EFFECT OF ULTRASONIC SHOT PEENING ON MECHANICAL PROPERTIES AND CORROSION RESISTANCE OF MG ALLOY SHEET

by

Jianyue Zhang

A Dissertation

Submitted to the Faculty of Purdue University

In Partial Fulfillment of the Requirements for the Degree of

Doctor of Philosophy

School of Engineering Technology

West Lafayette, Indiana

May 2019

THE PURDUE UNIVERSITY GRADUATE SCHOOL
STATEMENT OF COMMITTEE APPROVAL

Dr. Xiaoming Wang, Chair

Department of Mechanical and Engineering Technology

Dr. Milan Rakita

Department of Mechanical and Engineering Technology

Prof. David Johnson

School of Material Engineering

Prof. Sarah Leach

Department of Mechanical and Engineering Technology

Approved by:

Dr. Kathryne A. Newton

Head of the Graduate Program

To my parents and my sister

ACKNOWLEDGMENTS

I would like to express my sincere gratitude to all who helped me in the accomplishment of this work.

Firstly, I want to thank Dr. Qingyou Han, for his continuous support and encouragement in the past three years. I appreciate his patient guidance both in research and in life.

Special thanks to my thesis committee: Prof. Xiaoming Wang, Prof. Milan Rakita, Prof. David Johnson and Prof. Sarah Leach for their insightful comments and guidance. Sincere thanks to Prof. Fusheng Pan, Prof. Aitao Tang and Prof. Bing Jiang from Chongqing University for their valuable support and insight throughout the doctoral study.

I also want to thanks Dr. Jia She, Dr. Peng Peng, Dr. Yuan Xing from Chongqing University, Dr. Xusheng Yang from Chongqing University of Technology for their help in the mechanical tests and microstructure characterization. I am also grateful to Dr. Yongxing Jian from Xian Jiaotong University for his help on wear tests, and Dr. Dean Meng for his help on numerical modeling. In addition, I would like to thank the research team members, the staff from School of Engineering Technology and all those who made the the study at Purdue University meaningful and enjoyable.

At last, I would like to thank my family: my father Guofang Zhang, my mother Xiuying Pan and my sister Jianyuan Zhang for supporting me spiritually throughout the doctoral study at Purdue University and my life in general.

TABLE OF CONTENTS

LIST OF TABLES

LIST OF FIGURES

ABSTRACT

Author: Zhang, Jianyue. Ph.D.
Institution: Purdue University
Degree Received: May 2019
Title: Effect of Ultrasonic Shot Peening on Mechanical Properties and Corrosion Resistance of Mg Alloy Sheet
Major Professor: Xiaoming Wang

Magnesium alloys are regarded as the most promising structure materials in transportation and aerospace fields because of their low densities and high specific strengths. However, the unsatisfactory mechanical performance and corrosion resistance restrict their applications. Grain refinement is an effective way to improve the mechanical properties and widen the applications. Among which, ultrasonic shot peening shows a great potential in producing refined grains or even nanocrystalline. A nanocrystalline forms at the surface after ultrasonic shot peening treatment. The formed nanocrystalline has been proved to dramatically affect the mechanical properties, such as hardness, mechanical stress, wear resistance and fatigue life.

In this dissertation, the microstructure evolution of AZ31 Mg alloy after the ultrasonic shot peening as well as its effect on the mechanical properties are investigated. The grain size, the twin structure, the surface roughness and the residual stress distribution after ultrasonic shot peening are characterized. A gradient nanostructure is achieved through ultrasonic shot peening and the thickness of this gradient nanostructure increases with prolonging the treated time. The grains at the top surface after 5 min treatment is refined to 45 nm and further refined to 42 nm for 10 min and 37nm for 15 min treatment from the XRD result. A lamellar nanocrystalline is below the top surface and a lot of tensile twins are found at the heavily deformed grains below the nanocrystalline layer. Below the twinned layer, a residual stress is distributed as deep as 400 μm in the matrix. A rough surface is obtained and the surface roughness of the 5 min treated sample was 5.934 μm, increased to 6.161 μm for10 min and 6.236 μm for 15 min. The nanocrystalline

leads to the improvement of the microhardness, from 65 HV of the as-received to 123 HV, 127 HV and 145 HV for 5 min, 10 min and 15 min treatment, respectively. The tensile stress and compression stress are also improved remarkably. The yield stress is increased from 127.7 MPa of as-received to 198 MPa of 10 min treated sample and the compression stress is improved from 73 MPa to 100 MPa. The improved yield stress is attributed to the grain refinement and the work hardening of the nanocrystalline.

The wear resistance of AZ31 Mg alloy is improved greatly after ultrasonic shot peening process. The coefficient of friction and the wear rate of the ultrasonic shot peening treated sample are both lower than that of as-received. The width of the wear track of ultrasonic shot peening treated is also narrower than that of as-received, and the worn surface has a lower surface roughness. In as-received samples, abrasion and oxidation dominate the wear mechanism at low sliding speed and low applied load. The increase of sliding speed or applied load resulted in the delamination. Severe wear such as thermal softening happens with the further increase of load value or sliding speed. In ultrasonic shot peening treated samples, oxidation, the abrasion and delamination are also existing while no severe wear is found. The improved wear resistance of the ultrasonic shot peened sample is due to the improved hardness and a higher activity of oxidation during wear process. The nanocrystalline on the top surface leads to the transition boundary between the mild wear and severe wear to a higher sliding speed and higher applied load.

The corrosion resistance of AZ31 Mg alloy before and after ultrasonic shot peening is tested in 3.5 % NaCl solution. The corrosion resistance after ultrasonic shot peening is reduced greatly because of the Fe particles at the top surface, which was exfoliated from the shot during the treating process. After a 40 μm thick polishing, Fe particles are removed totally and the corrosion resistance is improved, compared with that of as-received. The anodic current density of the nanocrystallized surface after polishing is reduced because of the compression residual stress and a rapid formation of protective layer. Meanwhile, the grain boundary acts as a physical barrier for corrosion and reduces the corrosion rate.

The bending behavior of AZ31 Mg alloy before and after ultrasonic shot peening is studied by a V-bending test. The ultrasonic shot peening treated sample has a similar bending performance even though the ductility has been reduced after ultrasonic shot peening. A single side ultrasonic shot peening (either at the inner side or the outer side) changed the bending behavior because of its asymmetric structure. The ultrasonic shot peening at the inner side for 5 min improves the bendability and longer treated, such as 10 min and 15 min degenerates the bendability to as-received. The improved bendability of 5 min treated sample is due to the drawing back of the neutral layer. The ultrasonic shot peening at the outer side for 5 min also improves the bending performance and a longer treatment of 15 min further enhanced the bendability. The improved bendability after outer side treatment is due to the high yield stress of nanocrystalline at the convex, resulting in the smaller strain here.

CHAPTER 1. INTRODUCTION

1.1 Background

The development of light materials is of great concern in recent decades. The application of light materials on transportation can reduce the energy consumption and decrease the emission of CO^2 (Hakamada et al., 2007). For both economic and environmental reasons, these light materials are greatly needed in the future (Hirsch, 2011). Until now, light materials such as aluminum(Hirsch, 2011), titanium (Ivasishin, Anokhin, Demidik, & Savvakin, 2000), magnesium and composites materials have been applied in automobile and aerospace fields (Lesuer & Kipouros, 1995). Magnesium (Mg) alloy is regarded as one of the most promising alloys in automotive and aerospace fields. The density of Mg alloy is from 1.75 to 1.85 mg/m^3, which is 2/3 aluminum (2.7 mg/m^3) and 1/5 steel (7.8 mg/m^3) (Pollock, 2010). Magnesium is the eighth most common element on the earth. It can be produced by the metallothermic reduction of magnesium oxide with silicon or extracted from the sea or salt lakes (Kramer, 2000). Meanwhile, its high specific strength, high specific stiffness, and easiness to recycle makes Mg alloy one of the next generation structure materials in transportation (Mordike & Ebert, 2001). It is estimated the 22.5 Kg of mass reduction can lead to one percent improvement of fuel efficiency. A typical car weighing 1525 Kg currently contains about 5-6 kg of magnesium alloys, and the automotive manufacturers are looking to increase the Mg content to about 45-160 kg per automobile (Pollock, 2010).

The dominant manufacturing process of magnesium components is casting, such as high pressure die casting, low pressure casting, squeeze casting, semi-solid casting and loam foam casting (Vinarcik, 2002). The die-casting Mg alloys like Mg-Al-Sr and Mg-Al-RE have been established for the fabrication of engine block, cylinder block, chassis, real seal carrier and cradle (A. A. Luo, 2013). However, the further application of Mg alloys is limited because of its low mechanical properties, such as mechanical strength, wear resistance (Mondal et al., 2003), and poor corrosion resistance (Atrens,

Song, Cao, Shi, & Bowen, 2013). Mg is a hexagonal-close-packed (hcp) metal and there are very limited slip systems in the hcp structure. The limited slip system in Mg alloys results in poor ductility and poor deformational ability (Yamashita, Horita, & Langdon, 2001). Compared with aluminum alloys and steel, there are limited numbers of cast magnesium alloys available for structural application with low-cost and acceptable mechanical properties. The Mg-Al based alloys is the most conventional used Mg alloy because of its low-cost and moderate mechanical properties. The content of aluminium is usually from 3-9 wt% and additional elements less than 1 wt%. The limited age-hardening response of Mg-Al system restricts applying heat treatment to improve the mechanical strength. Recently, Alloy systems with substantial precipitation hardening, such as Mg-Sn (H. Liu, Chen, Tang, Wei, & Niu, 2007), Mg-Zn (A. Luo & Pekguleryuz, 1994) and Mg-RE (Hort et al., 2010) have been developed to improve the mechanical strength, but the cost of these systems is relatively high.

Efforts have been made to widen its further application as a structural material. The wrought Mg alloys are generally preferred due to its better mechanical performance, both the mechanical strength and ductility. Methods include extrusion (Y. Chen, Wang, Peng, Zhai, & Ding, 2007), rolling (Pérez-Prado, Del Valle, Contreras, & Ruano, 2004) and forging (Matsubara, Miyahara, Horita, & Langdon, 2003) have been developed to obtain wrought Mg alloy. The grain size can be substantially refined and the casting defects, such as porosity, can be eliminated through processing. The second phase can be refined as well. The wrought Mg alloys are currently used to a limited extent due to its low production speed and high manufacturing process cost (Easton et al., 2008). Due to its HCP structure, extruded Mg alloy presents a strong basal texture, with which the further formation is difficult at room temperature. An elevated temperature is required to activate the non-basal slip system to allow a desired formability, which causes a higher energy consumption and cost. Researchers have developed methods to weaken the texture after extrusion. The addition of rare earth (RE) elements is the most commonly applied method. The Gd or La containing alloys has a rare earth texture $(11\bar{2}0)$ that is parallel to

the extrusion direction, which improves the ductility (Stanford & Barnett, 2008). Besides the addition of RE elements, some new methods, like asymmetric extrusion(Q. Yang, Jiang, Tian, Liu, & Pan, 2013), and asymmetric composite extrusion(Q. Wang et al., 2016) are developed to title the c-axis after extrusion.

The grain size in Mg alloy can be further refined by several plastic deformation(SPD) methods, such as accumulative roll bonding (ARB), equal channel angular pressing (ECAP), high-pressure torsion (HPT), twist extrusion (TE), and low-temperature extrusion(Valiev et al., 2016). By these SPD methods, the grain size can be refined to hundreds of nanometers. Among these grain refinements, ultrasonic shot peening (USSP) is currently of great interest. During ultrasonic shot peening, a large number of flying balls are vibrated at the surface of the material. By this several plastic deformation method, ultrasonic shot peening can produce nano-crystallized grains at the surface of the materials(Tao, Sui, Lu, & Lua, 1999). With this nanostructure, the mechanical properties, such as yield strength, wear and fatigue, can be improved greatly (Rakita et al., 2013). The application of ultrasonic shot peening to Mg alloys is a recent concern of a lot of researchers. H. Sun et al. (2007) studied the grain refining deformation and found the depth of deformation layer is dominated by the dislocation, stacking fault and twining behavior in Mg alloys. Xia, Liu, Fu, Jin, and Lu (2016) found that the wear resistance of Mg-3Al-1Zn can be promoted after ultrasonic shot peening, and found the gradient nano structure can improve the wear resistance by alteration of the wear mechanism. Laleh and Kargar (2011) reported that the corrosion resistance of Mg-9Al-1Zn can be improved and the enhanced corrosion resistance is due to the dissolution of the second phase, which leads to the reducing of galvanic corrosion between the Mg matrix and the second phase.

To sum up, the formation of nanocrystalline in Mg alloy by ultrasonic shot peening provides a possible way to modify or improve the mechanical properties as well as other properties such as wear behavior or corrosion resistance, which has a potential to widen the application of Mg alloys in industry. The investigation of nanocrystalline at the top surface is necessary but with a challenges.

1.2 Scope of Study

This study focuses on the microstructure evolution at the surface on Magnesium alloys sheet processed by USSP and the effect of this microstructure evolution on the mechanical properties and corrosion resistance. The mechanical properties include the mechanical strength, the wear resistance and the bendability. Three USSP treatment times: 5 min, 10min and 15min are applied to obtain different thickness of nanocrystalline. The effect of USSP treatment time on the mechanical stress and microhardness is studied. The effect of nanocrystalline on the corrosion resistance of Mg sheet in 3.5% NaCl solution is studied. The dry wear behavior of Mg sheet before and after USSP is investigated. The bending process is held at a three-point bending experiment and the effect of thickness and the position of nanocrystalline on the bendability is investigated. The frequently used Mg sheet, AZ31 Mg alloy, is chosen as the investigated subject and the thickness of AZ31 sheet is 3 mm. An optical microscope, scanning electron microscope, electron back-scattered diffraction and transmission electron microscope is used to characterize the gradient nano structure.

1.3 Significance of Study

The further application of Mg alloys is limited to a specific area because of its relatively low mechanical stress compared with steel and aluminium alloys. Grain refinement is an effective way to improve the mechanical stress of alloys. The finer the grains are, the higher mechanical stress the alloy has. So, grain refining to obtain finer grains even nanocrystalline in Mg alloy is the key factor that affects its wider application. A lot of methods have been developed to obtain fine grain size. The grain can be refined by severe plastic deformation(SPD). It is reported SPD method like ECAP, HPT and ARB can refine the grain to less than 1 μm. Moreover, the USSP process is a more effective way and it is reported that the grain size can be refined to less than 100 nm. The mechanical stress can be improved by SPD while the ductility will be sacrificed most of the time. For Mg alloys, its ductility is limited due to its HCP structure and limited slip

system at room temperature. So it is necessary to investigate the effect of this nanocrystalline on the mechanical properties of Mg alloys. On the other hand, further application of Mg alloy is limited by the poor formability, low wear resistance and poor corrosion resistance. It is of interest and meaningful to investigate how the nanocrystalline affects the formability, tribological behavior and corrosion resistance of Mg alloy.

1.4 Research Questions

The main research questions of this study are:

1. What is the microstructure evolution during the ultrasonic shot peening process?
2. How does the nanocrystalline of Mg alloy processed by ultrasonic shot peening affect the mechanical properties?
3. How does the nanocrystalline of Mg alloy affect the corrosion properties?

1.5 Assumptions

The assumptions are shown as following:

1. The control of ultrasonic shot peening: The sample will be shot peened to obtain the nanocrystalline. The treatment will be 5min, 10 min and 15min. The distance between the sample and the ultrasonic generator will be 10 mm. The diameter of the steel ball will be 3 mm. It is considered that the parameter used will generate nanostructure on the sample's surface and the thickness of nanostructure layer will be stable for the same sample at the same parameters.
2. The control of sample: The sample will be picked from the as-rolled Mg alloy AZ 31 sheet with a thickness of 3mm. It is assumed the microstructure of the AZ31 sheet, including the grain size, the distribution of second phase, is homogeneous.

3. The immersion time for the corrosion resistance test is 7 days. It is assumed the immersion time is long enough to observe the corrosion behavior of AZ31 Mg alloy sheet.

4. The quality and quantity of the experimental data are sufficient to obtain the morphology and microstructure evolution during ultrasonic shot peening process.

1.6 Limitations

The limitations are as follows:

1. The accuracy of the grain size and the microstructure evolution after USSP treatment is dependent on the accuracy level of characterization equipment level.

2. The observation of nanocrystalline can only be achieved in TEM at a high magnification. The observation area is limited.

3. The observation of microstructure evolution by EBSD is achieved at a low magnification. The detailed microstructure evolution cannot be obtained.

4. The effect of the surface roughness provided by the USSP process on the corrosion resistance is not considered.

5. The load-stroke curve of the bending process in the in-situ EBSD experiment can not be recorded due to the limitation of in-situ equipment.

6. The accuracy of the FEM simulation results of the shot peening process and bending process is limited by the relationship between the mechanical properties and the microstructure evolution. The texture, the fluctuation of the thickness of gradient nano structure and the surface roughness will not be considered.

1.7 Delimitations

The delimitations are as follows:

1. The research will not focus on the second phase of Mg alloy on mechanical properties and corrosion resistance. The second phase is an important factor that effects the mechanical properties and corrosion resistance. The second phase in the matrix is a useful source to hinder the movement of dislocation and to improve its mechanical stress. On the other hand, during the SPD or heat treatment process, the second phase will be dissolved. This will result in a complex process. In this study, AZ31 Mg sheet is chosen because of its few amounts of second phases.
2. The research will focus on the effect of USSP treatment time on the mechanical properties and corrosion resistance of the AZ31 sheet. Other parameters include the size of shot, the distance between sheet and shot and the intensity of amplitude will not be discussed.

1.8 Summary

The chapter draws up a basic structure of the research project including the background and the main motivation of the research. It also lists the assumptions, limitations and delimitations of the research. The next chapter will present a summary of the concerned literature covering the application of USSP technology and the development of formation mechanism of nanocrystalline as well as the effect of nanocrystalline on the mechanical properties and corrosion resistance.

CHAPTER 2. REVIEW OF LITERATURE

This chapter provides a review of the literature relevant to the ultrasonic shot peening process, the mechanical properties and corrosion resistance of Mg alloy.

2.1 Overview of SPD and grain refinement

Efforts have made to improve the mechanical properties of alloys to widen their applications. Among these methods, grain refinement is the most traditional. The relationship between conventional grain size of alloy and its mechanical strength is described as the Hall-Petch equation, as shown in equation2. 1.

$$\sigma_Y = \sigma_{Y0} + Kd^{-1/2} \tag{2.1}$$

Where σ_Y is the yield stress, σ_{Y0} is the lattice resistance to the motion of dislocation, and d is the average grain size. In this equation, parameters σ_{Y0} and k are material dependent. So the pursuit of finer grain has generally been researchers' focus to improve the mechanical properties of alloys. For the as-cast alloy, the addition of grain refiner/ small number of solute elements to promote heterogeneous nucleation and restrict the grain growth. The grain in the as-cast alloy can be refined to less than 50 micrometers by this method, and can improve the mechanical properties (X. Wang, Liu, Dai, & Han, 2015). The as-cast grains can be further refined during the deformation process by extrusion, rolling and forging. In the wrought alloy, the grains are refined because of dynamic recrystallization during the deformation, and the grain size can be refined to several micrometes so the wrought alloy always has improved mechanical performance. In the past 30 years, new deformation methods called severe plastic deformation (SPD) are developed to fabricate the grains with a size of submicrometer or nanometer. The fabricated material with submicrometer (average grain size between 100 - 1000 nm) is called ultrafine-grained (UFG) materials and nanocrystalline with nanometer microstructure (average grain size $\leq$ 100 nm). Numerous techniques for the SPD process

have been developed in the past 30 years. The major methods established for the manufacture of bulk ultrafine material or nanocrystalline are high-pressure torsion (HPT), twist extrusion (TE), equal-channel angular pressure (ECAP), accumulative roll-bonding (ARB) and multi-direction forging (MDF)(Valiev et al., 2016). During the SPD process, heavy plastic straining is employed to the surface of bulk materials to achieve a fairly homogeneous and equiaxed microstructure with a grain size in the range of submicrometer or nanometer. Meanwhile, an amount of nanostructure, such as twins or nano particles, are also revealed in the SPD process. The method is called a top-down approach in the reported literature because it takes a bulk solid with relatively coarse grains to produce a submicrometer or nanometer microstructure. The effect of SPD processing is not only to the extreme fine grains, but also resulting in unusual phase transformation with the dissolution of second phases, precipitation and amorphization (Valiev et al., 2006). These changes in the materials may affect the deformation mechanisms and the properties can be changed in a radical way.

2.2 Principle of ultrasonic shot peening

Among these grain refining methods, ultrasonic shot peening is currently of great concern world-wide. The first known work dealing with the nanocrystalline by USSP is by Tao et al. (1999). The equipment of USSP is simple, as shown in Figure 2.1. It consists of the generator of ultrasonic signals, a transducer which translates the generated signals into mechanical motion, and a simple metal rod which propels the shots. During ultrasonic shot peening, a large number of flying balls impacted at the surface of the material (Rakita et al., 2013). The repeated impacting of the flying balls provide a high strain rate during the ultrasonic shot peening process. By this several plastic deformation method, ultrasonic shot peening can produce nano-crystallized grains on the surface of the materials.

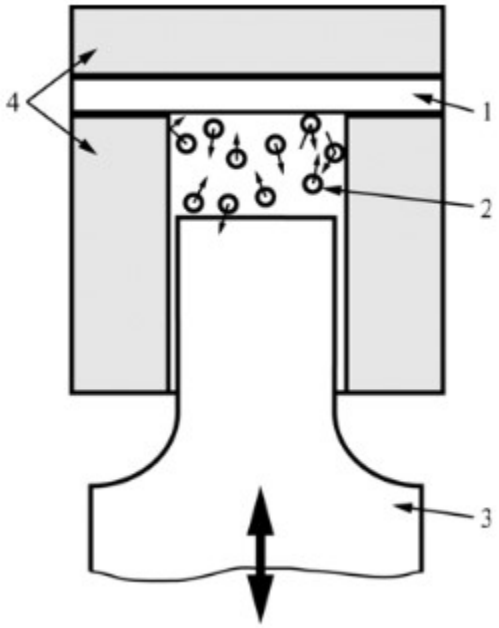

Figure 2.1. Schematic of USSP with (1) Workpiece, (2) Shots, (3) Horn and (4) Enclosure. Source: Rakita et al. (2013)

2.3 Fabrication of nanocrystalline by ultrasonic shot peening

This ultrasonic shot peening is regarded as the one of the most effective ways to produce the nanocrystallization (NC). Methods like HPT, ECAP and ARB, can refine the grains to UFG, but can be very difficult to acheive NC. However, the grains can be refined to about tens of nanometer by ultrasonic shot peening and the thickness of the NC layer generated varies with different materials. Tao et al. (1999) studied the formation of nanocrystalline at the top surface of Fe by ultrasonic shot peening process, and found that the grains at the top surface were refined to 10 nm with random crystallographic texture (Tao et al., 1999). During the treatment, the repeated peening generated a high density of dislocations and shear bands at the surface. Arrays of high-density dislocations happened at the shear bands and resulted in the formation of subgrain boundaries and separated individual grains. The similar surface nanocrystalline was achieved in 316L stainless steel by G. Liu, Lu, and Lu (2000). The result showed the shear bands formed by slip led to the formation of nanocrystalline while the shear bands formed by twinning could not led to

significant grain refinement. The surface nanocrystalline were also obtained in 304 stainless steel by H. Zhang, Hei, Liu, Lu, and Lu (2003). They found the formed nanocrystalline in 304 stainless steel was not only due to the arrays of high-density dislocation, but also the result of twin-twin interactions. The formation of twinning in 304 stainless steel was due to its low stacking fault energy(H. Zhang et al., 2003). The interactions of the twins resulted in the subdivision of the grains as well as a martensite phase transformation in nano scale. Wu et al. (2002) investigated the formation of ultrafine grains in 7075 Al alloy by USSP method. Lamellar type microbands with low angle misorientations were found at low stain and these microbands were subdivided by the formation of cell blocks inside. The subgrains were further refined to submicro or nanometer regime by the repetitive USSP process (Wu et al., 2002). K. Wang, Tao, Liu, Lu, and Lu (2006) studied the grain refinement mechanism in copper and found that the deformation twinning played a critical role. The original grains were divided into lamellae structure by the formation of high-density twins and the lamellae structure was further subdivided into equiaxed nanosized blocks with random orientation. Moreover, they found the minimum grain size was controlled by the stain rate during the USSP process (K. Wang et al., 2006). The surface nanocrystalline in the nickel alloy was also studied by Villegas, Dai, Shaw, and Liaw (2005). In this medium/low stacking fault energy material, the original grains were divided by a parallel array of microtwins and further subdivided by the twin intersections. Their results suggested two mechanisms in grain refinement from microtwins to nanograins. One is the generation of dislocation with a high density within microtwins and the other is the formation of deformation microtwins within the original microtwins(Villegas et al., 2005).

The application of ultrasonic shot peening to Mg alloys is a recent topic of concern by a lot of researchers. The dominating mechanism for the formation of fine grains in Mg alloys under USSP is considered to be a gradual transformation from dislocation cell walls to high-angel grain boundaries.H. Sun et al. (2007) studied the grain refining deformation and found the depth of the deformation layer is dominated by the dislocation, stacking fault and twining behavior in Mg alloys. The process and mechanism of nanocrystallization of Mg alloys during USSP is shown in Figure 2.2. At the beginning of

plastic deformation, twinning behavior governs, and the original grains are divided into finer twin platelets. Double twins and stacking faults appear within the twin platelets with the increase of strain. As the process continues, the dislocation slip systems activate. Because of dislocation movement along these planes and cross slips, high-density dislocation arrays are formed within twin platelets. These dislocation arrays subdivide the twins into subgrains with high strain energy. The high strain energy stored in the sample significantly decreases the recrystallization temperature. Simultaneously, the heavy plastic deformation at high strain rate would also raise the temperature of the sample. Once the temperature is higher than the recrystallization temperature, DRX takes place. They found the thickness of the NC layer could be as thick as 100 m on the solid solute AZ91D after 20 min USSP treatment(H. Sun et al., 2007).

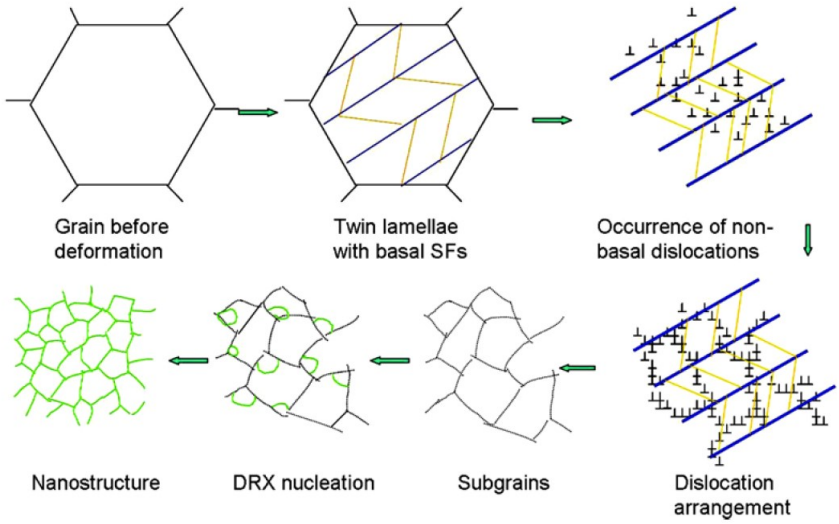

Figure 2.2. Schematic illustration of the grain refinement process of AZ91D during.

Source: H. Sun et al. (2007)

2.4 The modified material properties by ultrasonic shot peening

During the past 30 years, the intensive study on nanostructure materials shows that the nanocrystalline possesses fundamentally different properties, compared with the coarsen-grained counterpart, both mechanical properties and functional properties(Valiev et al., 2016). As one of the most effective ways to fabricate the nanocrystalline, the USSP process is expected to achieve a surface modification by nanocrystallization to change the surface properties of the material(Lu & Lu, 2004). The surface properties, such as fatigue, wear resistance, corrosion behavior, can be greatly modified after the surface nanocrystalline. Moreover, the overall properties, such as mechanical strength and ductility, are also changed after surface nanocrystalline. It is expected that this surface modification can widen the application of the materials by its unique properties.

2.4.1 Tensile properties and hardness

The grain refinement is the most popular mechanism of mechanical strengthening. According to the Hall-Pitch relationship, the finer the grains fabricated, the higher the yield stress obtained. After USSP treatment, the top surface layer is nanocrystallinezed and this surface layer has a much higher yield stress. Moreover, the improved yield strength at the surface can restrict happening of crack nucleation during a tensile test and leads to an improved yield strength of the overall material. Lu and Lu (2004) found the yield strength of 316L stainless steel can be improved from 280 MPa to 550 MPa after surface nanocrystalline during tensile test, after formation of 10 μm nanocrystalline at 316L stainless steel sheet with a thickness of 1 mm. They believed that the formed nanocrystalline at the surface would have 2-3 times increased yield stress. Y. Liu, Jin, and Lu (2015) investigated the mechanical stress improvement in pure Al and found the yield stress was enhanced from 43 MPa to 89 MPa after treatment.The improved mechanical strength was also found in Ni-based alloys. After 30 min treatment, the yield stress was increased from 437 MPa to 723 MPa, and further increased to 803 MPa after 180 min treatment(Tian et al., 2008). Wen, Liu, Gu, Guan, and Lu (2008) studied the mechanical

properties of pure Ti and Ti-6Al-4V alloy. The yield strength of pure Ti was increased by 100 MPa after treatment. For Ti-6Al-4V alloy, the yield strength was also increased but not so obviously by 20 MPa. X. Yang et al. (2015)investigated the mechanical behavior of pure copper after treatment. The yield strength of the coarsen grained copper was about 53 MPa and increased to 235 MPa when the volume fraction of the nanocrystalline reached 0.2 percent. In addition to the improvement of mechancial strength, Tian et al. (2008) found the improved mechanical stress was not only attributed to the formed nanocrystalline, but also affected by the compressive residual stress. J. Li, Chen, Wu, Soh, and Lu (2010) used a numerical simulation to study the individual effect of residual stress and work hardening of this surface nanocrystallized graded material during tensile test. The result showed the residual stress affected the initial stage and improved the yield stress, while it did not show much influence on the ultimate tensile strength. A more detailed experimental investigation was conducted by Moon et al. (2019). They found that the improved yield stress in copper was the combination result of residual stress and surface nanocrystalline. The contribution of residual stress was 20%.

Besides the improved yield stress, the elongation of the surface nanocrystallized material always presents a reduced ductility. The decreased ductility was due to the limited ductility of nanocrystalline and the presence of work-hardened surface region(Wen et al., 2008). Moreover, an extra strain hardening happened at the interface of coarsen grains and the nanocrystalline.X. Yang et al. (2015) illustrated a 3-D schematic of the graded material under uniaxial tensile test, shown in figure 2.3. During the tensile test, the coarsen grain matrix deformed plastically first, while the nanocrystalline still deformed elastically at the inelastic-plastic transition stage, forming a plastic-elastic interface. In the coarse grains adjacent to the interface, the gliding of dislocations was blocked at the interface and accumulated later, which resulted in an extra stain hardening.

The improved mechanical strength and the reduced ductility are also observed in Mg alloy after surface nanocrystalline. Shi et al. (2015) used USSP method to treat the extruded Mg-Gd alloys plate. They found the yield strength of the treated Mg-3Gd alloys ($\sim$ 150 MPa) was much higher than the initial one ($\sim$70MPa). The ultimate tensile strengths of the treated samples were about 50MPa higher than the initial sample. The

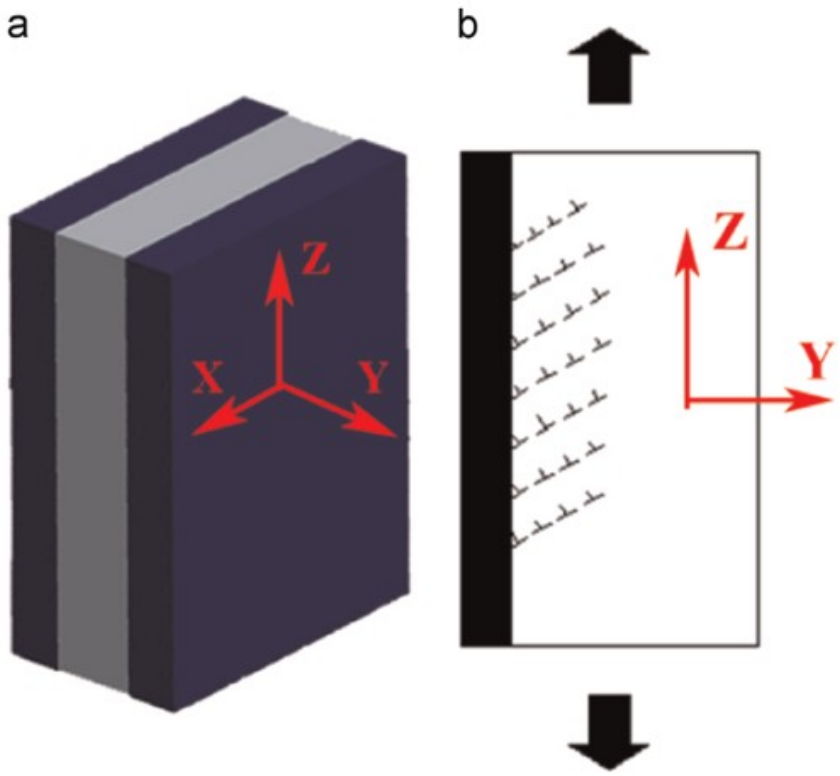

Figure 2.3. (a) A 3D schematic of the samples under uniaxial tensile stress.(b) Schematic illustration of dislocation pileup at the plastic/elastic interface.. Source: (X. Yang et al., 2015)

enhanced mechanical strength could be attributed to the grain refinement in the surface layer, the high density of twins in the center region and the strain hardening. Meng et al. (2017) found the yield strength of AZ31 Mg alloy sheet could be enhanced while a reduction of ductility could not be avoided. The deformation mechanism of AZ31 sheet with gradient structure was also studied by in-situ SEM and the results suggested the deformation localization as well as strain concentration could be suppressed and alleviated in the finer grains of the gradient AZ31 Mg alloy. H. Chen et al. (2017) studied the effect of surface nanocrystalline on the mechanical properties of AZ31 Mg alloy with a thickness of 1 mm, 2 mm and 3 mm after a treatment of 5 min, 15 min and 30 min. The longer treated time led to a higher yield strength. For sheets with different thickness, the 2 mm thick sheet presented the highest mechanical strength other than 1 mm thick sheet.

The yield strength of 2 mm thick AZ31 sheet after 30 min treatment was improved from 147 MPa to 249 MPa. This kind of exceptional results were also observed in the 304L stainless steel reported by Chan, Ruan, Chen, and Lu (2010). They attributed this abnormal decrease of yield stress to the high density of nano twins at the subsurface. A new simulation result, proposed by Wu, Jiang, Chen, Yuan, and Zhu (2014), showed an extraordinary strain hardening in the gradient structure. According to their simulation result, there is an optimized thickness of surface nanocrystalline that presented the best mechanical stress.

The formed nanocrystalline at the surface always presents a much higher hardness compared to the coarse grain. Lu and Lu (2004) used nanoindentation tests to determine the hardness of Fe after surface nanocrystalline, and found the hardness was as high as 3.8 GPa, which was almost twice of the coarse counterpart. The improved hardness was due to the grain refinement rather than the residual stress or the contamination from the USSP media. The improved hardness was also found in superalloy IN718(Kumar et al., 2014). There was about 20% enhancement of the hardness after treatment. However, an 8% reduction happened after the stress relieving, implying the improved hardness was the result of grain refinement and residual stress. Meanwhile, Moon et al. (2019)studied the improved hardness in copper and showed that the contribution of residual stress to hardening was estimated about 30%. In Mg alloys, the micro-hardness of the NC on the top surface of AZ91D was found twice as much as the matrix after surface nanocrystalline(H. Sun, Shi, & Zhang, 2008).

2.4.2 Wear resistance

The improved hardness and mechanical strength at the surface after surface nanocrystallization are expected to achieve a modified material behavior and the tribological performance is of great concern. The wear loss and macroscopic friction of the metallic material is always one of the challenges that determines the active time during contact conditions(Holmberg, Andersson, & Erdemir, 2012). The reduced friction as well as the wear losses will substantially prolong the lifetime of the material. According to

Archards law(Archard & Hirst, 1956), the worn volume of a material is related to its hardness, seen in equation 2.2:

$$W/L = KP/H \tag{2.2}$$

where W is the worn volume, L is the sliding distance, P is the applied load and H is the hardness of the softer one (always the tested material) in the two contacting parts. From the equation, it can be seen that the improved hardness by the nanocrystallization can enhance the wear resistance greatly. By the USSP treatment, the surface hardness can be enhanced to about twice that of the untreated one(Lu & Lu, 2004). As the wear resistance is surface sensitive, the improvement of wear resistance of this graded structure is more expected than the improvement of mechanical strength.

2.4.3 Modified wear behavior by nanocrystalline

During the past decades, a lot of work has been done to discover the relationship between the wear resistance and nano-grained metals. The reduced coefficient of friction and improved wear resistance have been reported in various nano-grained metals, fabricated by different methods. Lu and Lu (2004) reported that the surface nanocrystalline by USSP treatment in Fe showed a low coefficient of friction and wear loss. The coefficient values at different loads of the USSP treated sample were about half of these untreated sample. The enhanced wear performance was attributed to the higher surface hardness and the gradient microstructure and mechanical properties along the depth. Farhat, Ding, Northwood, and Alpas (1996) studied the effect of grain size (from 15 nm to 120 nm) on the wear behavior of nanocrystalline aluminum, fabricated by magnetron sputtering. They found the coefficient of friction decreased about 55% with the grain size decreasing from 10^6 to 16.5 nm. Meanwhile, a transitional behavior from severe wear to mild wear above a critical sliding distance was observed and the severe wear was sensitive to the grain size of the material.According to the result, a modified Archard-type equation incorporating the effect of grain size was proposed, as follows:

$$W = W_0 + K[\frac{P}{H_0 + kD^{-0.5}}] \tag{2.3}$$

where W is the worn volume, P is the loading force, H_0 is the hardness of the material and d is the grain size, K is a constant termed wear coefficient and k is coefficient between the grain size and hardness. Rupert and Schuh (2010)used electrodeposition technique to fabricate Ni-W alloy with grain sizes of 3-47 nm. The nanocrystalline Ni-W alloys presented increasing wear resistance as the grain size decreased. Meanwhile, the grains below 10 nm showed unexpectedly high wear resistance, which was due to the grain growth and grain boundary relaxation during the wear process. These changes were associated with an increase in hardness after wear. El Aal et al. (2010) studied the wear performance of Al-Cu alloys after equal channel angular pressing and found the wear resistance was improved by increasing the number of ECAP passes.The similar improvement of wear resistance was also observed in 7075 Al alloys(Chegini, Fallahi, & Shaeri, 2015). Edalati, Ashida, Horita, Matsui, and Kato (2014) applied high pressure torsion to obtain ultrafine-grained pure Al and Al-based composites and the wear resistance was also improved after HPT treatment.

Meanwhile, there are some reported results that imply the coefficient of friction was insensitive to the grain size. A. Wang, Venkataraman, Alspaugh, Katz, and Stoica (2012) studied the tribological behavior of pure Ti after HPT treatment. They found that the coefficient of friction of all the samples was 0.6, implying there was little grain size effect on the coefficient of friction. The improved wear resistance of the ultrafine-grained Ti was due to the transition of wear mode. The wear mode of the pure Ti was changed from ploughing and wedge formation for the coarse grains to abrasive for the ultrafine grains. Y. Zhang, Han, Wang, and Lu (2006) reported that the enhanced wear resistance of the surface nanocrystalline was affected by the value of the load force in copper. The friction coefficient of the nanocrystalline was lower than that of the coarse-grained when the load was below 20N. The difference between the nanocrystalline and the coarse-grained narrowed when increasing the load value. There would be a transition of wear damage modes when the load exceeded 40 N, and an abrupt increase of the wear

volume and the removal of nanocrystalline layer happened. Zhilyaev, Shakhova, Belyakov, Kaibyshev, and Langdon (2013) studied the effect of ECAP, HPT as well as their combination on the wear behavior of copper and found there was no advantage in reducing the wear rate in copper after the grain refinement. The coarse grain copper presented a better wear resistance and lower wear rate compared with all the UFG copper samples. The brittleness of the UFG copper led to the development of crack networks at the bottom of the wear track.

So the reduced coefficient of friction and wear rate can be achieved by nanocrystalline at certain conditions, which is at a low load force or low sliding speed, where the applied contact stress is far below the flow stress of the material(X. Chen, Han, & Lu, 2018).

2.4.4 Wear resistance of Mg alloy

For Mg alloy, the friction and wear behavior can not be forbidden if Mg alloys are used as structure parts, such as automotive brakes and engine components(An et al., 2008). Meanwhile, sliding wear is also an important factor in material processing by the rolling, extrusion and forging, etc.(H. Chen & Alpas, 2000). Thus, the wear behavior of Mg alloys is necessary to investigate while the detailed studies on the wear mechanisms are absent.

Among the investigations of the wear behavior of Mg alloys, AZ91 as well as its composites have been widely reported because of its priority and leading role in the structure application(Dey & Pandey, 2018). H. Chen and Alpas (2000) investigated the wear performance of AZ91 alloy using a block on ring configuration within a load range from 1 to 350 N and a sliding speed velocity from 0.1 to 2.0 m/s. Their results revealed that the sliding wear regimes could be classified into two main wear regimes: the mild wear regime and the severe wear regime. In the mild wear regime, an oxidational wear and a delamination wear was observed while in the severe wear regime, a severe plastic deformation induced wear and a melt wear was identified. The transition from the mild wear regime to the severe wear regime occurred when the surface temperature reached

75± 15 °C. A sliding wear map for AZ91 was established.Aung, Zhou, and Lim (2008) studied the wear behavior of AZ91D at low sliding speeds. They found abrasive wear was dominant at sliding speeds of less than 0.1 m $s^{-}1$, and oxidational wear happened because of the facilitated frictional heat at a sliding speed higher than 0.1 m $s^{-}1$. When the sliding speed was at 0.5 m $s^{-}1$ or higher, the delamination wear happened as a result of the load-bearing components and transmitted shear strains. The effect of normal loads on the wear behavior was investigated by An et al. (2008). Their finding revealed that the melting and plastic deformation were the dominant wear mechanism when the loads were higher than 200N(An et al., 2008). The wear behavior of AZ91D mg alloys was reported byS. Wang, Yang, Zhao, and Wei (2010). Their results suggested oxidation always took place during the wear process and a mechanical mixing layer (MML) which was made of a mixture of the oxides formed on the worn surface, resulting in an effective decrease of the wear volume. Shanthi, Lim, and Lu (2007) studied the effect of grain size on the wear resistance in AZ91 Mg alloy from 0.6-28.9μm, fabricated by mechanical milling. The fine-grained structure did not present an improvement in the wear resistance during the dry sliding process. The brittleness of the mechanical milled samples led to a micro-cutting abrasion and a higher wear rate while the formation of MML as well as its level of protection appeared to be unrelated to the grain size. The wear resistance of AZ91 Mg alloys with addition of RE elements could be improved due to the formation of stable oxide films on the worn surfaceQi, Liu, and Yang (2003). An et al. (2008) compared the wear behavior of AZ91 and $Mg_7Zn_1Y_2$, and pointed out the wear performance of Mg alloys was controlled by the changes in microstructure and mechanical properties when the surface temperature increased during sliding.

Based on the present reports and investigations in Mg alloys, there are two wear regimes: the mild wear regime and the severe wear regime and there are five main wear mechanisms: abrasion, oxidation, adhesion, delamination and plastic deformation.

2.4.5 Modified wear resistance of Mg alloy by nanocrystalline

The effect of the formed nanocrystalline on the wear performance in Mg alloy alloys was also reported. Xu et al. (2013) studied the wear resistance of AZ31 Mg alloy processed by equal channel angular pressing, and found the average values of the COF were decreased after ECAP process. Additionally, the wear depth and the volume loss were reduced with the increase of ECAP passes. The same effect was found in AM70 Mg alloy after ECAP process, and the smoother wear surface was due to the uniform hardness distribution (Gopi & Nayaka, 2017). The wear behavior of HPT processed UFG AZ31 Mg alloy was reported by Seenuvasaperumal et al. (2018). The wear rate of the sample was decreased after HPT treatment because of the increased hardness. Meanwhile, a distinct feature called lathy strip was observed in the untreated sample, which accelerated the wear rate. This lathy strip was diminished for the HPT treated sample with full recrystallization. The tribological behavior of the AZ91 after surface nanocrystalline fabricated by USSP with an average grain size of 30nm was investigated under dry sliding H. Sun et al. (2008). The nano-grained surface showed a lower friction coefficient and wear rate. The improved wear resistance was due to the grain refinement strength effect. The wear mechanism of the nanocrystalline was similar to the coarse-grained alloy, which was cutting, plowing and oxidation wear. The effect of surface nanocrystalline by laser shot peening on the wear resistance was also studied by Ge et al. (2018). The reduced wear rate after laser shot peening was because of the grain refinement and the strain-hardening generated by laser shot peening. The wear mechanism of the sample before and after laser shot peening was a mix of abrasive wear and oxidation wear. The tribological behavior of the AZ91 after surface nanocrystalline fabricated by USSP with an average grain size of 30nm was investigated under dry sliding. The nano-grained surface showed a lower friction coefficient and wear rate. The improved wear resistance was due to the grain refinement strength effect. The wear mechanism of the nanocrystalline was similar to the coarse-grained alloy, which was cutting, plowing and oxidation wear. The surface nanocrystalline by the ultrasonic nanocrystalline surface modification treatment was reported to enhance the wear resistance of AZ91D Mg alloy

by the surface hardness and the abrasive wear was the major wear mechanism (Amanov, Penkov, Pyun, & Kim, 2012). Meanwhile, a thicker oxidation layer was found at the untreated surface, indicating the nanocrystallized surface was able to prevent the oxide layer. A smaller oxide layer would reduce the risk of delamination mechanism because the oxide wear debris could become the source of micro-cracks by mixing into the deformed surface (So, 1995). The wear resistance of Mg-6Gd-3Y-0.5Zr alloy after surface nanocrystalline by USSP treatment was studied (Y. Liu, Jin, Li, Zeng, & Lu, 2015). They found the nanocrystalline exhibited a poor wear resistance because of the low ductility of the nanocrystalline and a high risk of fracture during the wear process. Meanwhile, at a higher sliding speed, the formed wear debris would fall in the valley and induced the occurrence of a delamination wear mechanism in nanocrystalline. A similar investigation in AZ31 Mg alloys showed the formed nanocrystalline substantially promoted the formation of an oxidation layer on the worn surface and reduced the wear rate by developing a compact oxidation layer (Xia et al., 2016).

To sum up, the formed nanocrystalline can improve the wear resistance because of its higher hardness while the improved hardness will also lead to the brittleness of the material and risk the formation of micro cracks. Meanwhile, the formed oxidation can protect the matrix by reducing contact while it will also have a possibility to fall into the valley and induce the occurrence of delamination.

2.5 Corrosion resistance

Corrosion is defined as the destructive attack of a metal under chemical or electrochemical reaction with its surrounding environment. Every year, the direct cost of corrosion is about 3-4% of the Gross National Product globally (Revie, 2008). From the prospect of economics and safety, there is a great motivation to conduct corrosion research. Like wear resistance, corrosion behavior of a material is also a surface sensitive property. The formed surface nanocrystalline by the USSP process is modified by the mechanical properties of the material. So the corrosion behavior of materials after USSP treatment is of great interest.

2.5.1 Modified corrosion behavior by surface nanocrystalline

Y. Li, Wang, and Liu (2004) studied the corrosion behavior of low carbon steel after USSP treatment in 0.05 M H_2SO_4 + 0.05M Na_2SO_4 aqueous solution, and found the corrosion rate increased after surface nanocrystalline. They suggested the grain refinement induced more grain boundaries and the atoms at grain boundaries had a higher energy to take part in the reaction, resulting in an increase of anodic current density. Mordyuk, Prokopenko, Vasylyev, and Iefimov (2007) investigated the effect of ultrasonic shot peening treated time (from 1-4 min) on the corrosion resistance of 321 stainless steel, and found an optimal corrosion behavior after 1 min treatment. A further increase of treated time would decrease the corrosion resistance because of the strain induced martensite and the galvanic corrosion between the austenite and martensite. X. Wang and Li (2002) studied the corrosion behavior of the surface nanocrystallized and annealed 304 stainless steel in 3.5 % NaCl solution. The corrosion resistance was reduced after surface nanocrystalline and a following annealing at 350 °C for 60 min showed an increased corrosion resistance. The improved corrosion resistance of the annealed sample was due to the formation of a dense passive film on the top surface. Lee, Kim, Jung, Pyoun, and Shin (2009) compared the corrosion resistance of the shot peening and ultrasonic shot peening samples of 304 stainless steel. The shot peened samples presented a lower corrosion resistance than the untreated whereas the ultrasonic shot peened sample showed a better corrosion resistance than the untreated sample. They attributed these differences to the surface roughness after peening treatment. Even though there were more strain-induced martensite on the ultrasonic shot peened sample, it showed a superior general and localized corrosion resistance. The same kind of improvement in corrosion resistance was also observed in Ti25Nb3Mo3Zr2Sn alloy after surface nanocrystallization (Huang & Han, 2013). The grain refinement led to a dilution of segregated alloying elements at the grain boundaries and relieved the intergranular corrosion. Moreover, the high densities of grain boundaries and dislocations provided more nucleation sites for passivation during the corrosion process, forming a thicker passive layer. The enhanced

corrosion resistance by the surface nanocrystalline was also observed in Ni-Ti alloy (Hu et al., 2011), β-type titanium alloy (Lei, Cui, Xiu, Gang, & Lian, 2014), Ti6Al4V titanium alloy (Jelliti et al., 2013), pure Zirconium (Han, Zhang, Lu, & Zhang, 2009) and pure aluminum (Ralston, Fabijanic, & Birbilis, 2011).

2.5.2 Corrosion behavior of Mg

The corrosion resistance of Mg alloys is one of the key Achilles heels of the metal that limited its application, not only in the transportation field but also as a biomaterial(Esmaily et al., 2017). The poor corrosion resistance of Mg and its alloys is mainly attributed to two key factors: (1) the highly electronegative potential of Mg and (2) the poor protection of the formed surface films upon Mg. The standard electrode potential of Mg at 25 °C is -2.37V, which allows the corrosion to process even in the absence of oxygen. In the air at room temperature, Mg reacts instantaneously with oxygen to form Mg oxide:

$$Mg(s) + \frac{1}{2}O_2(g) \rightarrow MgO(s)$$

The formed oxide layer upon the surface of bulk Mg is just a few nm in thickness. Meanwhile, the MgO/Mg Pilling-Bedworth ratio is just 0.81, which means the Mg surface layer is not fully covered and the protection of the MgO film is limited (Gusieva, Davies, Scully, & Birbilis, 2015). Moreover, the chemisorption of water on the MgO films takes place in the solutions, results in hydroxylation of the MgO surface:

$$MgO(s) + H_2O \rightarrow Mg(OH)_2$$

The hydroxylation of the MgO film is a bilayer structure and is illustrated in figure 2.4.

Both the formed $Mg(OH)_2$ and MgO are relatively soluble in water, which means the formed film can be easily dissolved and the protection is limited in neutral and acidic solutions.

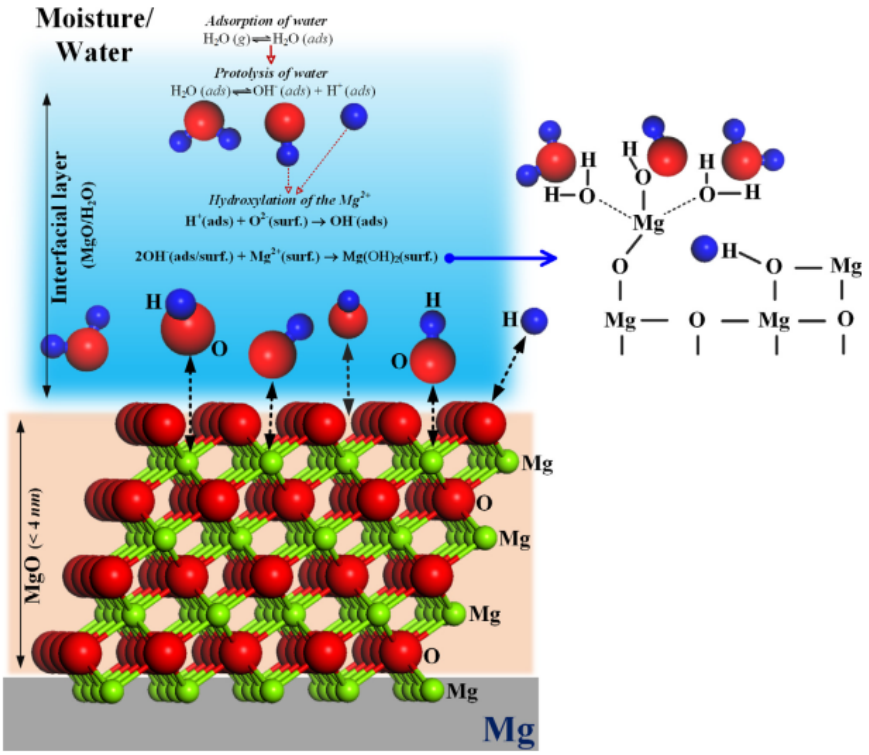

Figure 2.4. Schematic illustration of the hydroxylation of MgO surface. Source: (Esmaily et al., 2017)

On the other hand, alloying is necessary for Mg to achieve the required mechanical properties as a structural material because of the insufficient strength of pure Mg. The alloying elements can be divided into two groups: (1) insoluble with a solubility less than 0.05 wt.%, such as Fe, Nb, Zr and Si; (2) soluble, such as Al, Sn, RE and Zn (Gusieva et al., 2015). For the insoluble elements, the added alloys can just exist as impurities, which is usually more noble than Mg. For the soluble elements, there will be a second phase when the content exceeds its solubility, and the formed second phases are usually more noble, too. Unlike the case of Cr addition for Fe or the case of Mg addition for Al alloy, for the purpose of improving corrosion resistance, there are few elements that can be

added to form so-call stainless Mg. As the second phase or impurity is more noble, Mg serves as a sacrificial anode during the corrosion process (G. Song & Atrens, 2003). The effect of alloying in binary Mg-alloys in NaCl solution is summarized and presented in figure 2.5.

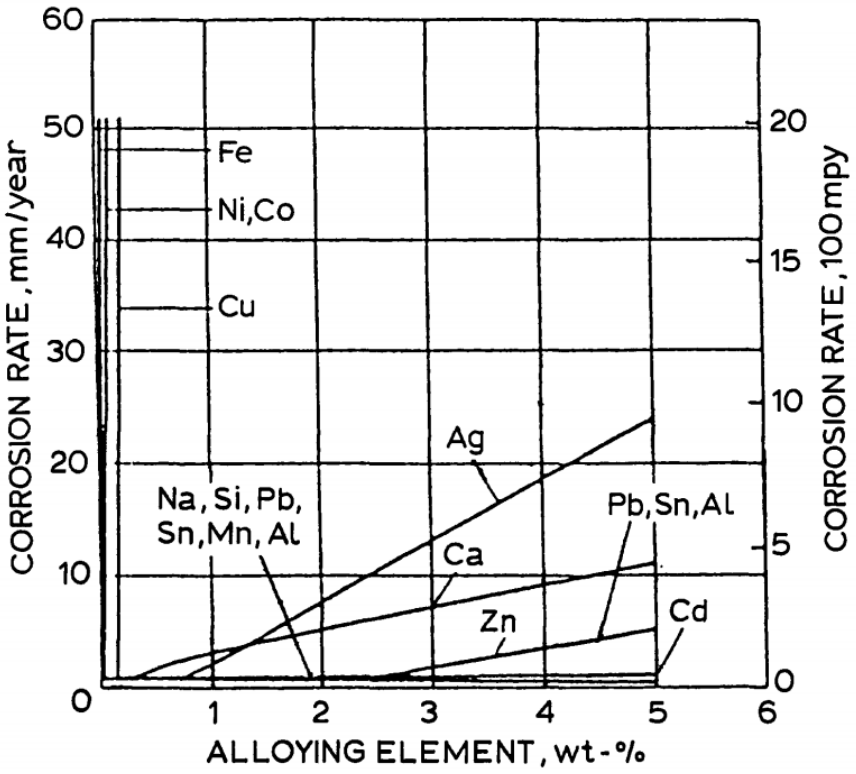

Figure 2.5. Effect of alloying additions on corrosion behaviour of binary magnesium alloys in 3% NaCl solution. Source: (Makar & Kruger, 1993)

It can be seen that the corrosion resistance of Mg is very sensitive to the content of impurities, such as Fe, Cu and Ni. There is a tolerance limit of each impurity: 170 ppm for Fe, 1000 ppm for Cu, and 5 ppm for Ni.

Besides the content of alloy element, the crystallographic orientation of Mg alloy also has a great effect on the corrosion resistance. G.-L. Song, Mishra, and Xu (2010) found the (0001) crystallographic plane was more electrochemically stable and corrosion resistant than the $(10\bar{1}0)$ and $(11\bar{2}0)$ prismatic planes. The difference between the corrosion resistance was attributed to their different electrochemical activities of (0001),

$(10\bar{1}0)$ and $(11\bar{2}0)$, which originated from the different surface energy levels. Hagihara, Okubo, Yamasaki, and Nakano (2016) investigated the corrosion behavior of pure Mg single crystals and found the anodic reaction governed the difference between different orientation planes. The corrosion rates increased in the order: $(0001) < (11\bar{2}0) < (10\bar{1}0) < (11\bar{2}3) < (10\bar{1}2)$.

Meanwhile, the corrosion resistance of Mg alloys can be modified by controlling the morphology of second phases. The formed second phase is always more noble than the matrix and accelerates the micro-galvanic between the matrix. Zhao, Liu, Song, and Atrens (2008) studied the effect of β-phase morphology on the corrosion behavior of AZ91 Mg alloys. The results indicated that the formed noble β-phase second phase could act as a barrier to hinder the corrosion propagation if the morphology of second phase is a continuous network. This kind of barrier behavior was also observed in Mg-Zn-Y alloy (J. Zhang, Xu, Cheng, Chen, & Kang, 2012) and Mg-2Zn-0.46Y-1.0Nd alloy (B. Wang, Guan, Wang, Wang, & Zhu, 2011).

2.5.3 Modified corrosion resistance of Mg alloy by nanocrystalline

For the nanocrystalline in Mg alloys, it is looking forward to obtaining an improved corrosion resistance. Aung and Zhou (2010) reported that the grain boundaries can act as a physical barrier to stop the extension of corrosion between grains. The smaller grain size produced more grain boundaries and the corrosion rate was slowed down due to the better barrier effect. The corrosion resistance of nanocrystalline fabricated by SPD methods are reported. Ahmadkhaniha et al. (2018) applied HPT to cast pure Mg and found the corrosion resistance was not significantly affected by the HPT treatment. A different result was reported by Gao et al. (2011). They found a nano-sized second phase with a uniform distribution was obtained after HPT treatment in Mg-Zn-Ca alloys, resulting in a reduced corrosion rate in simulated body fluid. C. Zhang et al. (2016) also reported a similar result in Mg-Zn-Ca. They found the galvanic corrosion occurred near the grain boundary in untreated, while the initiation of corrosion covered the entire surface after HPT treatment. As a result, a uniform and compact film formed at the surface of

HPT treated samples, leading to better corrosion resistance. The same kind of improvement of corrosion resistance after nanocrystallization was also reported by Pu et al. (2011). They used cryogenic burnishing to fabricate a surface with a grain size of 200 nm. The improved corrosion resistance was due to the positive effect of grain refinement as well as a strong basal texture. Birbilis, Ralston, Virtanen, Fraser, and Davies (2010) studied the grain refinement in pure Mg after ECAP as well as the corrosion resistance and an improved corrosion resistance was also observed by decreasing the grain size. Laleh et al.(2011) reported that the corrosion resistance of Mg-9Al-1Zn could be improved after USSP treatment and the enhanced corrosion resistance was due to the dissolution of the second phase, which led to the reducing of galvanic corrosion between the Mg matrix and the second phase(Laleh & Kargar, 2011). They also found that the diameter of the flying balls would not change the grain size on the top surface, but the thickness of the deformation layer increased with the increase in ball size. The increased ball size also resulted in the added surface roughness and defect density, which will decrease the corrosion resistance of Mg alloy. N. Li et al. (2014) applied the surface nanocrystalline in pure Mg and Mg-Ca, and their results showed the corrosion rates were increased after the treatment. The increased corrosion rate was attributed to the high density of crystalline defects.

2.6 Summary

This chapter provided a summary of the relevant literature for the mechanical, tribological and corrosion properties of Mg alloy and application of USSP on Mg alloys. Fabrication of nanocrystalline on the surface of bulk Mg alloy by USSP method is developed recently and regarded as one of the most promising methods to produce nanocrystalline by a top- down method. It was demonstrated that the application of Mg alloy had been limited to a specific area due to the low stress, limited tribological resistance and low poor corrosion resistance. It also pointed out that the grain refinement would effectively improve the mechanical stress, wear resistance and corrosion resistance.

So the effect of surface nanocrystalline should be done in the area to figure out the mechanism of nanocrystalline on the mechanical properties, wear resistance and corrosion properties and provide theory support to widen the application of Mg alloys with nanocrystalline in the future.

CHAPTER 3. FRAMEWORK AND METHODOLOGY

This chapter presents the framework and methodology used in this study to demonstrate the ultrasonic shot peening process, materials characterization, corrosion behavior, wear behavior and bending behavior of Mg alloys. This chapter outlines the methods that will be used in this quantitative study, which includes the research design, experimental setup and parameters, characterization method.

3.1 Research Approach

A 3mm thickness Mg AZ31 alloy sheet samples will be prepared and ultrasonic shot peening treated to obtain a surface nanocrystalline structure. X-ray Diffraction (XRD), Optical Microscopy (OM), Scanning Electron Microscopy (SEM), Electron Back Scatter Diffraction (EBSD) and Transmission Electron Microscopy (TEM) are some of the technologies used to characterize the microstructures of the nanocrystallized samples. Finite element simulation software ABAQUS will be used to simulate the single shot peening process and the bending process. The mechanical properties, wear resistance, corrosion resistance and bending performance of the materials with surface nanocrystalline will be tested.

3.2 Material Preparation and USSP treatment

AZ31 Magnesium alloy rolled sheets with a thickness of 3 mm were purchased online. In order to get a uniform microstructure, annealing heat treatment at 200 °C was conducted in an electric resistance furnace to get uniform microstructure. At the material preparation stage, a lathe was used for cutting the 3 mm thick Mg plate into smaller plates of 6 cm in length and 5 cm in width plate. Then a grinding machine was responsible for grinding and polishing the specimens. The specimens were polished to 2000 grit by SiC polished paper and ultrasonic cleaned in ethanol before USSP treatment. The ground and polished specimens were ultrasonic shot peening treated (USSP) at room temperature.

The vibration frequency was 20 KHz, and the distance between the sample and the horn is 10 mm. The shots used here were stainless steel balls with a diameter of 3 mm. The specimens were treated for 5 minutes, 10 minutes and 15 minutes to fabricate the nanocrystalline with different thickness on the surface of Mg alloys.

3.3 Hardness Test

The Vickers hardness measurements were performed on the cross section of the ultrasonic shot peened surface and on the as-received surface using a Vickers micro hardness tester applying from the surface to center of sample with a load of 100 g and a holding time of 15s. Before hardness measurements, the cross-sectional sample was mounted and polished to 2000 grit in SiC abrasive paper. Five points were measured at every depth from the top surface.

3.4 Tensile and Compression Test

The ultrasonic shot peening treatment was conducted on both sides of the sheet to measure its effect on the mechanical properties. One side was first treated and then the other side. The treated time was 5 min, 10 min and 15 min. Uniaxial tensile tests at room temperature were conducted on CMT6305-300KN test machine with a gauge length of 14 mm and cross-sectional areas of 6 mm $\times$ 3 mm, shown in Figure 3.1. The compression test sample was 3mm$\times$ 3mm$\times$ 5mm (TD$\times$ ND$\times$ RD), and compressed along the RD direction. All the tensile and compression test samples were taken along the rolled direction by CNC wire-cut machine. The test speed was 0.5 mm/min. Three samples for each condition were repeatedly tested and the resulting data were averaged.

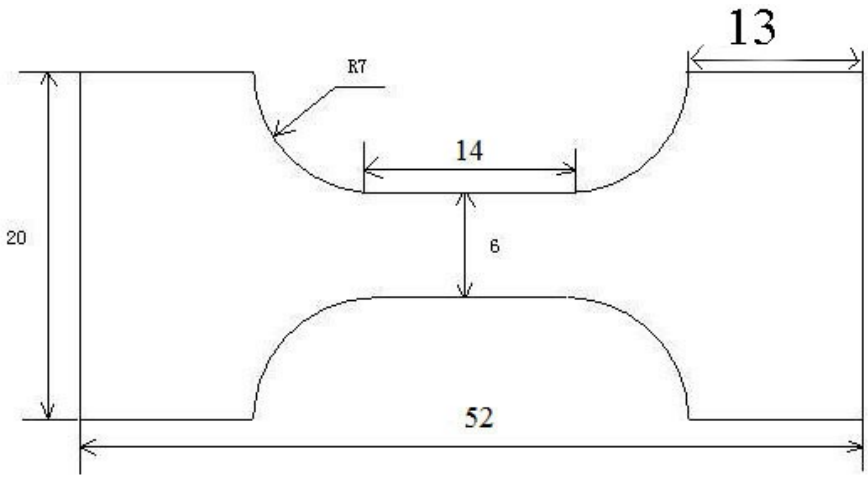

Figure 3.1. The schematic diagram of the tensile test sample

3.5 Corrosion Evaluations Test

The corrosion behavior of the as-received and USSP treated samples were conducted in 3.5 wt.% sodium chloride (NaCl) solution at 25 ^{o}C by electrochemistry test, weight loss test and hydrogen evolution experiment. The samples of corrosion evaluations were machined by a CNC wire-cut machine into specimens of 10 mm $\times$ 10 mm $\times$ 3 mm (TD$\times$ RD$\times$ ND). The specimens were mechanically ground to 2000 grit by SiC abrasive paper, cleaned with ethanal, and dried with warm flowing air. The specimens were mounted into epoxy resin except the TD$\times$ RD surface, of which the area was 1 cm^2. The TD$\times$RD surface was exposed in 3.5 wt.% sodium chloride solution to measure the corrosion resistance by the hydrogen evolution, weight loss test and potentiodynamic polarization curves. In order to test the corrosion evaluation of different depth from the top surface, the samples were polished to 20 μ m, 40 μm, 80 μm and 100 μm away from the top surface. The samples were polished by hand very carefully at 2000 grit SiC abrasive paper and the thickness before and after a few hand polishing was measured by micrometer until an expected thickness was obtained.

The electrochemistry test was conducted using a VersaSTAT 3 potentiostat/galvanostat connected to a three-electrode cell. The schematic illustration is shown in Figure.3.2.

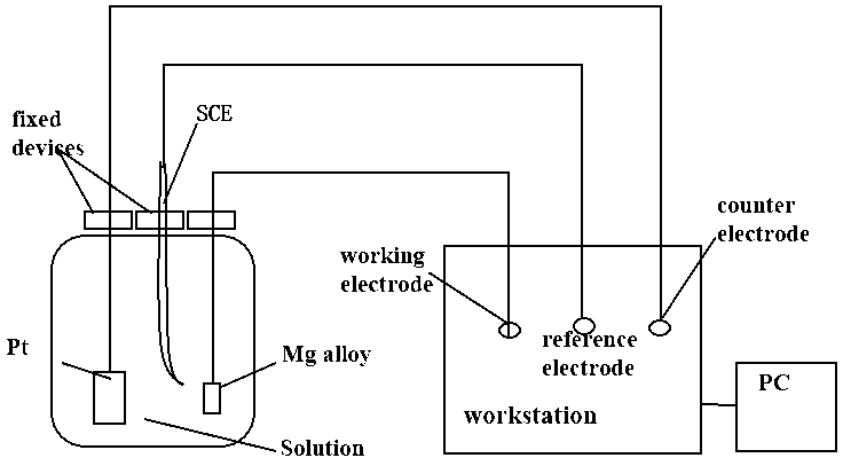

Figure 3.2. The schematic diagram of the three-electrode cell system

In the three-electrode cell system, the working electrode was the tested AZ31 Mg alloy sheet, and the contacted surface with the solution was 1 cm^2. The counter electrode was platinum, and the saturated calmel (SCE) electrode was the reference electrode. Open circuit potential vs. time curves were measured for the as-received sample, ultrasonic shot peening treated sample and polished sample. The electrochemical impedance spectroscopy (EIS) measurements were conducted after immersion for 15 min with the frequency ranging from 100 kHz to 0.02 Hz. The amplitude of the sinusoidal potential signal was set as 10 mV with respect to the open circuit potential. The polarization curves were obtained at a scan rate of 0.2 mV/s. Tafel fitting was employed to analyze the polarization curves to give the corrosion potential (E_{corr}) and the corrosion current density (i_{corr}). The values of the corrosion current density ($i_{corr}/mAcm^{-}2$) were converted into the corresponding corrosion rates (P_i/ mm y^{-1}) by the following equation (Atrens, Liu, & Abidin, 2011)(Cao et al., 2013):

$$P_i = 22.85 \times i_{corr} \tag{3.1}$$

The hydrogen evolution test was conducted in a burette above the specimens. The experiment setup is shown in figure.3.3 The specimen was mounted in an epoxy resin with the top surface explored to the solution, and the explored area is 1 cm^2. The hydrogen evolution volume (ΔV/mL cm^{-2}) was measured and converted to the hydrogen evolution volume rate (V_H/mLcm^{-1} d^{-1}). The hydrogen evolution volume rate was also converted to the corrosion rate (P_H/ mm y^{-1}) by the following equation(Atrens et al., 2011)(Cao et al., 2013):

$$P_H = 2.279 \times V_H \tag{3.2}$$

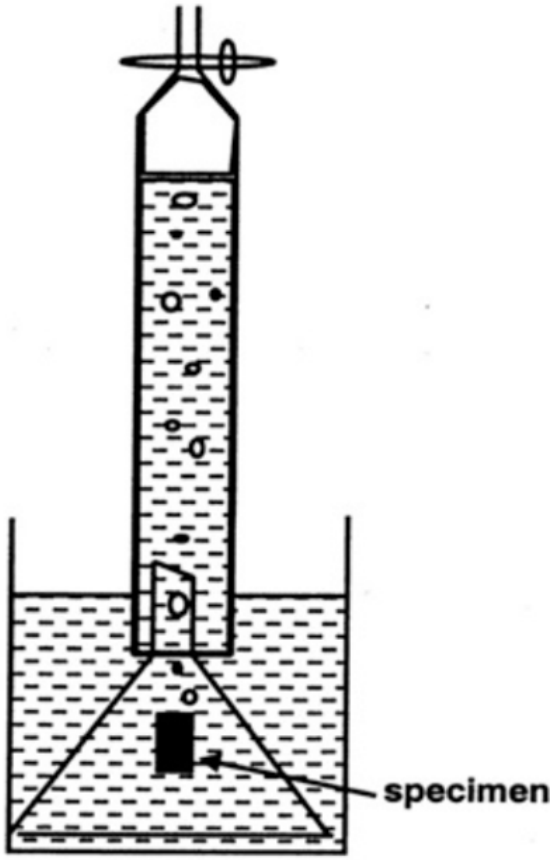

Figure 3.3. The schematic diagram of the hydrogen evolution test

The weight loss test was measured by the weight change after the immersion in 3.5 wt.% sodium chloride solution for 7 days. After the immersion, the formed corrosion products were removed by a cleaning solution of 150 g L^{-1} CrO_3 and 10 g L^{-1} $AgNO_3$ at an ultrasonic cleaning machine. The weight changes before and after the immersion (Δ W/mg cm^{-2}) were converted to the weight loss rate (V_W /mg cm^{-2} d^{-1}). The weight loss rate was evaluated using the following equation (Atrens et al., 2011)(Cao et al., 2013):

$$P_w = 2.1 \times V_w \tag{3.3}$$

3.6 Wear Resistance Test

The wear resistance of the as-received and ultrasonic shot peening treated samples were tested by dry sliding wear tests on a computerized ball-on-disk wear testing machine at room temperature and in the air with a relatively humidity of 45%. AZ31 Mg alloy sheet were cut to disks of 44 mm in diameter. The surface of the test samples was mechanically polished to a surface roughness of 0.05 μm and then cleaned by acetone solution in an ultrasonic clean machine. The GCr15 ball with a surface roughness of 0.1 μ m and hardness of 700 HV was selected as the friction pair. The ball was cleaned each time before use by an acetone solution in ultrasonic clean machine. The sliding speeds were 0.1m/s and 0.5 m/s, and the applied loads were 10N, 30N and 50N. The rotational speeds were 800 r/min for 0.5 m/s and 160 r/min for 0.1 m/s.

3.7 Bending Behavior Test

The rolled AZ31 Mg alloy sheets with the thickness of 3 mm were cut into the specimens with a length of 50 mm and a width of 12 mm, along the rolled direction. In order to investigate the effect of surface nanocrystalline the bendability, the USSP treated samples were cut from the center of USSP treated area along the rolled direction, with a length of 50 mm and a width of 12 mm. The one-side treated and two-side treated samples were both applied to the bending test. For the one-side treated sample, the nanocrystalline

will be placed at the compression side or tensile side, respectively. Three USSP treated durations: 5 min, 10 min and 15 min, were applied. The V bending test was conducted at room temperature on a CMT6305-300KN test machine with a V-punch radius of 4 mm and a die with consistent bending angle of 120^o. The V-bending is a kind of three-point bending. The specimen with a length of 50 mm and a width of 12 mm was placed at the die and the punch speed was set to 3 mm/min. To ensure the replicability, each sample condition was tested three times.

3.8 Material Characterization Methods

The microstructure evolution during the USSP process was investigated by optical microscope (OM), scanning electron microscope (SEM), Electron Back Scatter Diffraction (EBSD) and transmission electron microscope (TEM). The cross section of ultrasonic shot peening was mechanically polished by SiC abrasive paper to 2000 grit. For optical microscope and scanning electron microscope, the sample was etched with a solution of 50 ml ethanol, 5 ml water, 5 ml acetic and 5 g picric acid. The SEM characterization was conducted on JEOL 7800F field emission gun scanning electron microscope or Zeiss AURIGA FIB/SEM dual beam system. The characterization of the nano-grained structure was conducted by a FEI Tecnai G20 transmission electron microscope and operated at 20 kV. The TEM sample was prepared by the FIB Lift-out method using a Zeiss AURIGA FIB/SEM dual beam system. Bright-Field (BF) TEM images were captured to characterize the nanograined structure. The micro orientation and texture of samples were analyzed by electron-back scattering diffraction (EBSD) method. Sample preparation for EBSD analysis consisted of polished by SiC paper to 2000 grit and followed electro-polishing in an AC2 electrolyte, using a voltage of 20 V for 60 s at -20 °C. EBSD was conducted on a JEOL 7800F field emission gun scanning electron microscope with HKL Channel 5.0 software. The distribution of elements was characterized by Zeiss Auriga FIB-SEM dual beam system equipped with an X-ray energy dispersive spectrometer.

3.9 Surface Topography

The surface topography of the ultrasonic shot peening treated sample and the morphology of the worn surface were analyzed using a color 3D laser scanning microscope (VK-970, Keyence Corporation, Japan). The surface topography and surface roughness of the ultrasonic shot peening treated sample with treated time of 5 min, 10 min and 15 min were investigated with a scanning area of 2.5 mm $\times$ 2.5 mm. The three-dimensional morphology and the surface roughness of the worn surface were analyzed with a scanning area of 1.5mm $\times$ 1 mm.

3.10 X-ray diffraction

To identify the grain size and the grain orientation after ultrasonic shot peening, X-ray diffraction tests were performed on the Riguku D/max 2500PC X-ray diffractometer with Cu-K radiation. The tests were conducted by a scan step of 0.02^o per step in the 2θ ranging from 10^o to 90^o. The sample was cut from the USSP treated area with a size of 10 mm $\times$ 10 mm by CNC wire-cut machine. To avoid the possible changes of residual stress, the cutting edges of the sample were carefully polished by hand in SiC paper.

3.11 Finite Element Simulation

A finite element simulation model was applied to simulate a single shot peening process and the V-bending process using ABAQUS commercial software. In the single shot peening process, the steel shot was regarded as a rigid body, which meant the shot would not be deformed during the shot peening process. The Mg alloy sheet was modeled as a deformable body. The properties of Mg alloy sheet were coded into the simulation.

A simple two dimensional model was used to describe the deformation during the single shot peening process. Material properties data of Mg AZ31 alloy sheet was obtained from the tensile test results in chapter 4.5. The young's modulus was set as 45 GPa and Poisson's Ratio was set as 0.3. The yield strength was set as 155 MPa, and the

UTS was set as 350 MPa. During the ultrasonic shot peening process, the speed of shot was set as 3.5 m/s according to previous study (Yin et al., 2015). To simplify the shot peening result, the shot is peened once. The stress field and the strain field during the shot peening and after the shot peeing process is calculated.

The V-bending process was also simulated by a simple two dimension model. For the the V-bending process, a gradient mechanic strength from the top surface to the center of the sheet was set. The plasticity properties of the as-received and the USSP treated materials were obtained from the tension test resulting in chapter 4.5. For the USSP treated AZ31 Mg alloy, a gradient nano structure was set by the virtual temperature technique. A continuously variable temperature field was assigned and a one-to-one relationship between temperature and mechanical properties was created. The other thermal parameters, such as conductivity factor, were set as zero to ensure the temperature did not change during the bending process. By this method, the gradient mechanical properties at the top surface were achieved. The load distance was set as 4 mm and the stress field and the strain field after bending would be calculated.

3.12 Quasi in-situ EBSD experiment

A quasi in-situ EBSD experiment was setup to investigate the V-bending process. A self-made in-situ EBSD holder for the V-bending process was prepared and show in figure 3.4 (a). The distance between the gap was 10 mm. A sample with a thickness of 0.5mm, a length of 15 mm and a width of 3 mm was applied for the quasi in-situ EBSD experiment.

For the as-received AZ31 Mg alloy, the sample was cut from a 1mm thick AZ31 Mg alloy sheet. Then a polishing along the thickness was conducted to obtain the required thickness of 0.5 mm. For the USSP sample, the USSP was conducted to treat at the 1 mm thick sheet for 5 min to obtain a nanocrystalline structure. After that, the polishing process was applied at the untreated side and the sheet was polished to 0.5 mm. After that, the

needed in-situ EBSD sample was cut from the already thinner sheet by CNC machining. Before the in-situ EBSD experiment, The RD×ND plane of the sample was polished by SiC paper to 2000 grit and followed electro-polishing in an AC2 electrolyte, using a voltage of 20 V for 60 s at -20 °C.

The sample was placed at the center of the holder, which meant it would cross the 10 mm gap and was fixed by a screw. After that, the holder was placed at the stage to conduct the EBSD characterization. The placed position of holder is present in figure 3.4(b). The RD× ND plane was detected during the experiment. The EBSD was conducted at the center area of the RD × ND plane of the sample. Then the holder was taken out to apply the loading distance by the screw, the force direction (FD) is shown in white in figure 3.4 (a). In this study, two loading distances, 0.8 mm and 1.6 mm, were adopted to study the microstructure evolution during the bending process.

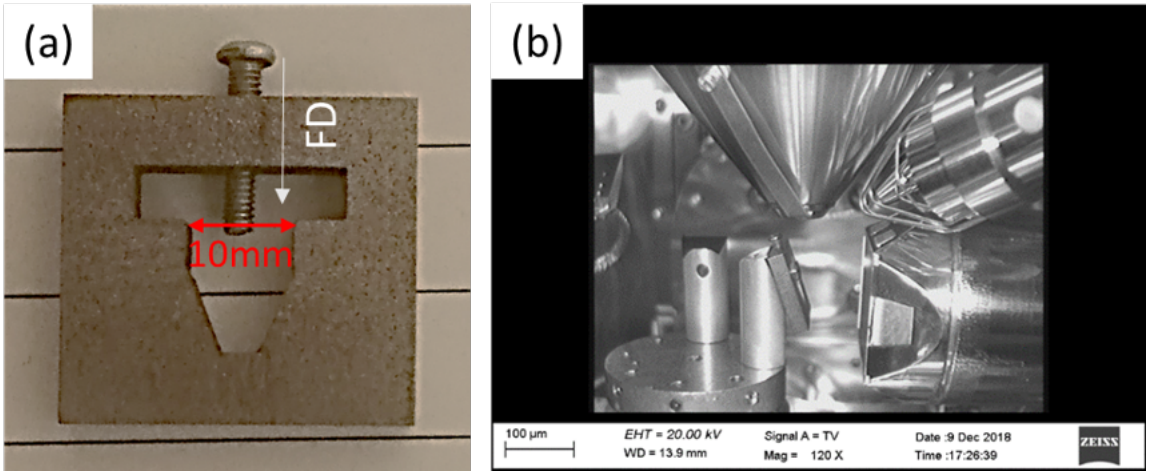

Figure 3.4. (a) the self-made in-situ EBSD holder and (b) The placed position of the holder during the in-situ EBSD experiment

3.13 Summary

This chapter introduces the framework and basic methodologies of the research. The ultrasonic shot peening process will be used to produce a surface nanocrystalline at AZ31 Mg alloy sheet. The induced stress and strain will be measured by XRD and simulated by the finite element method by ABAQUS software. The microstructure evolution during the ultrasonic shot peening process will be characterized by optical microscope, scanning electron microscopy, transmission electron microscopy, and electron back-scatter diffraction. The grain size, twins, grain orientation, surface topography will be described. Besides the microstructure evolution, the modified properties will also be studied. The effect of surface nanocrystalline on the microhardness and mechanical properties will be investigated. The surface sensitive properties: wear resistance and corrosion behavior will also conducted. Moreover, the deformation behavior after surface nanocrystalline during V-bending is measured.

CHAPTER 4. EXPERIMENTAL STUDY ON THE MICROSTRUCTURAL EVOLUTION AND MECHANICAL PROPERTIES OF AZ31 MAGNESIUM ALLOY SHEET AFTER ULTRASONIC SHOT PEENING

4.1 Introduction

This chapter presents the experimental study of the effect of ultrasonic treated time on the microstructural evolution and mechanical properties of AZ31 Mg alloy sheet. The microstructure includes the grain size, the grain orientation, the twin structures and surface roughness. In addition, the influence of ultrasonic treated time on the microhardness and mechanical properties is also studied. The relationship between the microstructure and the mechanical properties is discussed.

The results show that a great grain refinement can be achieved by the ultrasonic shot peening process. The grains have been refined to nanocrystalline at the topsurface and a random texture is also obtained after treatment. A twin structure is found below the nanocrystalline layer, and an untwined matrix with a residual stress below the twin structure. The increase of USSP treated time can increase the thickness of nanocrystalline as well as the surface roughness. The formed nanocrystalline leads to a higher micro hardness and a higher mechanical strength while the ductility is heavily reduced. The experimental results provide a basis for material properties of the USSP treated alloy which will affect the wear resistance in chapter 5, the corrosion resistance in chapter 6 and the bendability in chapter 7.

4.2 Experimental setup

The experimental material in this study was the commercial magnesium alloy-AZ31. The nominal composition was analyzed by an XRF-800 CCDE X-ray fluorescence spectrometer, and the result by weight percentage (wt. %) is shown in table 4.1. The as-received mg alloy was in the form of 3 mm thick sheet and small plate with a size of 55×55mm was cut from the sheet by a bend saw and subjected to the USSP process subsequently.

As shown in Figure 4.1, the experimental setup of USSP process consists of an ultrasonic signal generator, a transducer which translates the generated signals into mechanical motion and a simple metal rod which propels the shots. The Mg AZ31 alloy sheet with the thickness of 3mm used as the workpiece was fixed at the top of a cylindrical hollow steel container. The bottom of the cylindrical hollow steel container was a horn with a diameter of 20mm, and the shot was placed between the horn and the workpiece. The shots used in this study were 3 mm in diameter. The distance between workpiece and the horn was 10 mm. The shots were powered by the horn with a frequency of 20KHz.

Table 4.1. The nominal composition of as-received AZ31B Mg alloy

element	Al	Zn	Mn	Mg
composition	3.1	0.8	0.3	Balanced

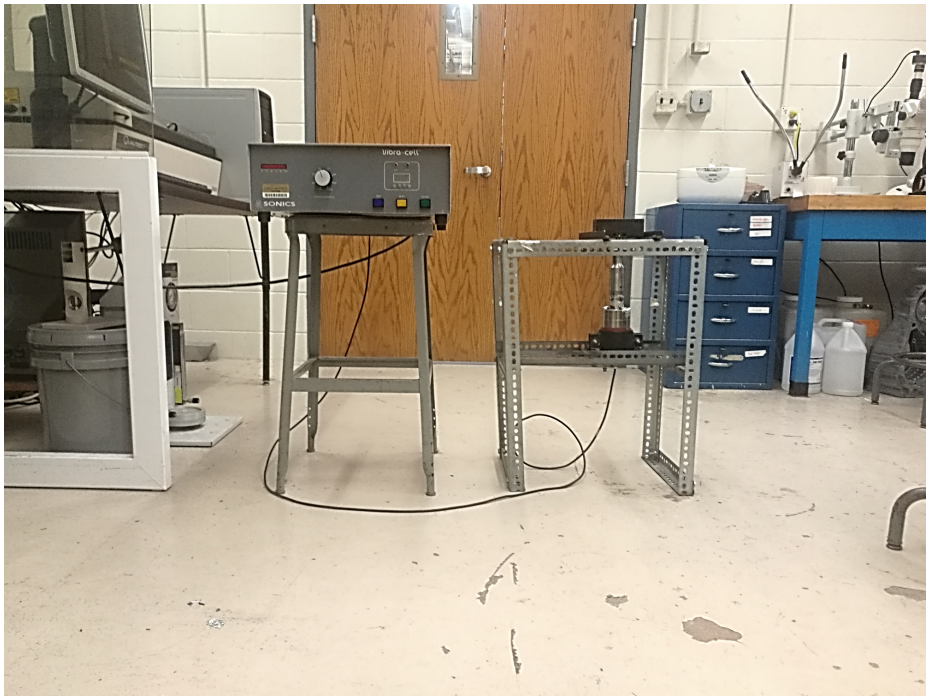

Figure 4.1. Experimental setup of the ultrasonic shot peening process equipment

4.3 Characterization of the microstructural evolution

4.3.1 The characterization of microstructure evolution by optical microscopy

The as-received AZ31 Mg alloy sheet was annealed at 200°C for 3 hours to remove the residential stress after rolling and to get a homogeneous microstructure. Figure.4.2 (a) shows that the annealed microstructure of the annealed AZ31 Mg alloy sheet is of a uniform microstructure. The grains are homogenous and equiaxed. The grain distribution is present in figure.4.2 (b). It can be seen that the average grain size of the sample is 8.9 μm. Most of the grains' size are between 5-10 μm.

The microstructure of the annealed sample after ultrasonic shot peening treatment is present in figure 4.3. The ultrasonic shot peening durations are 5 min (a), 10 min (b) and 15 min (c). The result shows that the top surface of the sample has been deformed heavily during the ultrasonic shot peening process. Due to the grain refinement, the grain

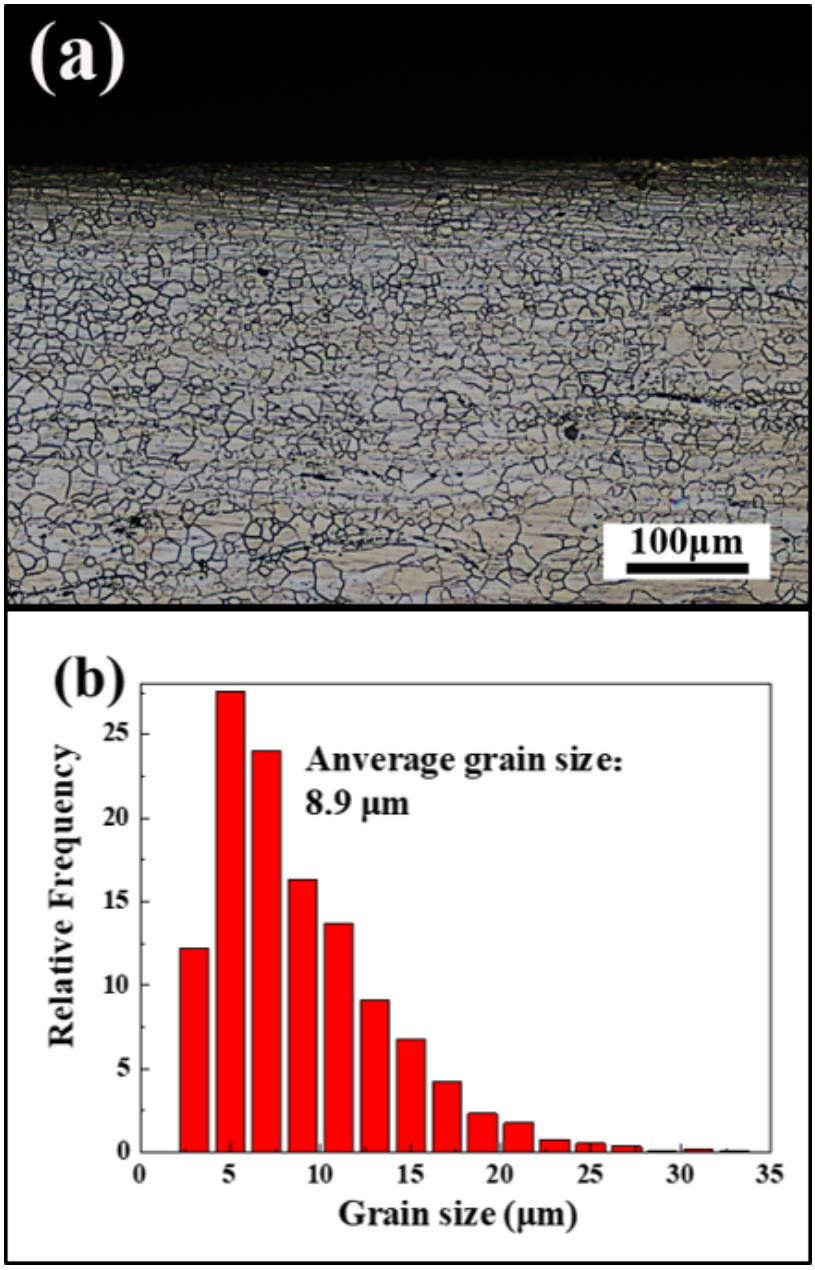

Figure 4.2. Microstructure of as-received AZ31 Mg sheet after annealed at 200°C for 3 hours (a) and the grain distribution (b)

boundary of the top surface cannot be etched and seen in OM. This boundary-invisible surface layer with a dark appearance is the refined layer during the ultrasonic shot peening. With the increase of shot peening time, the thickness of boundary-invisible layer

increases. The thickness of the boundary-invisible layer after 5 min, 10 min and 15 min is 51m, 79m and 145m, respectively. It can be seen that the longer shot peening time will induce more deformation to the material and change the microstructures of the materials at the deeper area.

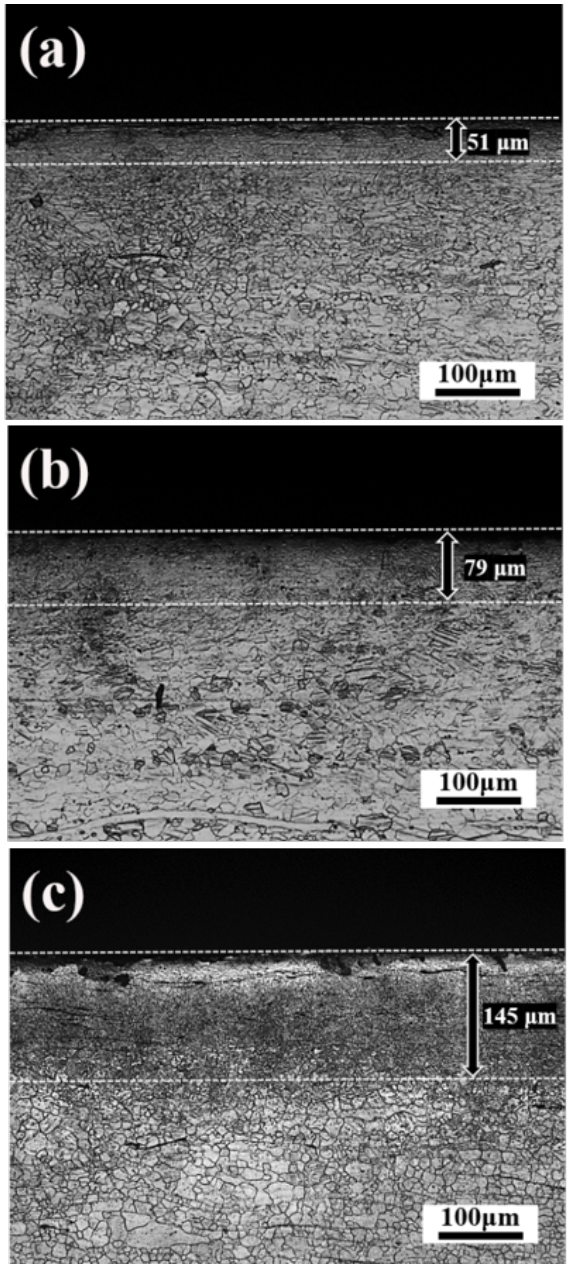

Figure 4.3. Microstructure of as-received AZ31 Mg sheet after ultrasonic shot peening for 5 min (a), 10min (b) and 15 min (c)

The appearance of this boundary-invisible layer during ultrasonic shot peening process is due to the significant grain refinement to nanocrystalline and dynamic recrystallization (DRX) occuring. This refined nanocrystalline cannot be resolved under this magnification.

4.3.2 Crystallographic orientation and grain size

The X-ray diffraction was conducted to analyze the crystallographic orientations and the grain size of the topsurface after ultrasonic shot peening process. Figure 4.4 shows the XRD patterns of the as-received AZ31 Mg alloy sheet and after the USSP treatment for 5 min, 10 min and 15 min.

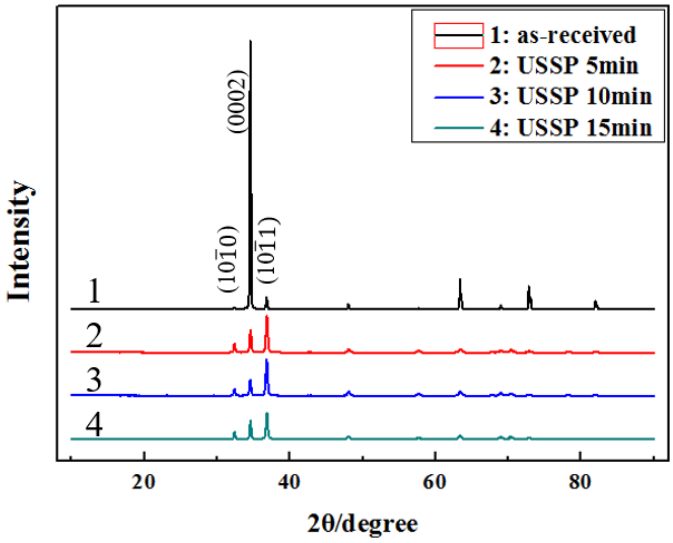

Figure 4.4. XRD patterns of as-received rolled sample and the USSP treated samples

According to the XRD result, only the peak of α-Mg is detected in these four XRD patterns. For AZ31 Mg alloys, the content of alloy element is relatively low and the solubilities of Al and Zn elements into Mg matrix are relatively high at room temperature, resulting in the formed second phase is relatively few. Moreover, the AZ31 alloy was annealed and hot rolled to produce the sheet, which led to the re-dissolution of second phase. So the left second phase in hot rolled AZ31 sheet is quite few, and its diffraction

peak cannot be detected. For the as-received AZ31 rolled sheet, the main peak is the (0001) peak, and the intensity of $(10\bar{1}0)$ and $(10\bar{1}1)$ is much lower. The result implies that the as-received rolled sheet has a strong basal texture (Styczynski, Hartig, Bohlen, & Letzig, 2004). This is because of the limited slip system of Mg and the grains with non-basal orientation will be consumed during rolling or extrusion(Z. Yang, Li, Zhang, Lorimer, & Robson, 2009). After USSP, the peaking of (0001) is reduced greatly and the peaks of the USSP treated sample are relatively strong at $(10\bar{1}0)$ and $(10\bar{1}1)$, which implies that the formed nanocrystalline after USSP treatment has a relatively random grain orientation. Meanwhile, the full width half maximum of the peaks after USSP becomes larger. Such a large full width half maximum is related to a smaller grain size after USSP. The grain size can be evaluated by the XRD analysis, according to the Williamson-Hall formula:

$$d = \frac{k\lambda}{\beta \cos(\theta)} \tag{4.1}$$

where d is the grain size, K is the Scherrer constant (0.9), λ is the x-ray wavelength, β is the full-width-half-max(FWHM) of the peaks and θ is the diffraction angle. The measured grain size is present in figure 4.5. The average grain sizes of USSP treatment for 5 min, 10 min and 15 min are 45nm, 42 nm and 37nm, respectively.

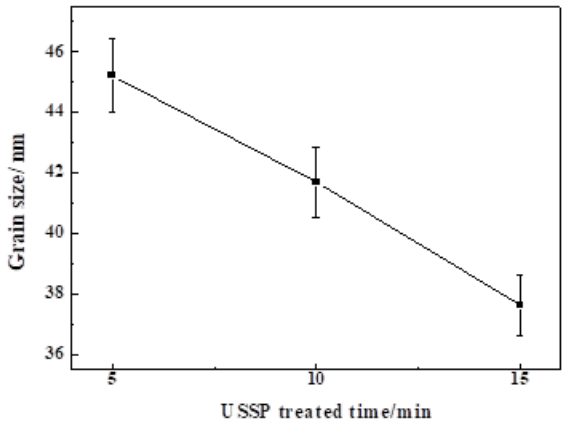

Figure 4.5. The grain size of topsurface after the USSP treated sample for 5 min, 10 min and 15 min

4.3.3 Characterization of nanocrystalline by TEM

The formed nanocrystalline on the top surface was characterized by TEM. The TEM sample was cut by FIB from the 10 min treated sample. The position of this TEM sample was about 20 μ m from the top surface, shown in figure 4.6 (b).

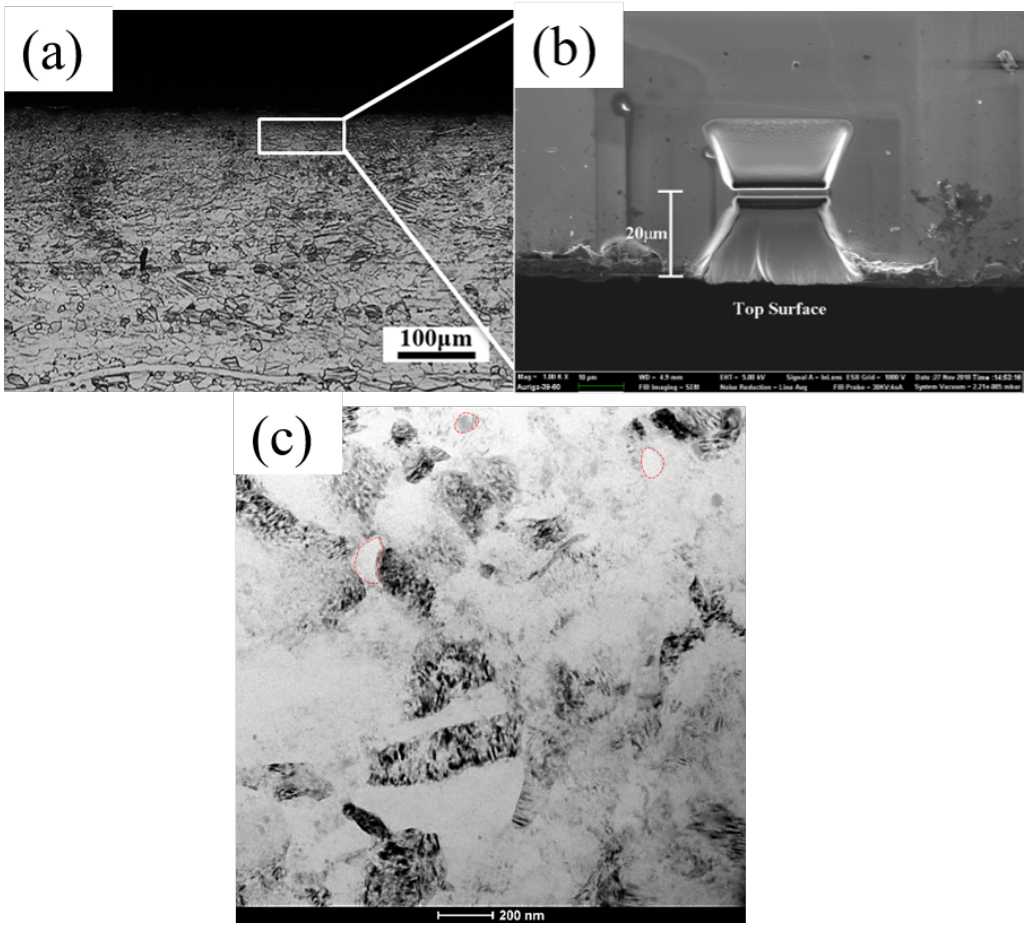

Figure 4.6. (a) The position of FIB cutting position in Optical microscopy; (b) the position of TEM sample in SEM; (c) Bright-field TEM image showing the microstructure of the USSP 10min treated sample from the top surface of 20 μm

In figure 4.6(c), the typical bright-field TEM image of the top surface layer after 10 min treatment. Obviously, a nanostructure is developed after USSP treatment. In figure 4.6(c), there are two kinds of morphology found: lamellar nanocrystalline and equiaxed nanocrystalline. The majority of the grains are lamellar nanocrystalline and a small part of

equiaxed nanocrystalline distributed among them. The equiaxed nanocrystalline has been refined to less than 100 nm. During the USSP process, the top surface undergoing a high strain and high strain rate induced the formation of a high dislocation density and dense dislocation walls with spacing in the nanometer regime. The further developing of dislocation walls resulted in the appearance of lamellar subgrains of nano-sized width and these lamellar subgrains eventually transformed into equiaxed nano-sized grain (Azadmanjiri, Berndt, Kapoor, & Wen, 2015). Here, both the lamellar nanocrystalline and equiaxed nanocrystalline are found. It can be inferred that the area with distance from the topsurface less than 20μm will have more equiaxed nanocrystalline because of the higher strain rate.

4.3.4 Surface Roughness

The three-dimension surface topography of the ultrasonic shot peening sample is displayed in figure 4.7. The measured area was 2.5 mm $\times$ 2.5 mm. The top surfaces are quite rough after the ultrasonic shot peening treatment. The surfaces are corrugated with deep, narrow valleys and peaks after shot peening, and the roughness increased with increasing shot peening duration time. The related surface roughness parameters are list in table 4.2.

R_a presents the arithmetic average value of the filtered roughness profile and is the most used parameter to present the surface roughness. It can be seen that the R_a of ultrasonic shot peening 5 min, 10 min and 15 min are 5.934 μm, 6.161 μm and 6.236 μm, respectively. The longer shot peening duration will result in a more coarse and rough surface, but the increment is limited. The maximum peak heights (R_p) of ultrasonic shot peening 5 min, 10 min and 15 min are 33.935 μm, 31.644 μm and 36.756 μm, respectively. For the maximum valley depth (R_v), it increases from 33.228 μm at 5 min, to 35.79μm at 10 min and 38.64 μm at 15 min. The mean of the width of the curve valleys (R_{sm}) also increases at longer ultrasonic shot peening durations. The R_v and R_{sm} can better

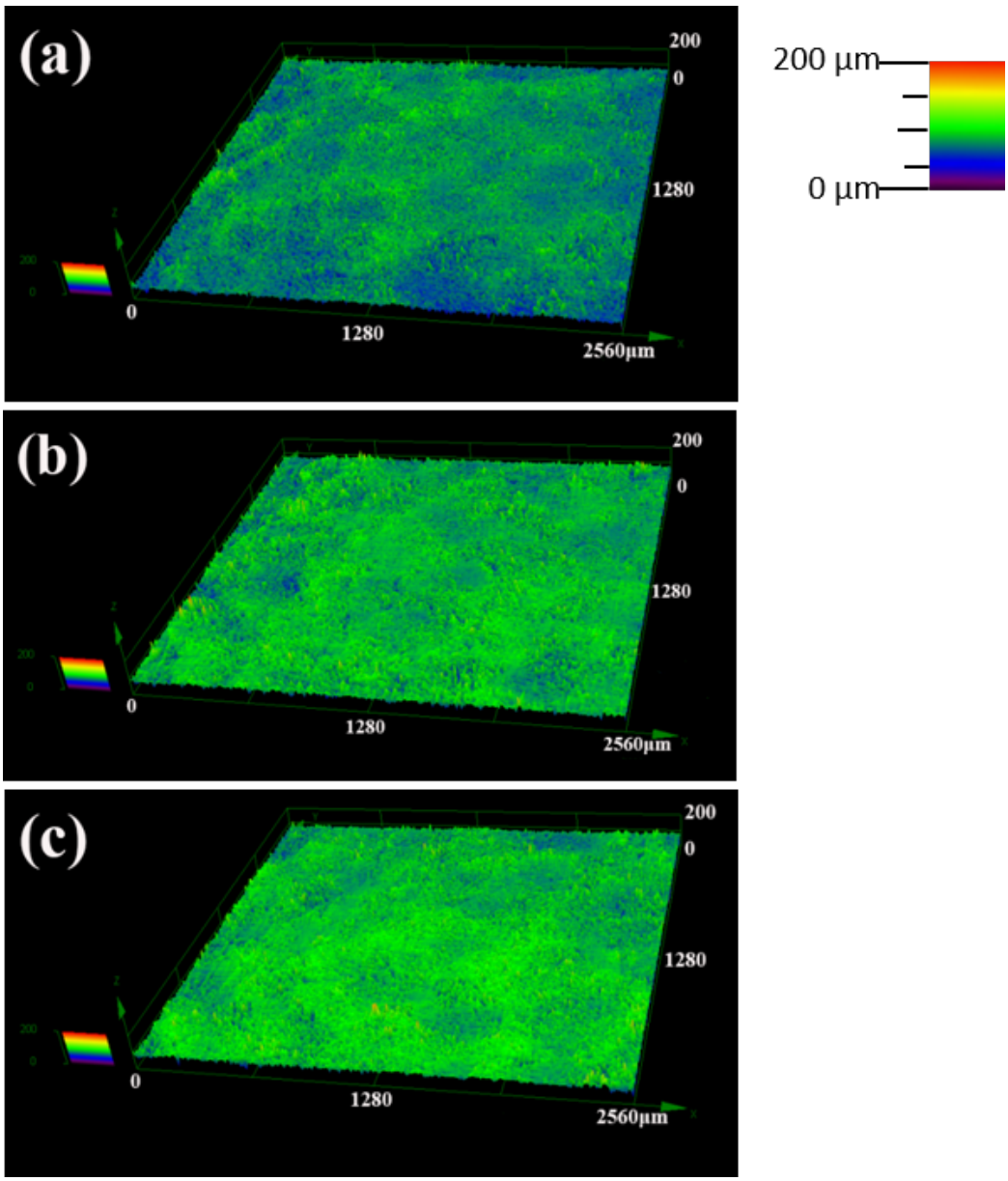

Figure 4.7. The top surface morphology of USSP treated AZ31 alloy: (a) 5min, (b) 10 min and (c) 15min, characterized laser confocal microscopy

present the effect of the shot peening on the surface because a long duration of repeated hits of the shot to the surface will make the valley deeper and wider. It can be seen that the induced USSP treatment results in a rough surface after 5 min treatment and the increment of roughness is very limited with further increasing the shot peening duration.

Table 4.2. The surface roughness parameters of the USSP treated samples

USSP time/ min	$R_a/\mu m$	$R_p/\mu m$	$R_v/\mu m$	$R_{sm}/\mu m$
5min	5.934	33.935	33.228	55.956
10min	6.161	31.644	35.49	57.327
15min	6.236	36.756	38.64	65.15

4.3.5 The EBSD Characterization of Microstructure Evolution

Even though the deformation area and twins can be clearly observed in optical microscopy, EBSD is superior to observe and highlight the depth of the deformation area and the location of the deformation twins. The cross-section of the ultrasonic shot peening treated sample is characterized by EBSD to better analyze the microstructure and texture evolution, shown in figure 4.8. The observed direction is the transverse direction. The inverse pole figure (IPF) maps, the twins, low angle grain boundary and high angle grain boundary, the Kernel Average Misorientation (KAM), and the band contrast maps are present.

For the USSP treated sample in figure 4.8, the cross-section consists of three parts: (1) the nanocrystalline region which is the white part at the top surface; (2) the transition region at which the grains are heavily fragmented and has a lot of twin structure; (3) the deformed region which is simply deformed and influenced by the residual stress. For the Mg matrix, we can see that all the inverse pole figure (IPF) maps of the undeformed areas present an orientation of the mix of $(11\bar{2}0)$ and $(10\bar{1}0)$ directions. As the observed direction is the TD, it can be implied that the as-received AZ31 Mg alloy sheet presents a strong basal texture, which is consist with the XRD result. For the ultrafine grain region, the USSP process will induce a high strain to the top surface of the AZ31 Mg alloy sheet. This high strain rate will result in an obvious grain refinement and create a nanocrystalline. For the top surface area, these grains have been refined to about 40 nm,

which is unable to be detected by EBSD at this magnification. Meanwhile, a lot of residual stress still exists after USSP, which also impedes the EBSD characterization. That is why the top area is white and unable to be characterized. For the transition region, there are a lot of twin structures and low angle grain boundary (LAGB). According to the previous report, the twin structure forms first, during the grain refinement induced by USSP(H. Sun et al., 2007). In the USSP treated Mg alloys, the formed twin by the USSP treatment is $(10\bar{1}2)$ tensile twin. This is because of the smaller twin shear (s=0.1302) of the $(10\bar{1}2)$ tensile twin and low CRSS values of $(10\bar{1}2)$ tensile twin, which is 2.4 MPa (Matsubara et al., 2003)(Bian & Shin, 2013).

In this study, the as-received AZ31 Mg sheet presents a strong basal texture. The impacted direction of the shot is parallel to the C axis of its HCP structure. This direction favors the formation of the $(10\bar{1}1)$ compression twin while there are few $(10\bar{1}1))$ compression twins formed. The reason is that the direction of the flying ball is multidirectional during the USSP process, not just perpendicular to the top surface. Meanwhile, the formed strain and stress during the deformation process are not a specific point but an area. The CRSS values of $(10\bar{1}1)$ compression twin is 114 Mpa, much higher than that of $(10\bar{1}2)$ tensile twin (H. Zhang, Huang, Roven, Wang, & Pan, 2013). This multidirectional compact and the difference between the CRSS values results in the formation of $(10\bar{1}2)$ tensile twin. Below the transition region, there will be the deformed region. Few twin structures are found in inverse pole figure (IPF) maps at this region. However, this region is still influenced by the residual stress, which is found from the Kernel Average Misorientation (KAM) maps. In KAM maps, the grain orientation spread (GOS) of each grain in the EBSD scan area is present. The distribution of the residual stress along the depth can be clearly estimated.

For the 5 min USSP treated sample in figure 4.8(a), the microstructural evolution along the depth is uneven. For the white ultrafine grain region, some areas near the top surface still present a detectable orientation, which means these areas are not refined to nanocrystalline. Meanwhile, some areas are distributed at a depth of 100 μm. Beneath the refined region is the transition region and a lot of $(10\bar{1}2)$ tensile twins are observed and outlined by red here. The $(10\bar{1}2)$ tensile twins are mainly distributed next to the white

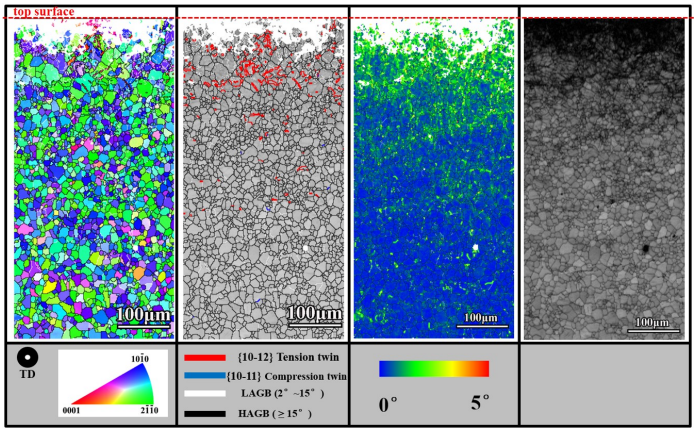

(a) USSP for 5min.

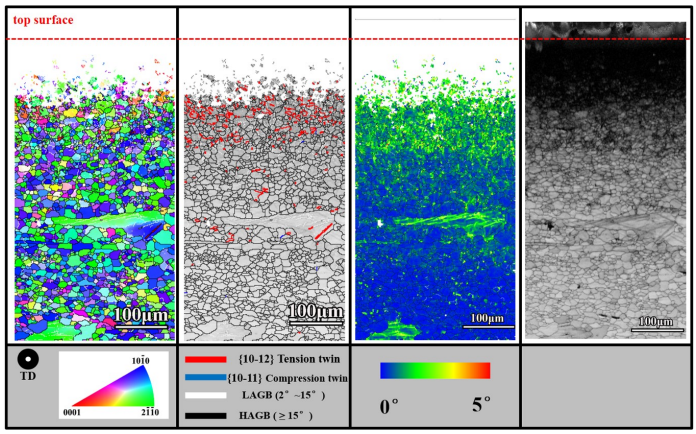

(b) USSP for 10min.

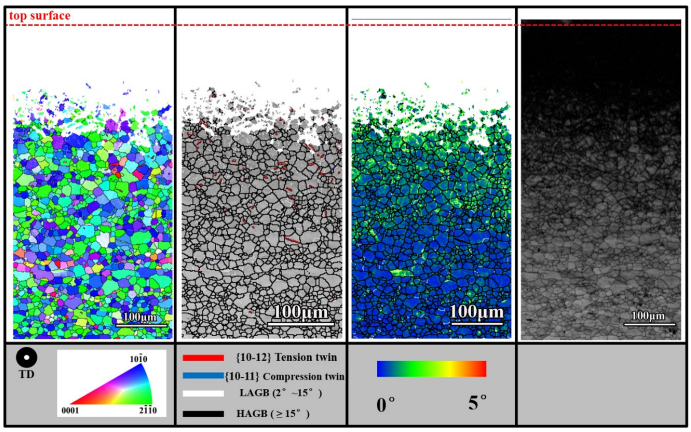

(c) USSP for 15min.

Figure 4.8. The EBSD characterization of the microstructure from the TD direction after ultrasonic shot peening for 5 min (a), 10 min (b) and 15 min (c)

ultrafined grain region from the top surface. No $(10\bar{1}1)$ compression twins are found in this region. From the KAM map, it can be seen that the transition region is covered by the residual stress and the residual stress is far beyond the distribution of the $(10\bar{1}2)$ tensile twins. These untwined places at the transition region also have a deformed strain. Also, the distribution of residual stress is uneven. In the deformed region, the original grains are simply deformed, and the residual stress is reduced. There are few tensile twins found in the deformed region.

For the 10 min USSP treated sample in figure 4.8(b), the microstructural evolution becomes even. For the nanocrystalline region, the white area becomes thicker and more even than that of the 5 min treated sample along the thickness, implying the heavy deformation becomes uniform after a longer treat time. With the increase of treated time, the area which is the transition region in the 5 min treated sample becomes the nanocrystalline region. Meanwhile, the formed transition in 10 min sample can be as far as 200 μm from the top surface. In the transition region, still a lot of $(10\bar{1}2)$ tensile twins are found. In its KAM map, the transition region shows a higher level of residual stress, which is the same as the 5 min treated sample. The distribution of residual stress in the deformed region is also close to that in the 5 min treated sample.

For the 15 min treated sample in figure 4.8(c), the nanocrystalline region enlarges to a thickness of ~ 230 μm, which is close to the depth of the transition region in the 10 min treated sample. Beneath the nanocrystalline region, there are fewer formed $(10\bar{1}2)$ tensile twins than that of 5 min and 10 min treated samples. The formed $(10\bar{1}2)$ tensile twins are regarded as the first step to become ultrafine grains or even nanocrystalline during the grain refinement. The fading away of the transition region implies that there is a limitation of the microstructure evolution thickness at this condition. The further increasing of treated time will have a limited effect on the thickness of nanocrystalline region. Even though the transition region is hardly found in 15 min treated sample, there is still a clear deformed region from the KAM map.

4.4 Mechanical properties

4.4.1 Microhardness

The microhardness distribution of the rolled AZ31 Mg alloy sheet with USSP treated for 5 min, 10 min and 15 min is shown in figure 4.9.

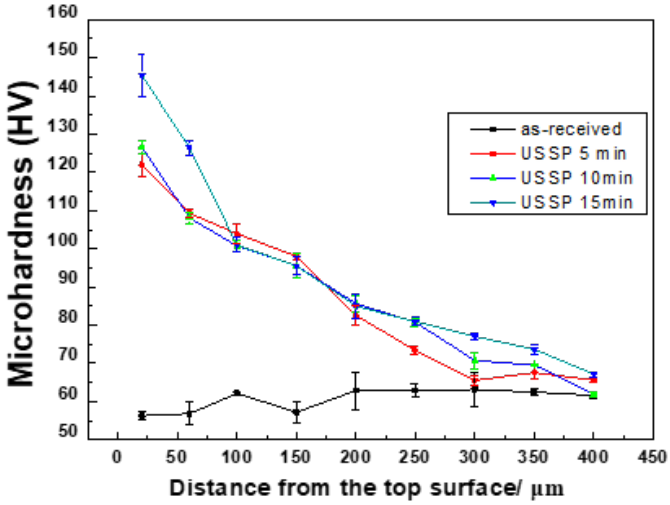

Figure 4.9. The distribution of the microhardness as a function of distance to the top surface after ultrasonic shot peening for 5 min, 10 min and 15 min

For the as-received Mg alloy sheet, the microhardness is distributed uniformly along the depth, with a microhardness of $\sim$ 61 HV. For USSP 5 min treated sample, its microhardness is improved to 123 HV, twice of the microhardness of the matrix, and decreases gradually to 65HV at the depth of 300 μm. For USSP 10 min treated sample, the microhardness at the top surface is enhanced to 127 HV, and gradually decreased to 65 HV along the depth. For the USSP 15 min sample, the microhardness is further improved

to 145 HV, and gradually decreased to 65Hv at the depth of 400 μm. It is apparent that the USSP treatment can improve the microhardness and the improvement is decreased along the depth. The effect area of USSP 5 min sample is 300 μm and can be further improved to 400 μm after a 15 min USSP treatment.

The improved microhardness may be attributed to the grain refinement. The USSP treatment resulted in a nano structure at the surface. As observed from OM, TEM and EBSD, the top surface was refined to nanocrystalline and a gradient nano structure along the depth was formed. According to the Hall-Petch formula, the finer the obtained grain, the higher the microhardness would be. The grain refinement and work hardening result in the improved microhardness. Meanwhile, the microhardness improved area is close to the distribution of residual stress. It can be inferred that the residual stress can also make a contribution to the hardness enhancement.

4.4.2 Tensile and Compression properties

The mechanical properties of the as-rolled and USSP treated (5 min, 10 min and 15 min) AZ31 Mg alloy sheet are shown in figure 4.10, and the values obtained from these curves are listed in table 2. The tensile test results in figure 4.10(a) indicate the tensile yield strength (TYS) of the as-rolled AZ31 sheet is improved greatly after USSP treated, from 127.7MPa to 162.4 MPa, 193.8 MPa and 153.4 MPa for 5 min, 10 min and 15 min USSP treatment, respectively. The ultimate tensile strengths (UTS) of the USSP treated alloys are also higher than that of the original alloy. The increments of UTS are 32 MPa, 51 MPa and 26 MPa for 5 min, 10 min and 15 min USSP treatment, respectively. However, the improved yield stresses after the treatment sacrifice the elongation of the original sheet. This changing tendency of mechanical properties is attributed to the strain hardening produced by the nanocrystalline at the top surface. The formed nanocrystalline leads to the accumulation and interaction of dislocations due to its higher percentage of grain boundaries and dislocations. What should be mentioned is that the USSP 15 min treated alloy presents a decreased stress and an improved elongation compared with 10 min treated alloy. The possible reason for this phenomenon is that there will be some

microcracks formed at the nanocrystalline layer after a longer treatment time. According to the previous report, the cyclic stress-strain load during the ultrasonic shot peening process resulted in a fatigue behavior of the material and the formation of microcracks at the top surface after the nanocrystalline has formed (Yin, Rakita, Hu, Sertse, & Han, 2017). The further induced energy during ultrasonic shot peening would result in the propagation of the microcrack because of the limited ductility and work-hardening. Another possible reason is the synergetic strengthening caused by the gradient effect. It is proposed that there may exist a particular volume fraction in this gradient nano structure that leads to a maximum strength improvement(Wu et al., 2014). H. Chen et al. (2017) reported that the optimized volume fraction in Mg alloy is probably between 9.3 and 14 pct. Here, the volume fraction of gradient structure after the 15 min treatment is 15.3 pct, which is above the proposed volume fraction. That may be one of the reasons of the reduced yield stress. The improved elongation may be the complex stress state at the interface of the matrix and the nanocrystalline and the generation of a three-dimensional stress state, leading to the activity of non-basal slip system (Meng et al., 2017).

The compression curves of the as-received and USSP treated alloys are present in figure 4.10(b). The compression yield stress (CYS) are improved from 77 MPa to about 100 MPa after 5 min USSP treatment, and no further obvious increment is found with the increase of treatment time. The ultimate compressive strength (UCS) and compression elongation are decreased after USSP treatment. The formed nanocrystalline would ruin the ductility of the alloy and result in a reduced compression elongation and UCS during compression. The similar CYS implies the fracture during compression has a limited relationship with the thickness of nanocrystalline. The CYS/TYS values after USSP treatment are not improved after USSP treatment and becomes even smaller when USSP time is 10 min because of the limited increment of yield during compression.

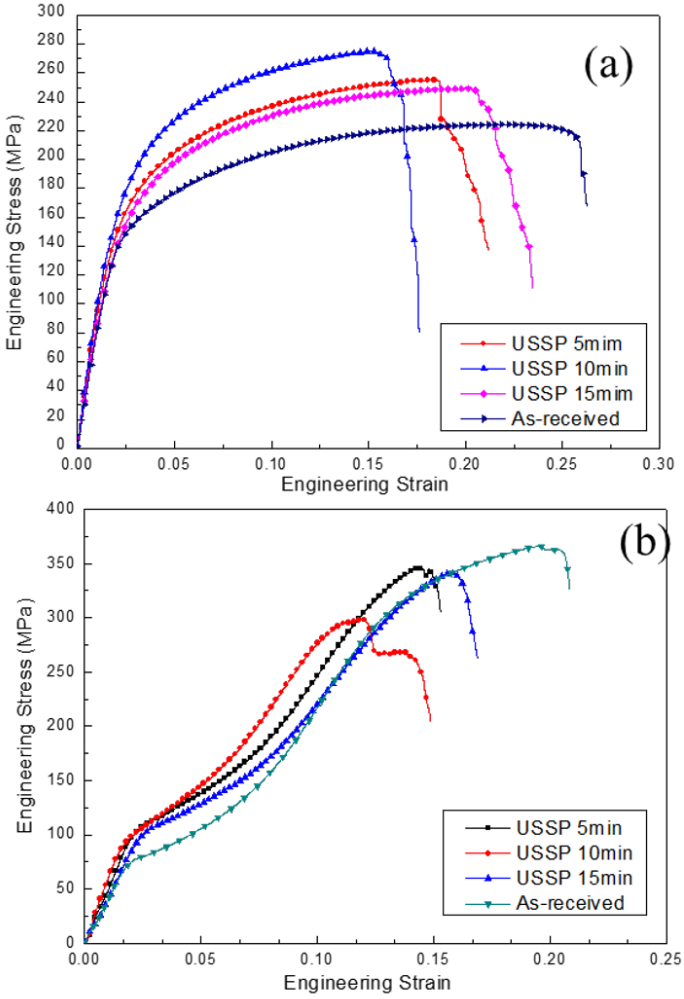

Figure 4.10. The engineering stress-engineering strain curves of various sheets with different USSP time during uniaxial tension (a) and compression deformation (b)

4.4.3 Fracture surface analysis

The tensile and compression fracture surface of the as-received and 15 min USSP treated samples are shown in figure 4.11. The tensile fracture surface of as-received AZ31 Mg alloy presents a typical ductile fracture, with dimples distributed in the matrix. For the USSP treated alloy, it is apparent that the tensile fracture along the depth has two patterns: the ductile fractures in the matrix and the brittle facture at the top surface. The top surface

Table 4.3. The tensile yield strength (TYS), ultimate tensile strength (UTS), tensile elongation (T-Eu), compressive yield strength (CYS), ultimate compressive strength (UCS), compressive elongation and CYS/TYS values of the various samples with different USSP time

Sample conditions	UTS (MPa)	TYS (MPa)	El (%)	CYS (MPa)	UCS(MPa)	C-Eu (%)	CYS/TYS
As-received	223.9	127.7	21.9	77	365.3	14.3	0.61
USSP 5min	255.2	162.4	15.6	100.7	344.4	8.6	0.62
USSP 10min	275	193.8	12.3	103.6	298.3	7.2	0.53
USSP 15min	249.9	153.4	17.2	100.2	342.7	10.1	0.65

and the matrix in figure 4.11(b) are present by high-magnification SEM micrographs. The fracture surface of the nanocrystal (figure 4.11(c)) shows a similar pattern of brittle material. The fracture surface is very smooth, and few dimples are found. The fracture in the matrix (figure 4.11(d)) presents a similar fracture characteristic with as-received sample, exhibiting dimples. The ductile fracture of the matrix is the main reason of the still reasonable ductility of the USSP treated sample. The result suggests that the main contributor of the ductility is the untreated matrix and the nanocrystalline at the top surface is apart in a brittle way, which is consistent with the high yield strength and the high microhardness at the surface. Moreover, the fracture at the interface between the nanocrystalline and the matrix is shown in figure 4.11(e). A lot of small dimples with a diameter of 1μm can be easily identified, suggesting the ductile fracture at the interface. The lateral fracture surface of the 15 min USSP treated sample after compression is shown in figure 4.11(f). The angle between the load direction and the formed crack is about 50^o, close to 45^o, because the shear stress is at the maximum along the 45^odirection. Meanwhile, the crack formed at the untreated surface rather than the USSP treated surface because of the low strength of the untreated surface. The higher mechanical strength of the nanocrystalline can restrain the formation of cracks during compression. The compression fracture surface of the 15 min USSP treated sample is present in figure

4.11(g). There are also two different fracture patterns along the depth: the brittle fracture at the nanocrystalline and the ductile fracture at the matrix. There are a lot of steps on the matrix fracture section. For the brittle fracture section, the surface is very clean, and no such kind of steps are found.

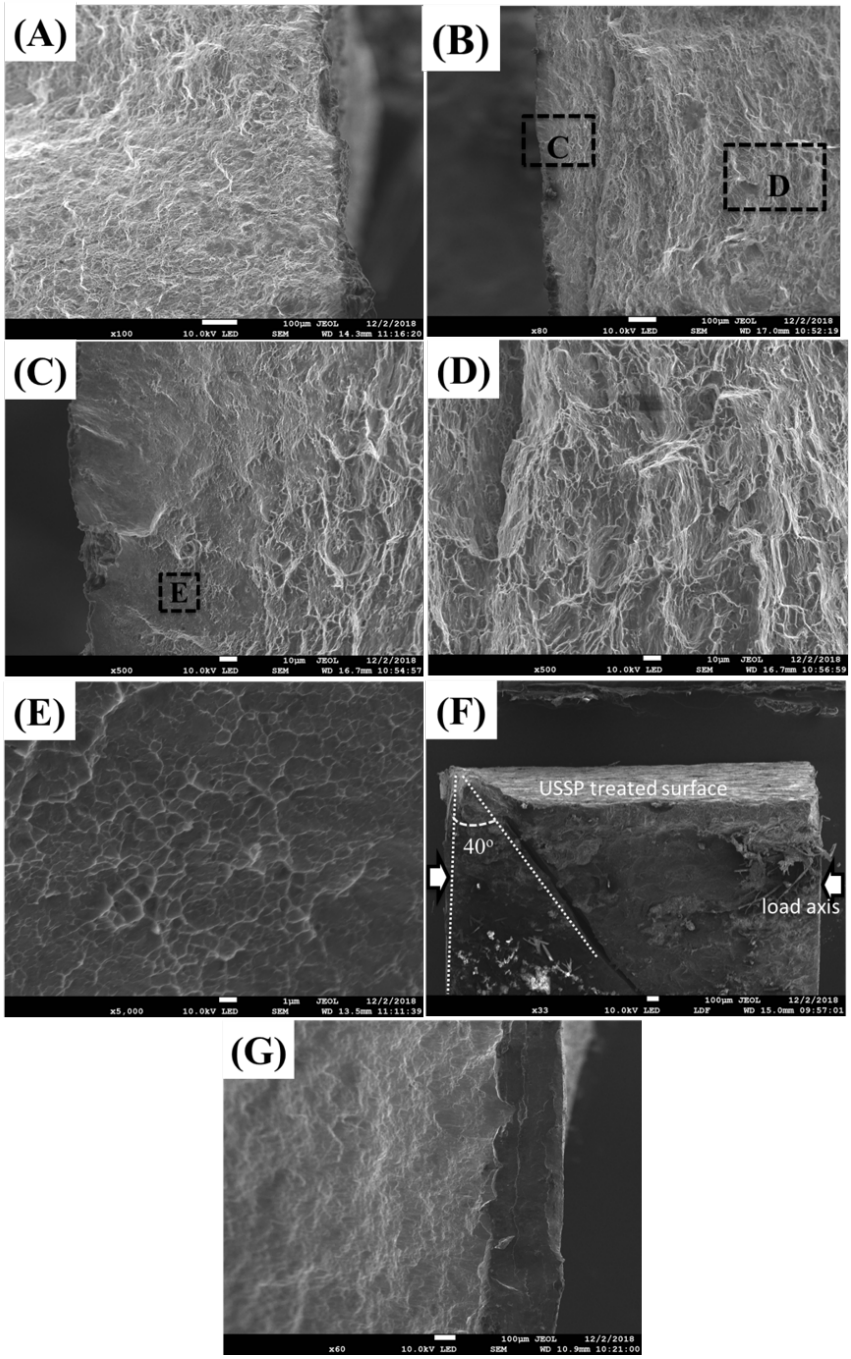

Figure 4.11. SEM micrograph of the fracture surfaces from as received tensile sample (a), USSP tensile sample (b-e), the lateral (f) of USSP compression sample and fracture surface (g)

4.5 The simulation of USSP process by Finite Element Method

A two-dimensional finite element simulation model was developed on the ABAQUS platform to simulate the impact process between the shot and the Mg alloy sheet surface during USSP process. According to previous research, the average value of the shot velocity was 3.6 m/s. The chosen diameter of the shot was 3mm. The test material was AZ31 Mg alloy. The Youngs modulus, density and Poissions ratio of the peened material was 45GPa, 1800 kg/m^3 and 0.3, respectively. The plasticity properties of the peened material were obtained from the tension test results in chapter 4.5. The shot material was S550 commercial stainless steel. The hardness of the stainless steel was much higher than that of the peened material. So, during the simulation process, the peened material was set as a deformable body and the shot as a rigid body. The mesh size was set as 0.02 mm and the set simulated time was 1e-4s. The explicit solver was applied here to simulate the USSP process. In figure 4.10, the simulation result of the equivalent plastic strain (PEEQ) and the mises stress are illustrated. The maximum PEEQ after a single impact is 2.23e-01mm and the maximum mises stress is 1.935e+02. From the result, it is obvious that there would be an induction of residual stress during the shot peening process and the distribution of the mises stress is much deeper than that of PEEQ.

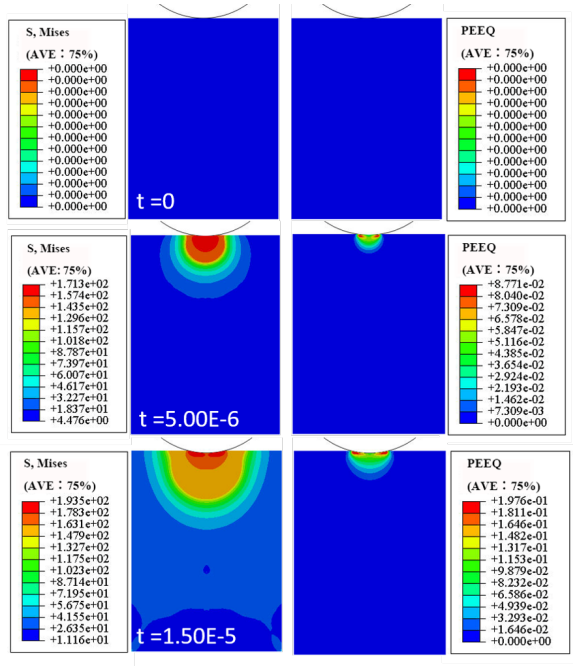

(a)

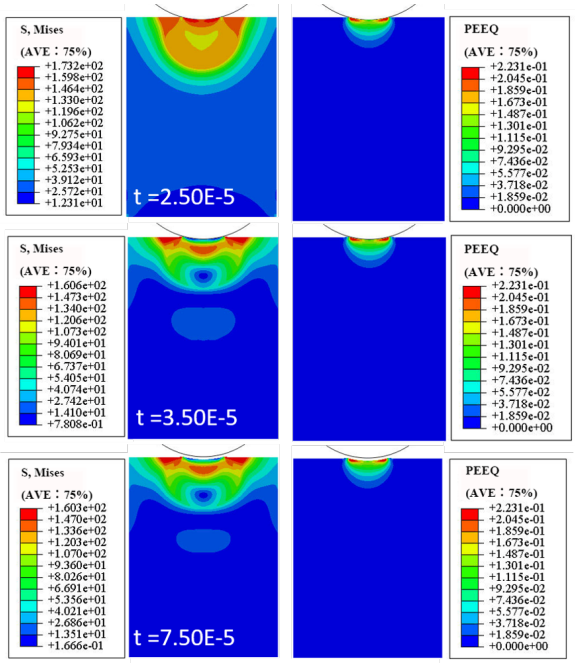

(b)

Figure 4.12. Finite element analysis of stress and strain of AZ31 Mg alloy after ultrasonic shot peening

4.6 Summary

The effect of the USSP treated time on the plastic deformation, microstructure evolution and mechanical properties of AZ31 Mg alloy rolled sheet during the ultrasonic shot peening process was investigated in this section. The microstructure evolution includes the grain size, surface roughness, the crystalline orientation and the distribution of residual stress. The mechanical properties include the microhardness, the tensile and compression properties. The following are the major observations from this chapter:

A gradient nanostructure was achieved at the top surface during the ultrasonic shot peening process. The grain at the top surface was refined to 45nm after 5 min USSP treatment, and further refined to 42 nm and 37nm for 10 min and 15 min treatment. A lamellar nanocrystalline was below the top surface along the depth. A lot of $(10\bar{1}2)$ tensile twin structures were found at the heavily deformed grains below the nanocrystalline layer. The untwined matrix still underwent a deformed strain.

A rough surface was achieved at the top surface after USSP treatment. The surface roughness (Ra) of the 5 min treated sample was 5.934 μm and increased to 6.161 μm and 6.236 after 10 min and 15 min treatment.

A residual stress was induced during the USSP process and the simulation results showed the distribution of residual stress was much wider than the strain. The distribution of the residual stress was simulated by FEM method and observed by EBSD.

The microhardness of the USSP treated samples was increased greatly compared with the as-received sample. The microhardness was increased from $\sim$65 HV of the as-received sample to 123 HV, 127HV and 143 HV of USSP 5min, 10 min and 15 min samples, respectively. The microhardness was attributed to the grain refinement, the work hardening and the residual stress.

The tensile stress and compression stress were improved remarkably after USSP treatment while the elongation was sacrificed. The yield stress was improved from 127.7 MPa to 198 MPa after a 10 min USSP treatment. The improved mechanical stress was attributed to the grain refinement and the work hardening. The increased USSP time from 10 min to 15 min would induce microcracks at the nanocrystalline layer, which decreased

the mechanical stress. The compression stress was improved from 73 MPa to 100 MPa after the 5min treatment and further increases of the USSP treated time did not improve the yield stress. The compression yield stress was limited by the yield stress of the untreated surface, so the thickness of the nanocrystalline had little effect on the compression yield stress.

CHAPTER 5. EXPERIMENTAL STUDY ON TRIBOLOGICAL BEHAVIOR OF ULTRASONIC SHOT PEENING TREATED AZ31B MAGNESIUM ALLOY

5.1 Introduction

As a future structural material because of its low density and high specific strength, Mg alloys are promising to replace other metals in the future. The poor wear resistance of Mg alloys strongly limits the further application of Mg alloys as a structural material. Surface hardening is an effective way to improve the wear behavior of Mg alloys. From the results in chapter 4, the surface hardness of Mg alloys after USSP treatment is substantially enhanced. So it is necessary to investigate the effect of USSP treatment on the wear resistance of Mg alloys and value if USSP treatment a promising and potential way to improve its wear resistance.

In this chapter, the wear resistance of AZ31 Mg alloy sheet before and after USSP treatment is investigated. The wear resistance is measured by a ball-on-disk wear test. Two sliding speeds (0.5m/s and 0.1m/s) and three applied load values (10N, 30N, and 50N) are applied to study the wear behavior. The coefficient of friction, the 3-D morphology after wear, the SEM picture of wear surface and the weight loss are measured to evaluate the wear resistance.

The results show that the USSP treatment leads to an improved wear resistance, compared to as-received one. The coefficient of friction, the wear rate and the worn surface roughness are reduced after USSP treatment. The improved wear resistance is attributed to the improve surface hardness. The wear morphology of the worn surface indicates there is a difference between the as-received and USSP treated AZ31 Mg alloy. The USSP treatment leads to the transition of wear regimes to a higher sliding speed and higher applied load, which widens the safe operation region of the material.

5.2 Experimental setup

The dry wear test was performed on a ball-on-disk wear testing machine at room air temperature. The sliding speed was 0.5m/s and 0.1m/s and the applied load was 10N, 30N, and 50N, the sliding distance was 100m. The steel bearing ball (ϕ= 10 mm) was selected as the friction pair. From the mircrohardness test in chapter 4, the USSP 15 min treated sample has the highest hardness at the top surface, and the formed nanocrystalline is thickest. So, only the USSP 15 min treated sample is used to study the wear resistance of the USSP treated sample. Each sample condition is tested three times for replicability.

5.3 Tribological behavior

5.3.1 The coefficient of friction

In Figure 5.1, the coefficient of friction (COF) of the as-received and USSP treated AZ31 Mg alloys is present as a function of the sliding distance under different applied loads (10N, 30N, and 50N). It is apparently found that the COF is unsteady during the sliding tests under the applied force. The coefficient of friction at the speed of 0.1 m/s and the applied force of 10 N presents a severely unstable fluctuation. With increasing the applied force, the fluctuation of COF is reduced. Both the as-received and USSP treated samples present a slight increase of COF at the beginning, which is due to the removal of surface impurities (Chang, Wang, Chang, & Wu, 2004). After the short running-in period, the COF presents a decline trend during the wear process. The COF of the USSP treated sample is obviously lower than that of the as-received under various applied loads.

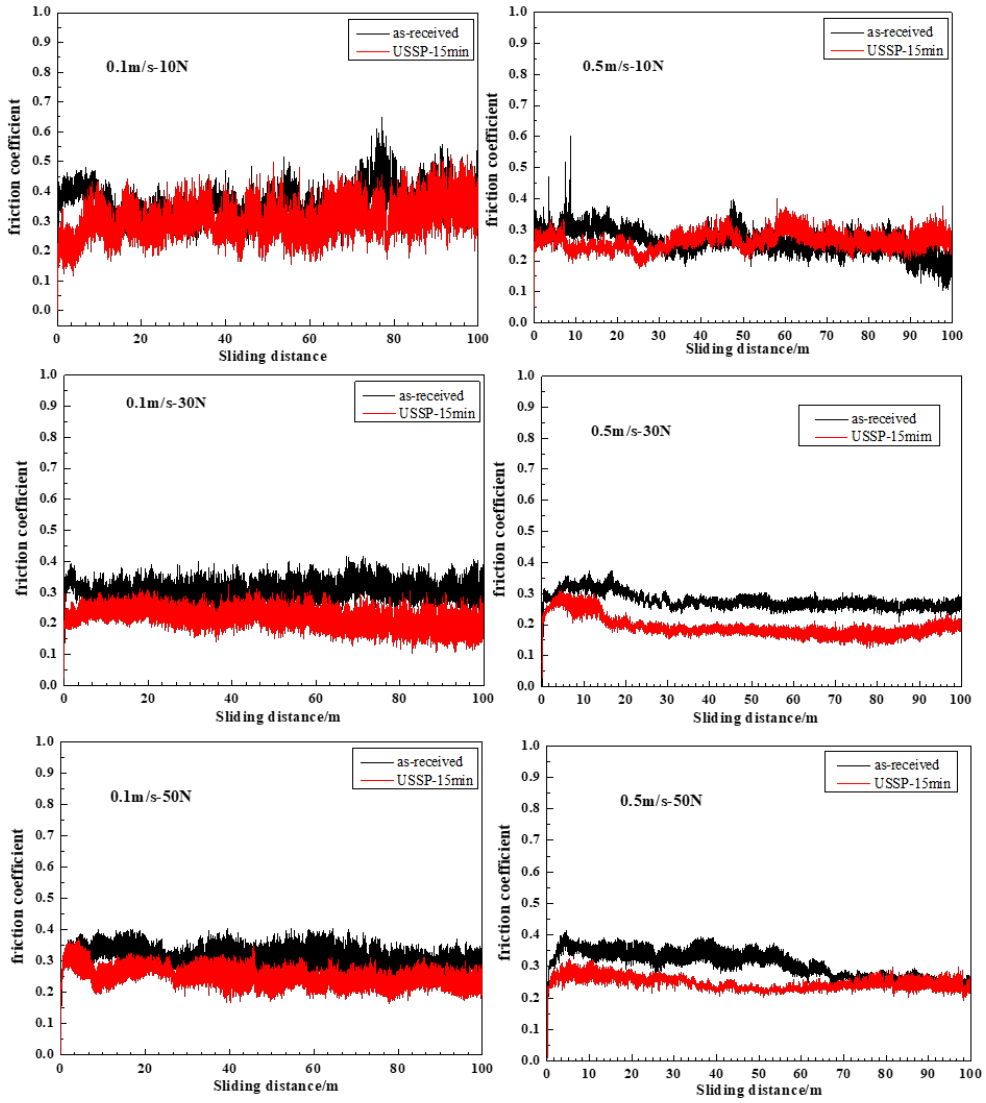

Figure 5.1. The variation of coefficient of friction of AZ31 Mg alloy before and after USSP treatment under different applied loads and different sliding speeds.

5.3.2 Wear rate

The wear rate (the wear volume loss per unit sliding distance) of AZ31 Mg alloys before and after USSP treatment is shown in figure 5.2. The wear rate of the USSP treated sample shows lower values compared with that of the untreated under all wear conditions. Meanwhile, the increase of applied load or decrease of sliding speed leads to a higher wear rate in either USSP treated or untreated samples. What should be mentioned is that

the changing tendency of the wear rate under different sliding speeds is quite different. Under the sliding speed of 0.1 m/s and the load value of 10 N, the wear rate of the USSP treated is close to that of untreated, implying limited or no improvement of the wear resistance after nanocrystalline. With the increase of applied load, the difference of wear rate between the untreated and USSP treated enlarges, and the USSP treated sample shows a lower wear rate. Under the sliding speed of 0.5 m/s, the curve of the USSP treated is almost parallel to that of the untreated. The improved wear resistance after nanocrystalline is quite stable under different applied loads.

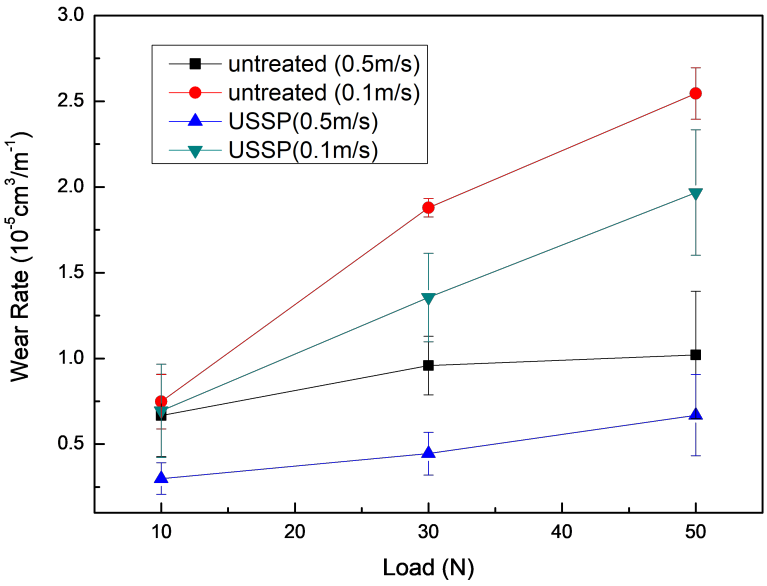

Figure 5.2. The variation of wear rate of AZ31 Mg alloy before and after USSP treatment under different applied loads and sliding speeds.

5.3.3 3-D surface profile

In order to verify the wear behavior of the USSP treated and untreated samples, the 3-D surface profiles of the worn surface are shown. The 3-D morphology of the wear surface Under the sliding speed of 0.1 m/s is present in figure 5.3. A typical wear track, with numerous ridges and grooves parallel to the sliding direction, is found. The wear surface roughness of the USSP treated sample is much lower than that of the untreated. The roughness of the wear surface decreases from 10.259 μm of the as-received to 6.102 μm of the USSP treated under a load of 10N. When the applied load increases to 30 N, the surface roughness of as-received increases to 14.046 μm and the USSP treated just increases to 9.223 μm. When the applied load further increases to 50 N, the surface roughness of the as-received and USSP treated becomes 18.123 μm and 10.98 μm, respectively. A lot of pile-up morphology is found in the interior of the scar of the as-received sample. This pile-up morphology is related to the plastic deformation of the wear surface. Meanwhile, a wide and deep groove is found at the bottom of the wear scar under the load of 50 N.

The 3D morphology of the wear surface under the sliding speed of 0.5 m/s is shown in figure 5.4. The surface roughness of the as-received and USSP treated under a load of 10N is 8.046 μm and 5.159 μm, respectively. Under a load of 30 N, the roughness of as-received is 9.894 μm and USSP treated is 8.189 μm. However, the surface roughness of as-received reduces to 9.123 μm under a load of 50 N and the USSP treated is 11.158 μm. The reduced surface roughness may be due to the change of wear mechanism of the as-received sample.

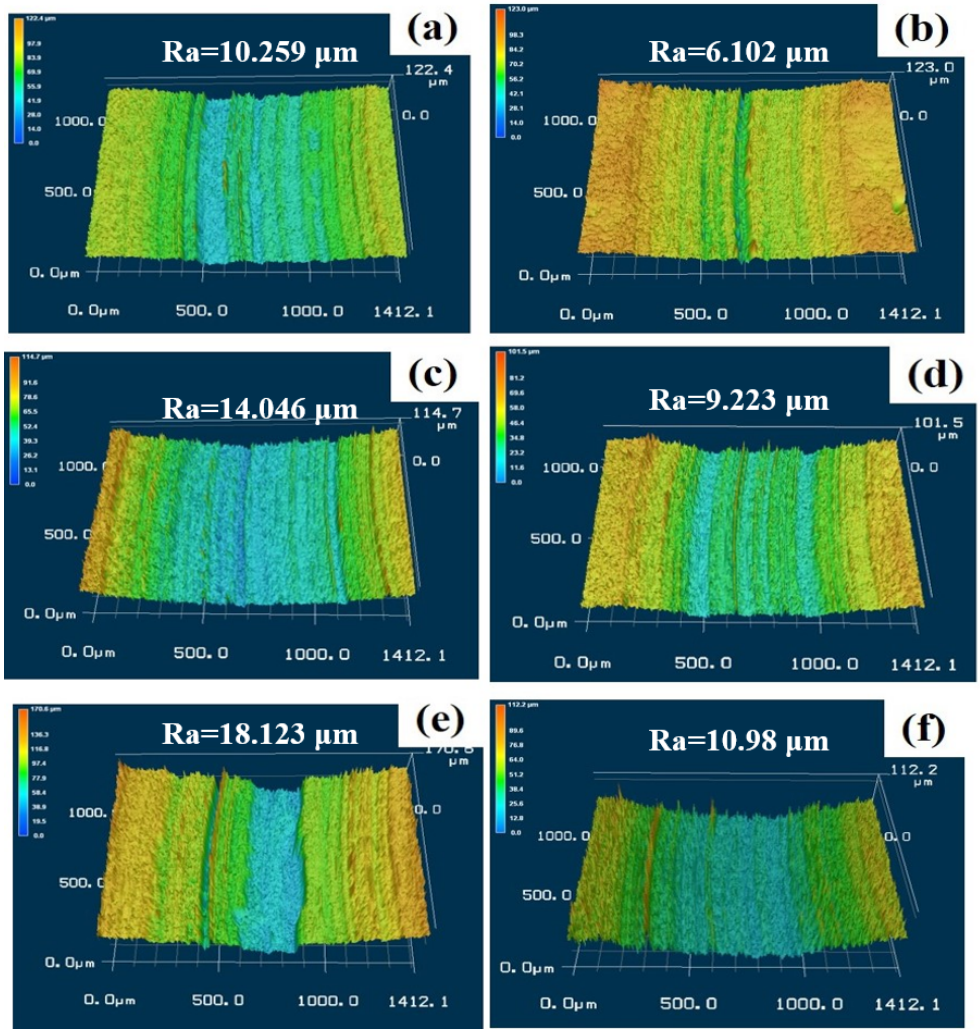

Figure 5.3. The 3D morphologies of the wear surfaces at a sliding speed of 0.1m/s for as-received at a load of: (a) 10N, (c) 30N and (e) 50N, for USSP treated at a load of: (b) 10N, (d) 30N and (f) 50N.

5.3.4 Wear track

Besides the wear rate, the width of the wear track is a commonly used measurement to estimate the wear resistance of a material. The SEM micrograph of the wear tracks of the as-received and the USSP treated AZ31 Mg alloy under the sliding speed of 0.1 m/s are present in figure 5.4. The width of the wear tracks of as-received and USSP treated under a load of 10 N are 1.167 mm and 0.822 mm, respectively, shown in

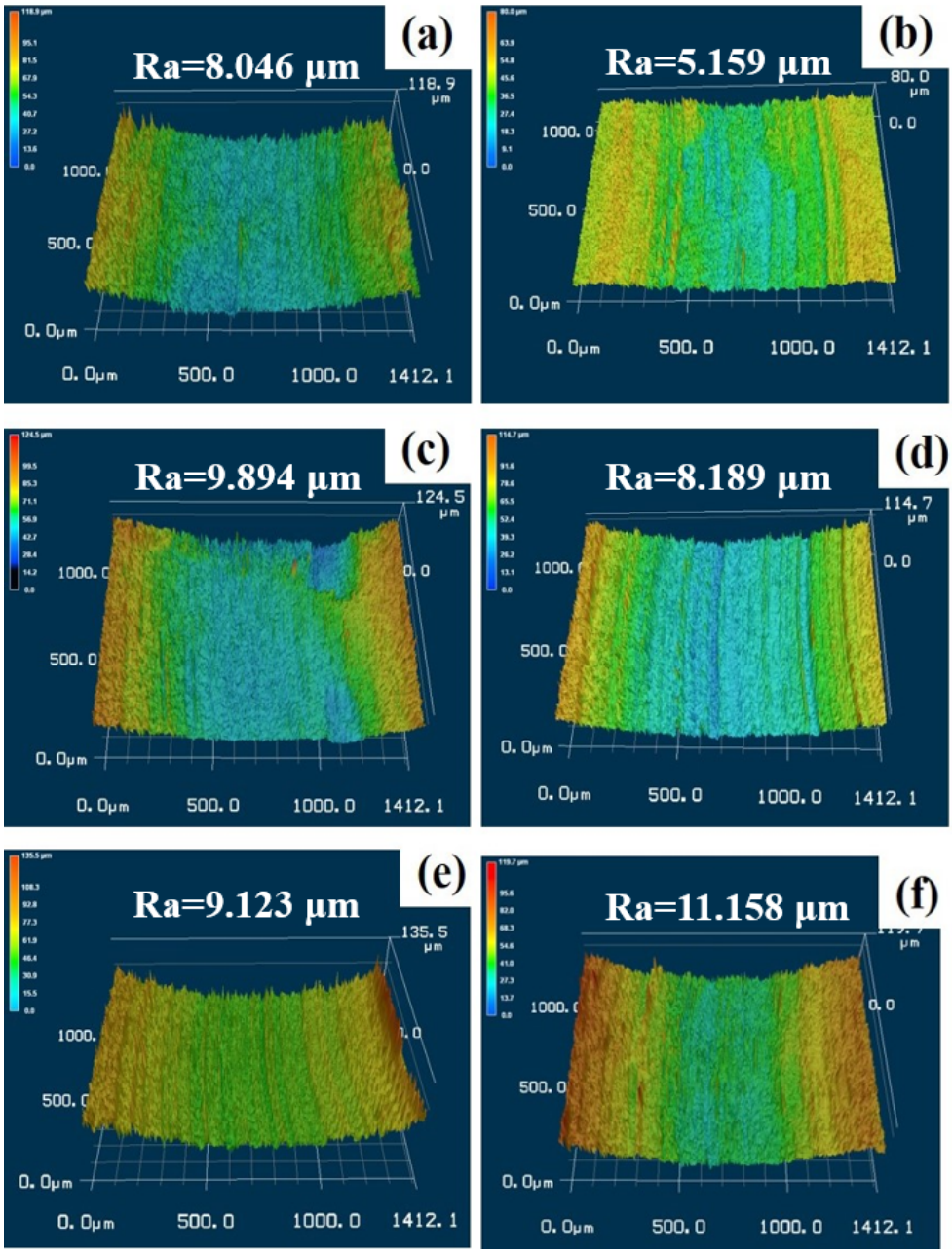

Figure 5.4. The 3D morphologies of the wear surfaces at a sliding speed of 0.5m/s for as-received at a load of: (a) 10N, (c) 30N and (e) 50N, for USSP treated at a load of: (b) 10N, (d) 30N and (f) 50N.

figure 5.4 (a) and (b). By contrast, the widths of the wear tracks under a load of 30 N are 1.38 mm and 1. 187 mm for as-received and USSP treated, respectively, as shown in figure 5.4 (c) and (d). The widths of the wear tracks under a load of 50 N are 1.62 mm and 1.533 mm respectively, seen in figure 5.4 (e) and (f).

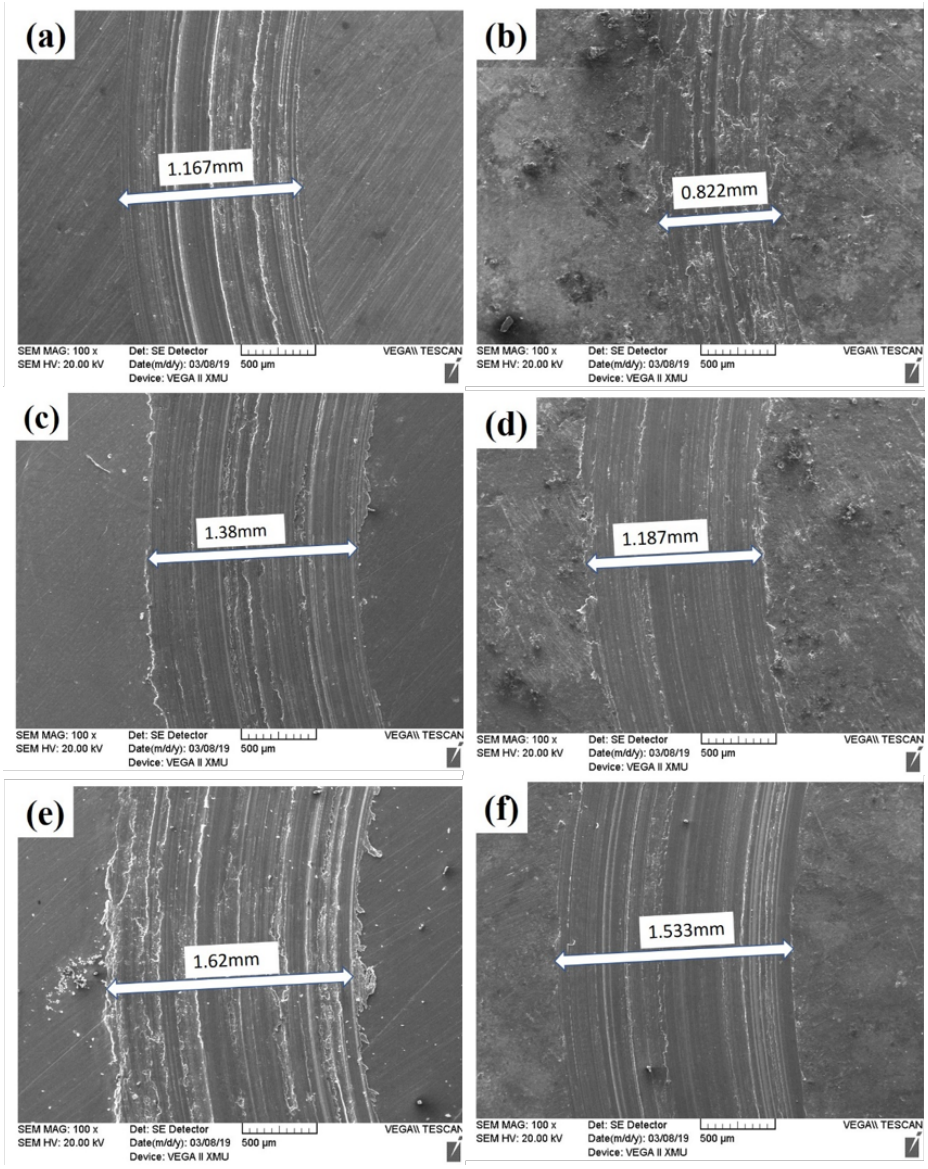

Figure 5.5. SEM micrographs of wear tracks after 100 m of sliding wear test at a sliding speed of 0.1m/s for as-received AZ31Mg alloy under a load of: (a) 10N, (c) 30N and (e) 50N, for USSP treated under a load of: (b) 10N, (d) 30N and (f) 50N.

The wear tracks of as-received and USSP treated under the sliding speed of 0.5 m/s are present in figure 5.5. Under a load of 10 N, the widths of the wear tracks of as-received and USSP treated are 1.212 mm and 1.05 mm, respectively. The widths of the as-received and USSP treated under a load of 30 N is 1.25 mm and 1.145 mm,

respectively. The widths of the wear track increase to 1.583 mm and 1.17 mm for as received and USSP treated when the load is 50 N. These measurements show that the widths of the wear tracks of the USSP treated sample are narrower than that of the as-received under loads from 10-50 N. It is clear that the surface nanocrystallized AZ31 Mg alloy processed by USSP treatment improves the wear resistance.

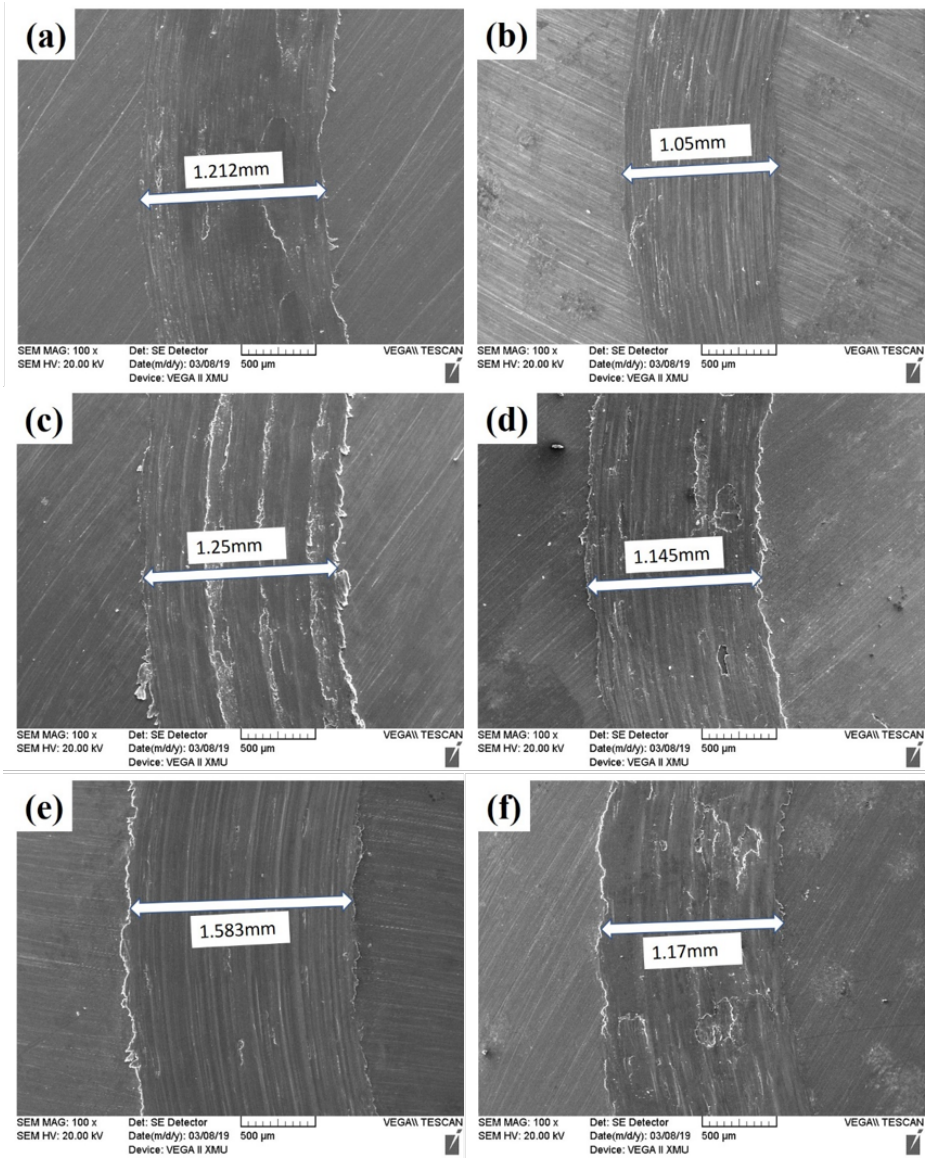

Figure 5.6. SEM micrographs of wear tracks after 100 m of sliding wear test at a sliding speed of 0.5 m/s for as-received AZ31Mg alloy under a load of: (a) 10N, (c) 30N and (e) 50N, for USSP treated under a load of: (b) 10N, (d) 30N and (f) 50N.

5.4 The wear mechanism

The wear surface morphologies of the as-received and USSP treated samples are shown in figure 5.7 under a sliding speed of 0.1 m/s. For as-received AZ31 under a load of 10 N in figure 5.7 (a), there are obvious grooves and ridges parallel to the direction of sliding. Meanwhile, the mapping result of the area highlighted by the red dash line is shown in the right-upper corner. The EDS result shows O element is detected and the at.% is 28.84%. A small amount of Al is also found. So, the wear mechanism for as-received AZ31 at a sliding speed of 0.1 m/s and a load of 10 N is oxidation and abrasion. For the USSP treated sample under the same load in figure 5.7 (b), there is no such obvious grooves or ridges. Instead, a lot of oxide patches appear at the worn surface and the content of O element at the surface is higher than as-received. According to the red highlighted mapping area, the O content can be as high as 42.47%. The result indicates this area is almost fully covered by MgO. Oxidation is the main wear mechanism for USSP treated samples. The nanocrystalline has a high activity to be oxidized during the wear process because the grain boundaries can act as the channel of atomic diffusion (Xia et al., 2016). During the wear process, the frictional heat generated during the sliding motion results in the formation of oxide layer on the worn surface. The formed oxide layer can reduce the true metallic contact, leading to a lower wear rate and COF value. For as-received, the wear surface morphology with the increase of applied load to 30 N is present in figure 5.7 (c). The higher applied load leads to the promotion of detachment of the surface(Taltavull, Torres, Lopez, & Rams, 2013). Besides the oxidation, an obvious delamination is observed, resulting in an increase of the wear rate. The application of higher load (50 N) results in a more detachment of the worn surface and more delamination, leading to a continuous increase in wear rate. For the USSP treated samples, the surface morphology under loads of 30 N and 50 N are present in figure 5.7 (d) and 5.7 (f). Unlike the as-received, there is no delamination found and the abrasive characteristics such as grooves and ridges are present, implying the wear mechanism is abrasion.

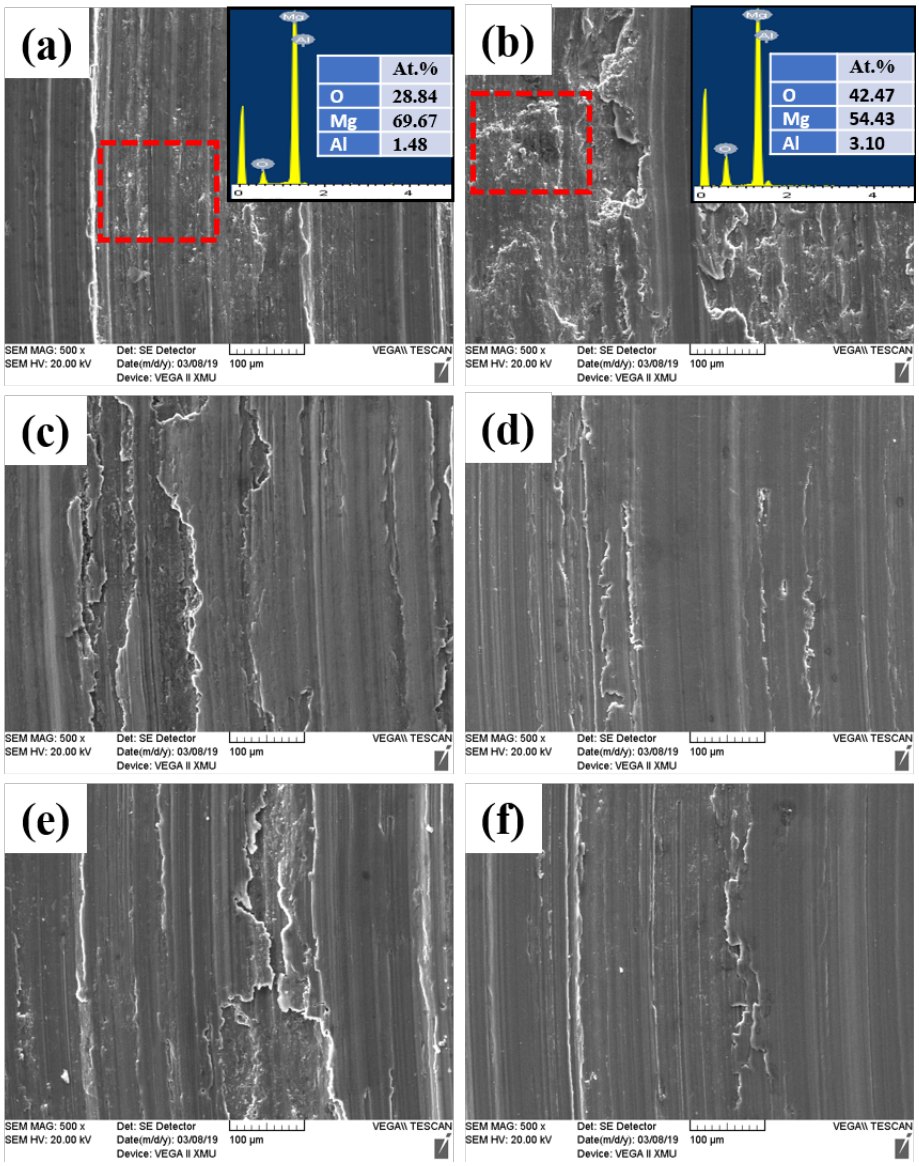

Figure 5.7. SEM micrographs of the worn surface at a sliding speed of 0.1m/s for as-received at a load of: (a) 10N, (c) 30N and (e) 50N, for USSP treated at a load of: (b) 10N, (d) 30N and (f) 50N.

The wear surface morphology of the as-received and USSP treated samples are shown in figure 5.8 under a sliding speed of 0.5 m/s. For as-received under a load of 10 N, the surface becomes smoother than that of as-received under a sliding speed of 0.1 m/s. The increased sliding speed results in the increment of local temperature and detachment

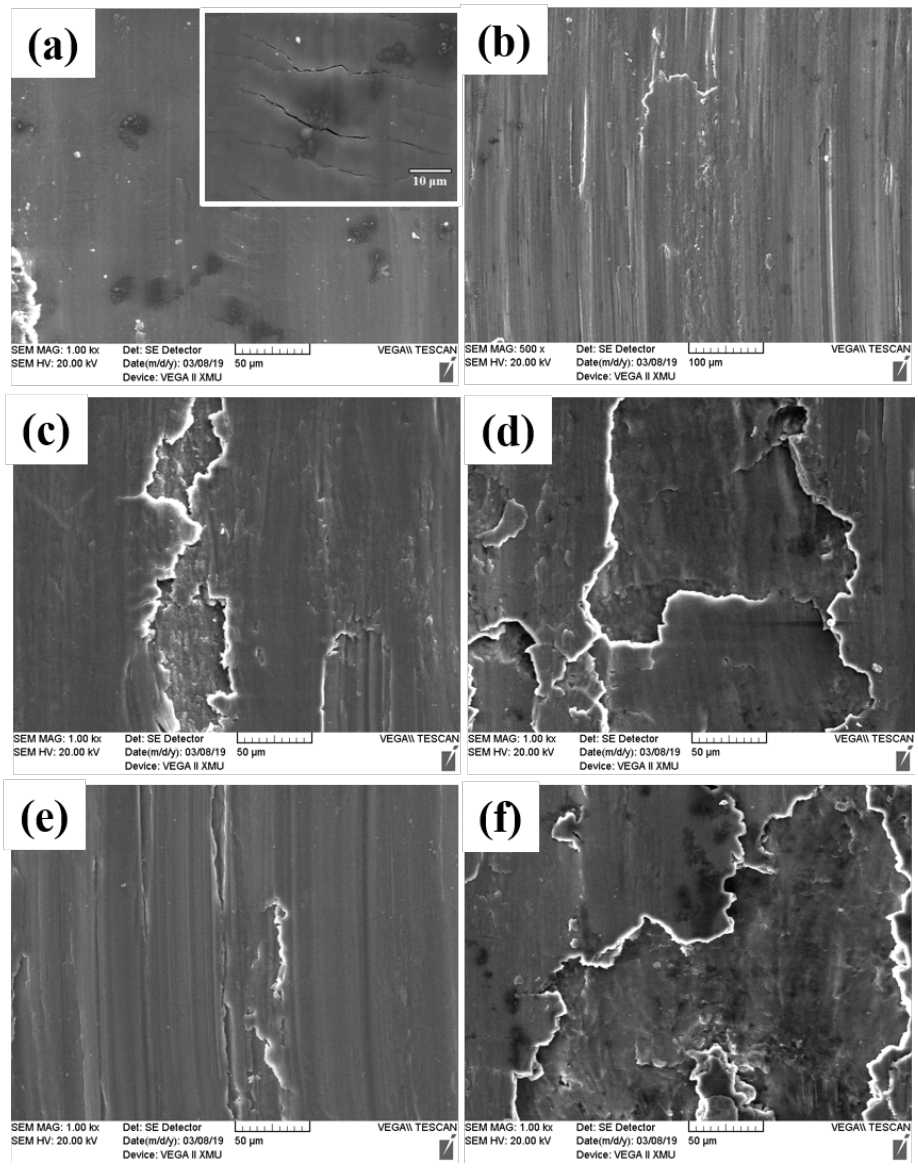

Figure 5.8. SEM micrographs of the worn surface at a sliding speed of 0.5m/s for as-received at a load of: (a) 10N, (c) 30N and (e) 50N, for USSP treated at a load of: (b) 10N, (d) 30N and (f) 50N.

of the surface. Small cracks perpendicular to the sliding direction are found. These cracks will undergo a propagation, linking and subsequent shearing under further sliding, and remove the worn surface in the form of sheet-like laminates(Dey & Pandey, 2018). For the USSP under a load of 10 N, the worn surface is covered by grooves, indicating

abrasion is the main wear mechanism. When the load increases to 30 N, the wear mechanisms for as-received and USSP treated are both delamination. What is interesting is that the wear surface became smooth and featureless when the load increased to 50 N in as-received. This is because the thermal softening and melting happens. When the applied load and sliding velocity reach certain critical thresholds, the sudden increase in temperature at the contacting area may exceed the melting point of the metal, resulting in a thermal softening of the alloy. For the USSP treated sample, delamination is still the main wear mechanism under the load of 50 N.

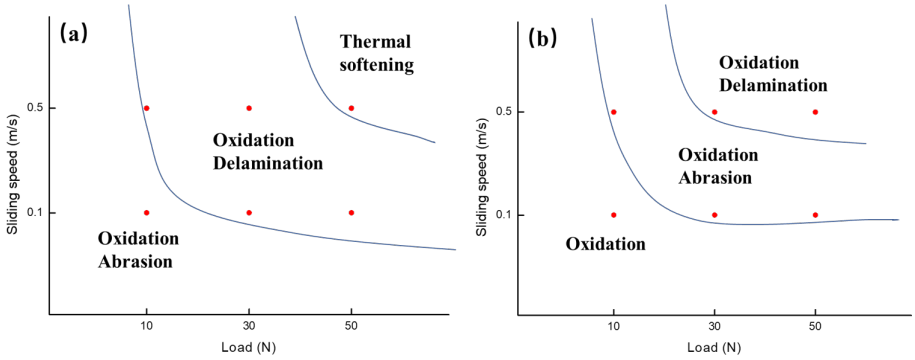

Figure 5.9. Wear transition map for as-received (a) and USSP treated (b) AZ31 Mg alloy.

The wear transition map under different sliding conditions for as-received and USSP treated AZ31 Mg alloy is present in figure 5.9. Lines are used to identify the various wear regimes. For as-received AZ31, abrasion and oxidation happen at low applied loads and low sliding speeds. The transition occurs from abrasion+ oxidation to delamination +oxidation. These two regimes are the mild wear regimes. When the sliding speed reaches 0.5 m/s and the load is 50 N, thermal softening happens and the transition from mild wear to severe wear occurs. For USSP treated AZ31 Mg alloy in figure 5.9(b), under lower sliding speeds and low applied load, oxidation controls the wear behavior. An increase of sliding speed or applied load leads to the regime of abrasion + oxidation. A further increase in sliding speed to applied load leads to the delamination + oxidation regime. No

transition from mild to severe wear is observed in USSP treated samples. The mild wear regimes are the safe operation region for a material. The formed surface nanocrystalline leads to the transition boundary between mild wear and severe wear to a higher sliding speed and a higher load, which widens the safe operation region of AZ31 Mg alloy.

5.5 Summary

In this chapter, an experimental study has been conducted to investigate the tribological behavior of as-received AZ31 Mg alloy after USSP treatment. The wear resistance was measured by a ball on disk wear test at room temperature in the air. The wear behavior was evaluated by the coefficient of friction, the wear rate and the worn surface morphology. The major conclusions from the experimental study are listed as follows:

The wear resistance of AZ31 Mg alloy was improved after USSP treatment. The coefficient of friction and the wear rate of AZ31 Mg alloy became lower after USSP treatment.

The widths of the wear track of the USSP treated sample were much narrower than that of as-received. The worn surface of USSP treated surface had a lower surface roughness.

Under a sliding speed of 0.1 m/s and a load of 10 N, the wear mechanism of the as-received was abrasion + oxidation while USSP treated was oxidation.

The increase of sliding speed or applied load of USSP treated AZ31 Mg alloy led to the abrasion + oxidation and further increase in the sliding speed or applied load resulted in delamination. No severe wear was observed. The formed surface nanocrystalline led to the transition boundary between the mild wear and severe wear to a higher sliding speed and higher applied load.

CHAPTER 6. EXPERIMENTAL STUDY ON CORROSION BEHAVIOR OF ULTRASONIC SHOT PEENING TREATED AZ31B MAGNESIUM ALLOY

6.1 Introduction

This chapter presents the experimental study of the effect of ultrasonic treatment on the corrosion resistance of AZ31 Mg alloy sheet in 3.5wt.% NaCl solution. The corrosion resistance of AZ31 Mg alloy sheet is tested by electrochemical test, hydrogen evolution test and weight loss test. The corrosion morphology after immersion is observed as well. In addition, the corrosion resistance of ultrasonic treated sample along the depth is analyzed. The corrosion resistance of this gradient nano structure is analyzed. The relationship between the corrosion resistance and the microstructure along the depth is built.

The results show the corrosion resistance of AZ31 Mg alloy is changed after ultrasonic shot peening and the corrosion resistance along the depth is different. An obvious reduction of corrosion resistance after ultrasonic shot peening treatment is observed. The reduced corrosion resistance is due to the exfoliation of Fe from the shot during the ultrasonic shot peening treatment. So the corrosion resistance of the 20μm depth layer is also much higher than the untreated because the exfoliated Fe particle can exist at a depth of more than 20 μm. For the 40 μm depth layer, its corrosion resistance is obviously improved, compared with the untreated. The improved corrosion resistance is attributed to the great grain refinement. The grain boundary acts as the barrier for the prolongation of corrosion between grains. For the 80μm and 100 μm depth layers, the corrosion resistance is slightly decreased but still better than the untreated. So the gradient nano structure leads to different corrosion behaviors along the depth. After USSP treatment, not also a gradient nano structure is obtained, but also a diverse corrosion resistance along the depth.

6.2 Corrosion behavior of the ultrasonic shot peening AZ31 Mg alloy sheet

To investigate the corrosion behavior of the ultrasonic shot peening treated AZ31 Mg alloys sheet, the samples were tested by the electrochemical measurements in 3.5% NaCl solutions. The tested samples were cut from the center of the ultrasonic shot peening area, with a square sharp of 10 mm $\times$10mm. The machined specimens were immersed in 3.5 weight percent (wt.) sodium chloride (NaCl) solution and the corrosion tests were conducted at room temperature (20 °C).

The corrosion resistance of the USSP treated and untreated samples is test by electrochemistry test. The electrochemistry test was conducted using a VersaSTAT 3 potentiostat/galvanostat connected to a three-electrode cell. The polarization curve is applied to obtain the E_{corr} and I_{corr} to estimate the corrosion resistance. The electrochemical impedance spectroscopy (EIS) measurements were conducted,and the sample was immersed for 30 min to obtain a steady state before test.

The polarization curves of the sample before and after the USSP treatment for 10 min are present in figure 6.1(a). Table 6.1 presents the extracted values from the data fitting of the potantiodynamic polarization curves. For the as-received AZ31 alloy, a typical potentiodynamic polarization curve of as-roll AZ31 Mg alloy is present. The E_{corr} of as-received AZ31 is -1.44 V and the I_{corr} is 5.15 mA cm^{-2}. The potentiodynamic polarization curve of the USSP treated sample shows a totally different changing behavior. The corrosion potential for the USSP treated sample is more positive than the as-received. The cathodic polarization current densities of the USSP treated is higher than that of the as-received. Additionally, in the anodic region, the breakdown behavior of the protective layer is not shown. The breakdown potential (E_b) has shifted from the anodic region in the as-received to the cathodic region in the USSP treated, which is indicated by the red arrows. This results in a great increase of the anodic current densities because of the breakdown of the protective layer. As a result, the E_{corr} of USSP treated AZ31 shifts to a noble value of -1.15v and the I_{corr} increases to 325.8 mA cm^{-2}, which is about 60 times of the as-received AZ31. Figure 6.1(b) shows the Nyquist plots of the AZ31 Mg alloy before and after USSP treatment. The as-received AZ31 has a very clear capacitive arc at

the high frequency region. Generally, the diameter of the capacitive loop is related to the resistance of the charge-transfer process, which means a larger diameter of the arc indicates a better corrosion resistance of Mg alloys (Müller et al., 2007). For the USSP treated sample, the diameter of the arc is much smaller than that of the as-received, and is agreed with the potentiodynamic polarization curves. Thus, it can be easily concluded that the corrosion resistance of AZ31 Mg alloy decreases greatly after USSP treatment.

The SEM of the USSP treated top surface is present in figure 6.2. The top surface after 10 min USSP treatment becomes rough, which is consist with the 3-D laser microscope. Meanwhile, there are some bright dots distributed at the surface, and these dots are the magnesium oxide. Besides the bright dots, it is found there are some smaller gray dots at the surface, which is highlighted by the red dash line. The Energy Dispersive X-ray (EDX) results of point B and C are present in figure 6.2(b) and (c). From the EDX results, these gray dots are Fe particles. During the USSP treating process, Fe particle will exfoliate because of the impact and friction between the stainless-steel shots(Q. Sun, Han, Liu, Xu, & Li, 2017). The exfoliated Fe particles will attach at the top surface and some of the Fe particles will be impressed into the matrix by the impact of the shots. This left Fe particle on the surface will reduce the corrosion resistance greatly because the electrode potential of Fe is much more positive than Mg matrix and a severe galvanic corrosion between the Fe particle and Mg matrix happens(Makar & Kruger, 1993).

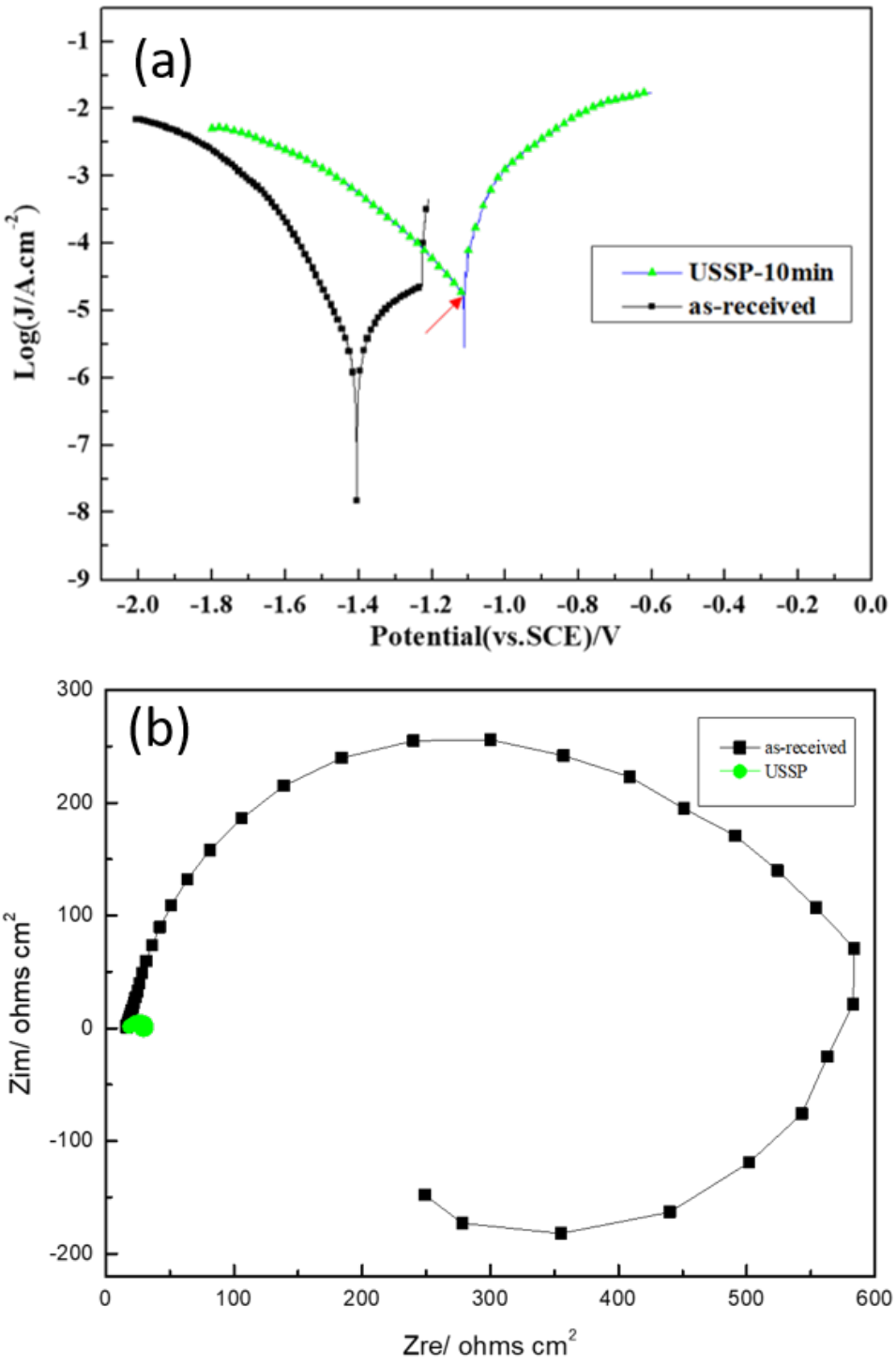

Figure 6.1. (a) potentiodynamic polarization curves and (b) Nyquist plots of AZ31 Mg alloy sheet before and after 10 min USSP treatment

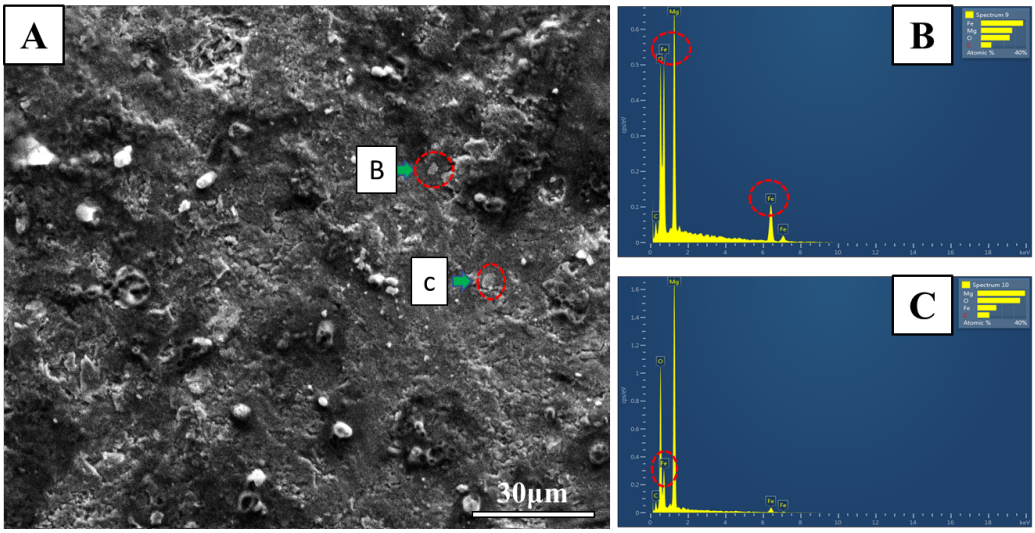

Figure 6.2. The SEM pictures of the top surface after USSP treatment (a) and the EDX results of point B (b) and point C (c)

6.3 Corrosion performance of ultrasonic shot peening under different depths from the top surface

As is mentioned above, there would be a exfoliation of Fe particles from the stainless steel shot during USSP process. This small Fe particles will attach on the top surface of the USSP treated sample. During the immersed process in 3.5 wt. % NaCl solution, there will be a galvanic corrosion happened between Fe particle and Mg matrix because the electrochemical potential of Fe is much positive than Mg matrix. So the induced Fe containment during USSP process will affect and reduce the corrosion resistance of the nanocrystalline on the top surface. The effect of grain refinement on the corrosion resistance cannot be observed and analyzed because of the serious disturbance of Fe containment. In order to analyze the effect of this nanocrystalline structure on the corrosion resistance of Mg alloys, the USSP treated samples are polished by 20 μm, 40 μm, 80 μm and 100 μm along the depth.

6.3.1 Experimental setup

The corrosion behaviors of layers with different depths from the top surface to the center were investigated. The sample was polished carefully from the top surface to the center by hand at 4000 grit SiC paper. The thickness of the specimen before and after polish are measured by micrometer to ensure the polished thickness. The polished thicknesses were 20 μm, 40 μm, 80 μm and 100 μm, respectively, seen in figure 6.3

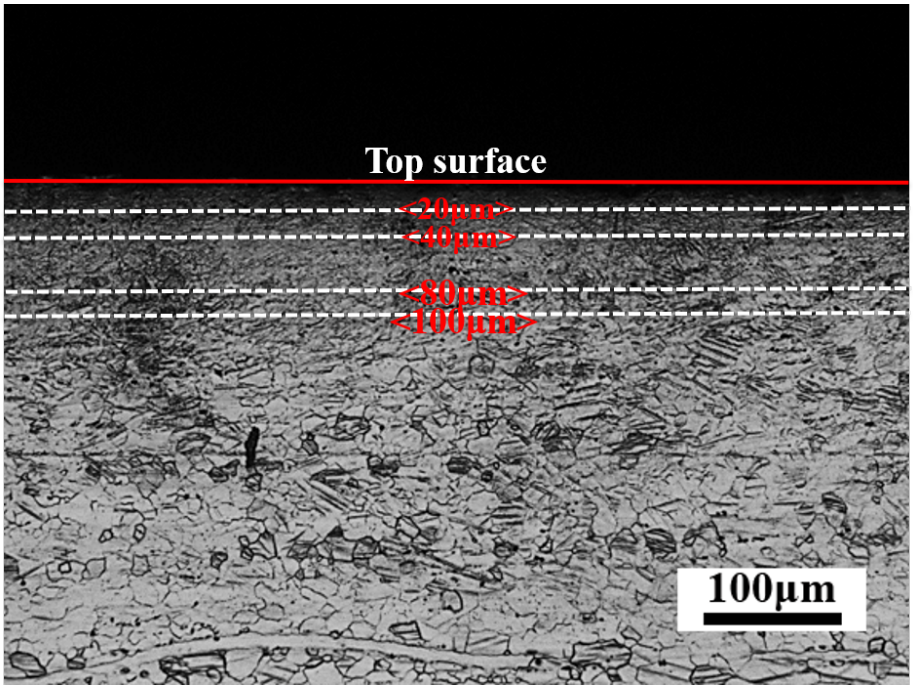

Figure 6.3. The specific position of the layers after polishing thicknesses of 20 μm, 40 μm, 80 μm and 100 μm.

A comprehensive study was conducted to evaluate the corrosion behavior of the USSP treated AZ31 Mg alloy under different depth from the top surface: (a) immersion test, (b) hydrogen evolution test, (c) electrochemical measurements, and (d) weight loss test. An untreated AZ31 Mg alloy sheet was tested as a reference for comparison. All the tests were conducted at 3.5 wt. % NaCl solution.

For hydrogen evolution test, the untreated, the USSP treated and the USSP polished specimens were cover with resin epoxy and only the treated or polished surface were explored to the solution. The exposed time was 175 hours.

For the weight loss test, the untreated, the USSP treated and the USSP polished were immersed in the solution for 7 days. After the immersion, the corrosion products were clean by the in an ultrasonic holder. The weights of the specimens before and after immersion were measured.

For the electrochemical test, the test was conducted using a VersaSTAT 3 potentiostat/galvanostat connected to a three-electrode cell. Open circuit potential vs. time curves was measured for the as-received, ultrasonic shot peening treated sample and polished sample. The electrochemical impedance spectroscopy (EIS) measurements and polarization curves were also conducted.

In the immersion test, the corrosion morphology of the untreated, the USSP treated and the USSP polished specimens was observed after immersion in the 3.5 wt. % NaCl solution for 7 days. After immersion, the corrosion products were removed by the in an ultrasonic holder. The specimens were cleaned by ethanol and air dried under a hot blower. The morphology of the cleaned specimen was observed by SEM.

6.3.2 Electrochemical Test

The variations in the open circuit potential with immersion time for layers of different depths are present in figure 6.4, and the E_{OCP} values after 1200 seconds immersion are list in table 6.1. For the as-received AZ31 Mg alloys sheet, the E_{OCP} shows a gradient shift towards the positive value during immersion. The positive changing tendency of the E_{OCP} is due to the formation of $Mg(OH)_2$ during the immersion process. The protection from the formed $Mg(OH)_2$ and the dissolution of Mg matrix will come to an equilibrium in the further immersion and reach a steady state (Thomas, Medhekar, Frankel, & Birbilis, 2015). For the USSP 10min treated sample, it displays a curve of different changing tendency. The E_{OCP} is more positive than that of as received. This may be due to the left Fe particles which are more noble than the Mg matrix. After the

immersion, the E_{OCP} is drifted to a negative value a bit at the beginning and becomes stable quickly. The shift towards a negative value of E_{OCP} value is not normal. The happening of this shift was due to the increased dissolution speed of Mg into the solution. Usually, this kind of negative shift happened at the very beginning of the immersion because of the limited formation of $Mg(OH)_2$, and would become positive in the further immersion (Singh, Singh, & Das, 2015). Here, the curve stays stable and no such kind of positive shift is observed, indicating there is no effective films formed on the surface to protect the Mg matrix. For the polished USSP-10min-20μm sample, the changing tendency is similar to that of USSP-10min sample. It shows a slight increase at the beginning and then decreases, just as that of the USSP-10min sample. The result indicates the formation of protective layer happens at the surface of the USSP-10min sample, but this protective layer is not functional because of the left Fe particle and the galvanic corrosion between Mg matrix. For the polished USSP-10min-40μm sample, its curve is neither similar to as-received nor the USSP-10min sample. Its value is between as-received and USSP-10min samples. The curve is drifted towards more positive values and becomes stable much more quickly. The E_{OCP} of the polished USSP-10min-80μm sample is slightly negative than the 40μm sample, and it presents an increased tendency like as-received, but in a quicker speed. The curve of the polished USSP-10min-100μm sample is similar to as-received. So the protective layers successfully formed at the polished 40 μm, 80 μm and 100 μm samples.

In figure 6.5, the potentiodynamic polarization curves of the layers of different depths are present, and the values extracted from the data fitting are list in table 6.1. The curves display obvious variations along the different depths. The E_{corr} value of as-received is -1.44 V. The E_{corr} value shifts towards to -1.15 V of the 10 min USSP treated sample. After polishing of 20 μm, the E_{corr} value shifts towards negative to -1.28 V. Further polishing to 40 μm leads to the further shift of E_{corr} value to -1.41 V. The E_{corr} values of 80 μm and 100 μm are -1.35 V and -1.37 V, respectively. The breakdown potential, E_{bd}, is obvious found in as-received and polishing 40-100 μm samples in the anodic region while missed in USSP and polishing 20 μm samples. The curve of the polishing 20 μm sample is similar to that of the USSP treated sample. The cathodic polarization current

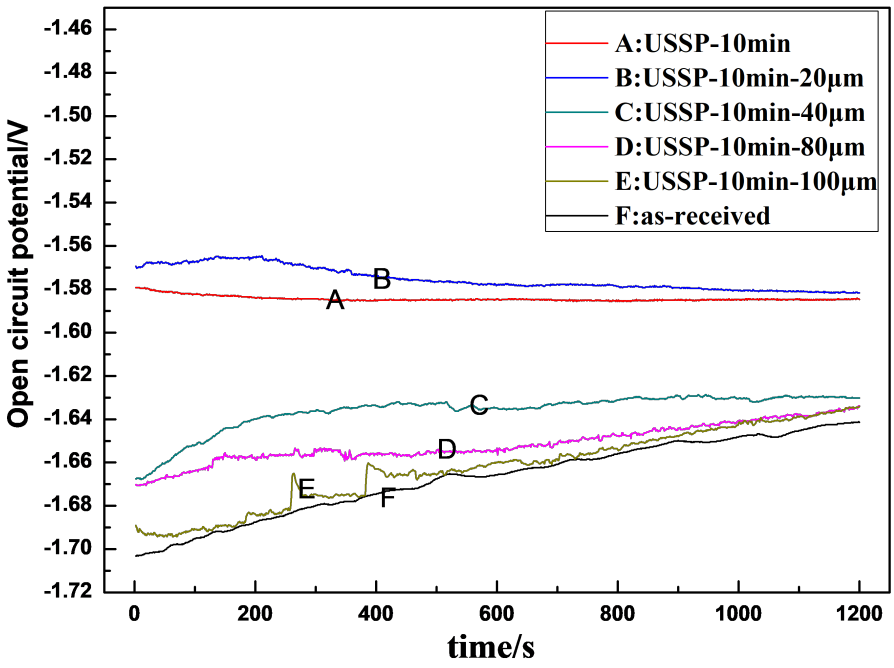

Figure 6.4. The open-circuit potential, as a function of immersion time for various depth layers of the USSP treated samples

densities of the polishing 20 μm samples is higher than that of the as-received, and the E_b also is shifted from the anodic region in the as-received to the cathodic region. As a result, the E_{corr} of the polishing 20 μm sample still stays at a noble value and the I_{corr} is still as high as 138.5 mA cm^{-2}, which is about 27 times of the as-received. The created roughness of the top surface during the USSP process forms some valleys. If the Fe particles were located the bottom of the valleys, a polishing deeper than the valley is required to remove all the Fe particles. According to the 3-D dimension information from chapter 4, the R_v of the USSP treated sample is 35.5 μm. So polishing 20 μm is still not

enough to remove all the Fe containments. For the polishing 40-100 μm samples, the cathodic region is similar to that of the as-received AZ31 while the current density of the anodic region is smaller than that of the as-received. The decreased current density of the anodic region also leads to a shift of E_{corr} towards a noble value but a smaller I_{corr}.

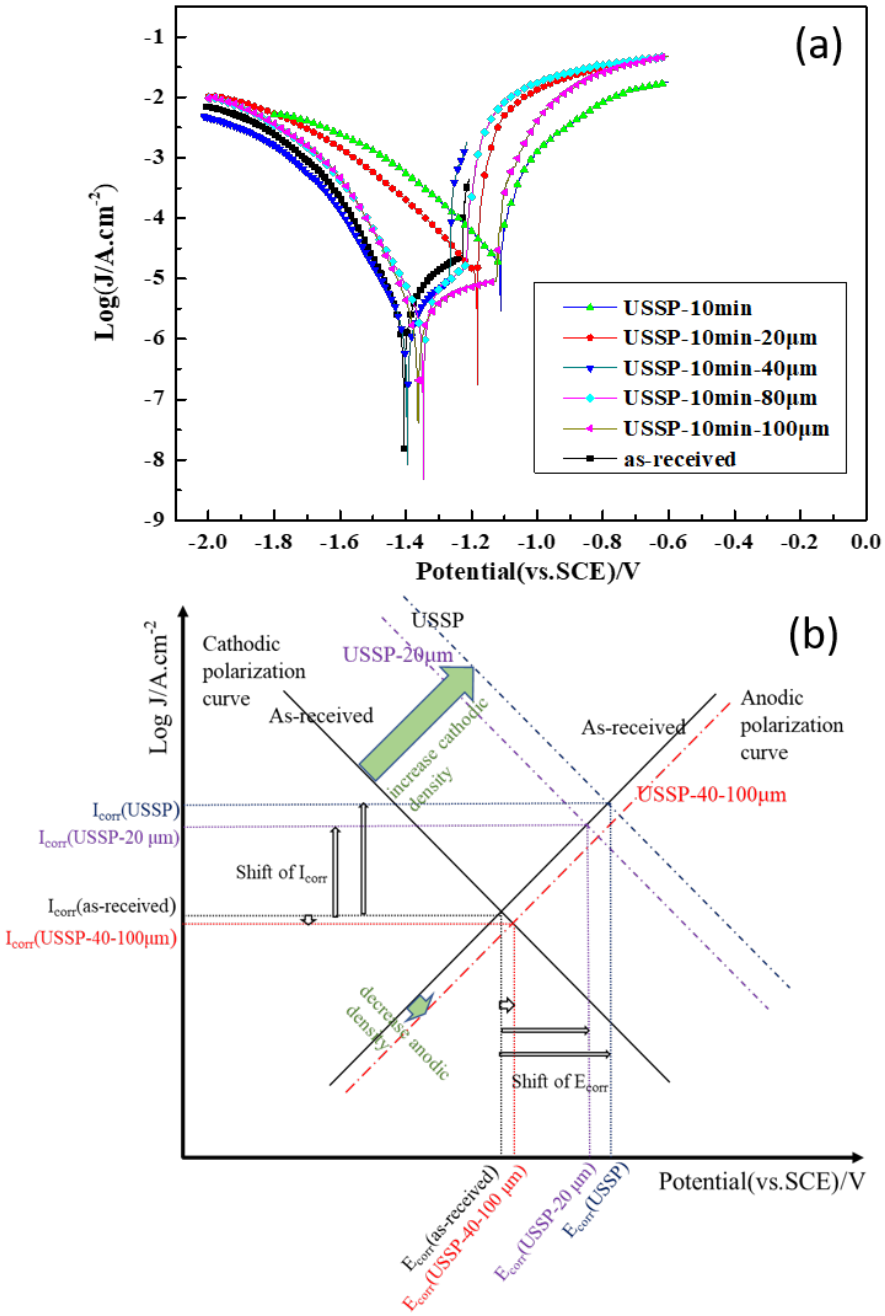

Figure 6.5. Potentiodynamic polarization curves of as-received AZ31 Mg alloy sheet, USSP treated and polished layers of different depths in 3.5 wt.% NaCl solution(a) and schematic drawing explaining the shifts of E_{corr} and I_{corr} after USSP treatment and different depth polishing(b)

The variations of the current densities of the layers along the depth are schematically explained and present in figure 6.5(b). The cathodic branch curve represents the hydrogen evolution and the anodic branch curve represents the dissolution of Mg (G. Song, Atrens, St John, Wu, & Nairn, 1997). In this study, the USSP treated AZ31 Mg alloy sheet endows a surface with not only nanocrystalline but also exfoliated Fe particles. It is reported the grain refinement of Mg alloys may lead to a dissolution of impurities or second phases in the grain boundaries, and results in less cathodic sites in the alloy for cathodic reaction and improves the corrosion resistance of Mg alloys(Laleh & Kargar, 2011). In this study, the current density of the cathodic branch does not decrease but increases a lot after USSP treatment. The left Fe particle in the top surface ruins the corrosion resistance of Mg alloy because of the severe galvanic corrosion between Mg matrix and Fe particles. The Fe particles lead to more cathodic sites for the cathodic reaction. The 20 μm polishing removes a part of the Fe particles and results a slight decrease of the cathodic reaction but the high sensitivity of the corrosion resistance of Mg alloys to Fe particle still leads to a high corrosion rate of the 20 μm polished sample. For the polished 40-100 μm samples, the polishing process removes all the Fe particles from the USSP process. The cathodic branch curves the polishing 40-100 μm samples are almost the same as that of the as-received. The limited amount of second phases in as-rolled Mg AZ31 sheet leads to an unobvious dissolution of impurities or second phases at the grain boundaries. The limited dissolution of second phases results in a similar cathodic reaction among them. However, the current density of the anodic region is reduced. The anodic process represents the dissolution of Mg alloys. The reduced current density leads to a lower I_{corr} and improved corrosion resistance. The dissolution of Mg is affected by many factors, such as the texture (Xin, Li, Li, & Liu, 2011), the residual stress (Denkena & Lucas, 2007) and the formed protective films (Esmaily et al., 2017) on the surface. The different textures lead to different in-plane packing densities of the surface. A greater chemical-bonding strength of atoms results a higher difficulty to corrode the atoms away when exposed to the solution (M. Liu, Qiu, Zhao, Song, & Atrens, 2008). In Mg alloys, the basal plane presents a higher in-plane packing density and a better corrosion resistance than other planes. Here, for the as-received AZ31 Mg alloy sheet, a strong basal

texture has formed after rolling process. Moreover, the intensity of the basal texture would be reduced somehow after USSP. So the texture is not the reason of the improved corrosion resistance of polished 40-100 μm samples. On the other hand, the tension stress on the surface will leads to a higher anodic current density while the compression stress on the surface will leads to a lower anodic current density (Horner, Connolly, Zhou, Crocker, & Turnbull, 2011). In this study, the existed compression stresses on the polishing 40-100 μm samples lead to a low anodic current density and better corrosion resistance. Last but not the least is the formed protective layers on the surfaces. From the OCP result, it is clearly found that the polishing 40-100 μm samples have more positive values and a faster speed to become stable after immersion, indicating the formation speeds of the protective layer of the polished 40-100 μm samples are higher than that of as-received.

Table 6.1. Parameters evaluated from the OCP curves and the polarization curves for the layers of different depths in 3.5 wt.% NaCl solution

sample condition	E_{corr}.(vs.SCE)/V	I_{corr}/(μA cm^{-2})	OCP/V
As-received	-1.44	5.15	-1.642
USSP-10min	-1.15	325.8	-1.585
USSP-10min-20μm	-1.28	158.49	-1.581
USSP-10min-40μm	-1.406	2.09	-1.631
USSP-10min-80μm	-1.37	4.26	-1.635
USSP-10min-100μm	-1.35	4.16	-1.635

Figure 6.6 presents the Nyquist plots of as-received AZ31 Mg alloy sheet, USSP treated and polished of different depths in 3.5 wt.% NaCl solution. A clear capacitive arc at high frequency region is shown in all the spectra. The diameter of the capacitive loop of USSP treates sample is much smaller than that of the as-received. The diameter of the capacitive loops after a 20 μm polishing are smaller than that of the as-received sample while the diameters of the capacitive loops under 40 μm, 80 μm and 100 μm polishing are larger than that of the as-received sample. This agrees well with the result of potentiodynamic polarization curves in figure 6.5.

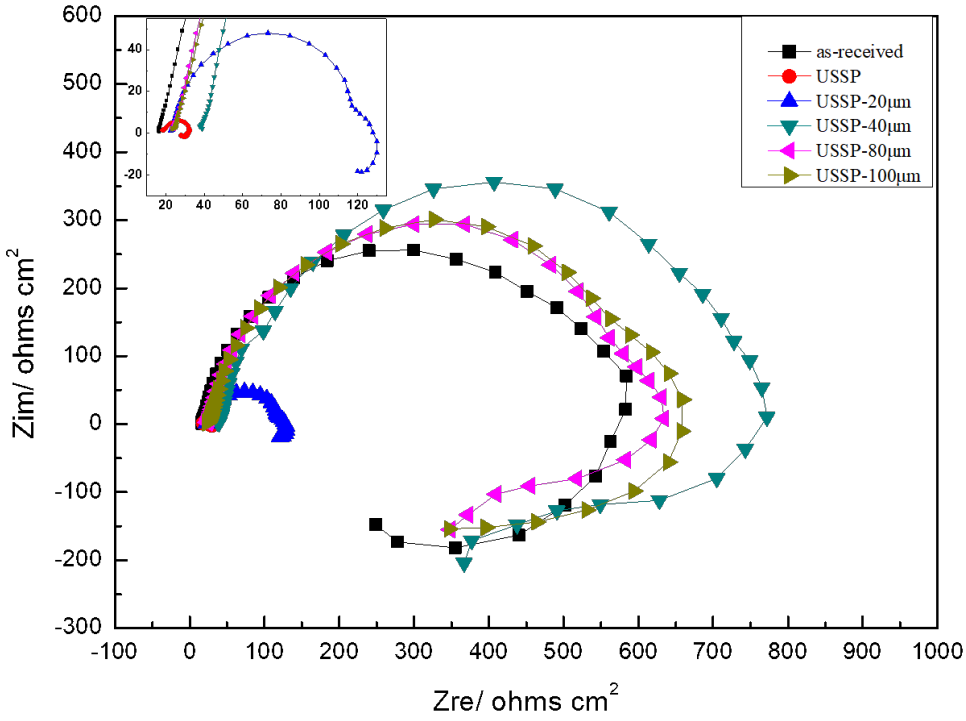

Figure 6.6. The Nyquist plots of as-received AZ31 Mg alloy sheet, USSP treated and polished layers of different depths in 3.5 wt.% NaCl solution

6.3.3 Hydrogen Evolution Test

The hydrogen evolution test was used to measure the corrosion behavior of the as-received, USSP treated and polished samples. As we can see from Figure 6.7, there are an obvious difference between the as-received, USSP treated and USSP polished samples in the amount of hydrogen evaluated. For as-received AZ31 Mg sheet, the amount of hydrogen is increasing steadily from the beginning to 175 hours. So the corrosion rate of the as-received AZ31 Mg alloy sheet does not change much during the immersed process in 3.5 wt. % NaCl solution. For the USSP treated sample, the amount of the formed hrdrogen is much lager than that of as-received. The amount of formed hydrogen per area after 27 hours is about 22.15 ml/cm^{-2} while that of as-received one is just 2.97 ml/cm^{-2}. The corrosion resistance of AZ31 Mg alloy sheet is reduced greatly after USSP treatment because the top surface of USSP treated sample is contaminated by the exfoliated Fe particles. The corrosion performance of the polished samples is changed a lot. For the 20 μm polished sample, the hydrogen per area is clearly reduced, compared with the USSP treated sample. The formed hydrogen after 175 hours immersion is 10.5 ml/cm^{-2} . The reduced corrosion rate of the 20 μm polished sample, compared to USSP treated one, is due to the partial remove of the attached Fe containment on the top surface.

For the 40 μm polished sampled, the formed hydrogen is much less than the USSP treated sample and 20 μm polished sample. After 175 hours immersion, the formed hydrogen is just 1.37 ml/cm^{-2}. So the corrosion resistance of 40 μm polished sample is much better than the USSP treated sample. Moreover, the formed hydrogen of 40 μm polished sample is less than that of the as-received sample. The result implies that the attached Fe containment on the top surface is completely removed after 40 μm polishing because the corrosion resistance of Mg alloy is very sensitive to Fe. The greatly reduced corrosion rate means the 40 μm polished surface is a Fe-free surface. Moreover, the corrosion rate of 40 μm polished sample is lower than that of the as-received sample, which implies that the grain refinement and formed nanocrystalline during the USSP process can reduce the corrosion rate of Mg alloys sheet. For 80 μm polished sample, the formed hydrogen amount after 175 hour is 2.6 ml/cm^{-2}, which is larger than that of 40

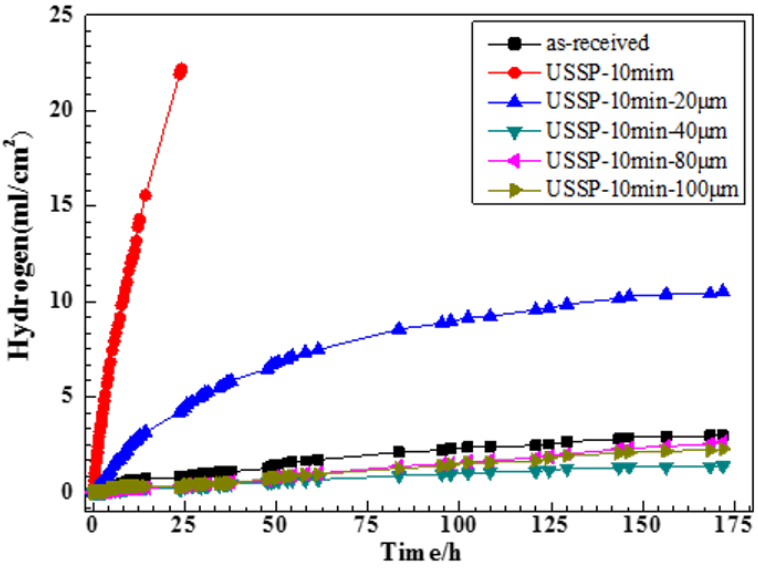

Figure 6.7. The hydrogen evolution per area of AZ31 Mg sheet after USSP and polished in 3.5 wt. % NaCl solution

μm polished but still smaller than that of as-received. According to the EBSD result, the formed gradient nano structure is about 80 μm after 10 min treatment. The 80 μm polished sample is closed to the interface between the nanocrystalline and the deformed matrix. At 80 μm deep area, the grain size is bigger than that of 40 μm depth area. The improved corrosion resistance by the grain refinement of 80 μm polished sample becomes less compared with that of 40 μm polished sample. Anyway, the grain size is still smaller than that of the as-received sample. That is why the corrosion rate of 80 μm polished sample is larger than 40 μm polished sample but smaller than as-received sample. For 100 μm, the formed hydrogen is 2.25 ml/cm^{-2}, after 175 hours immersion. The formed hydrogen of 100 μm polished sample is closed to that of 80 μm polished sample, implying that their corrosion rates are quite similar.

The formed hydrogen per area is converted to the corrosion rate by the experimental equation:

$$P_H = 2.279\Delta V/(st) \tag{6.1}$$

where ΔV is the volume of the evolved hydrogen (ml), s is the explored surface area (cm^2) and t is the time (d). The results are in figure 6.8.

As we see from figure 6.8, all the corrosion rates present a similar tendency during the immersion process: (1) An increased corrosion rate at the beginning process; (2) A gradually decreased corrosion rate after the peak; (3) A steady corrosion rate at longer immersion time. In the first stage of corrosion initiation, the increased corrosion rate is caused by the micro-galvanic corrosion. The corrosion prolongated and then be restricted by the grain boundary or second phase. That is why the corrosion rate reaches its peak and begins to decrease. During the following stage, the second phase may be consumed by the separation with the matrix because of the formed $Mg(OH)_2$ between them even though the second phase with a higher electrochemical potential will not be corroded once it is connected to the matrix. In the whole process, a layer of $Mg(OH)_2$ is formed which can protect the matrix and the thickness of $Mg(OH)_2$ increases as the time prolongated. Lastly, an equilibrium between the protection of $Mg(OH)_2$ and corrosion of Mg matrix is reached, and a steady corrosion rate is formed.

For the as-received AZ31, the corrosion rate is relatively low. At the beginning, its corrosion rate reaches to 3.5 mm y^{-1}, then begins to decrease and becomes stable after 175 hours immersion. In the USSP 10min treated sample, the corrosion rate at the beginning keeps at a high value of 90-100 mm y^{-1}, much higher than the that of as-received AZ31 Mg alloy sheet. Then the corrosion rate falls gradually, and ends at 50 mm y^{-1}, but still much higher than that of as-received. No such an increased corrosion rate process is observed in USSP treated sample, which means the micro-galvanic corrosion happens immediately once the sample is immersed in the solution, and the formed protective layer is insufficient to protect the matrix. For 20 μm polished sample, the corrosion rate increases gradually to a peak of 13.3 mm y^{-1} after 4 hours immersion. Then it decreases at a slower speed than the increasing rate and reaches to 3.3 mm y^{-1} after 175 hours immersion. For 40 μm polished sample, it presents a lower corrosion rate

than that of the as-received. At the corrosion initiation stage, it reaches its corrosion rate peak of 1.17 mm y^{-1} more quickly, after 8 hours. Then it also begins to fall and keep at a steady corrosion rate of $\sim$ 0.5 mm y^{-1} after 14 hours immersion. The corrosion rate of 40 μm polished sample is about 50 % of as-received. For 80 and 100 μm polished samples, the changing tendency is similar to 40 μm polished sample. The corrosion rate is a bit higher, but still smaller than that of as-received. After 175 hours immersion, the P_H values of 80 and 100 μm polished samples are 0.83 mm $y^{-1}$and 0.72 mm y^{-1}, respectively.

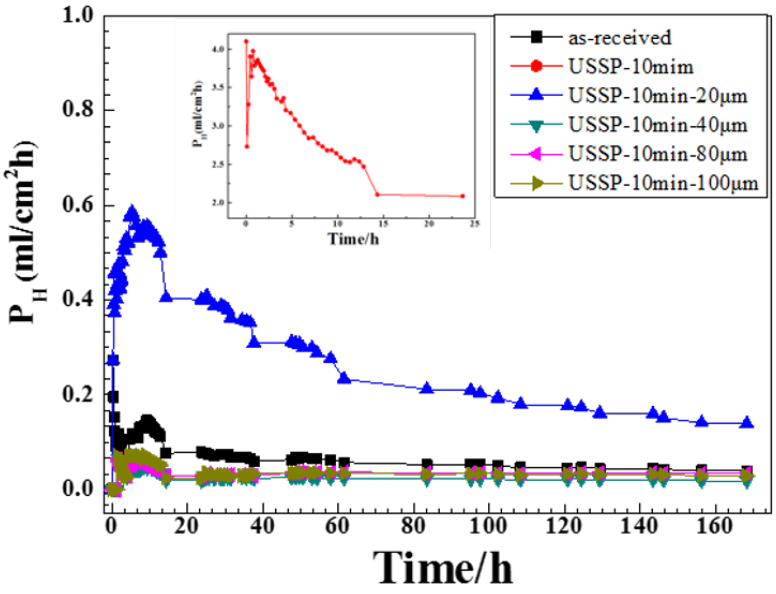

Figure 6.8. The hydrogen converted corrosion rate of AZ31 Mg sheet after USSP and polished in 3.5 wt. % NaCl solution

6.3.4 Mass Loss

The corrosion rates derived from the mass loss for the as-received AZ31 Mg alloy sheet, the USSP treated and polished samples after immersed in 3.5 wt.% NaCl solution for 7 days are listed in table 2. The corrosion rates of these sample with different states decrease in the following order: USSP-10min > USSP-10min-20μm > as-received >

USSP-10min-100μm > USSP-10min-80μm > USSP-10min-40μm. The USSP-10min-40μm sample presents a lowest corrosion rate. The P_w value of the USSP-10min is not calculated because the sample has been corroded completely after 7 days. This ranking of corrosion rate is consistent with that from electrochemical tests and hydrogen evolution test. Nonetheless, there are still some slight difference between the values of corrosion rates. The P_i values are much smaller than P_H and P_w values, and P_w has the maximum values among them, for all the samples. The possible reason is the P_i values are estimated from the polarization curves after 30 min immersion. At the beginning of 30 min, the corrosion rate is still increasing. For the corrosion rate evaluated from mass loss P_w, it is slightly higher than P_H, which may be caused by the additional damage of the mass during the corrosion product cleaning process.

Table 6.2. The comparison between the corrosion rate of P_i (estimated from Icorr from polarization curves), P_H (estimated from the hydrogen evolution rate) and P_W (estimated from the weight loss rate) for the as-received, USSP treated and polished AZ31 Mg alloy sheet immersed in 3.5 wt.% NaCl solution

sample condition	P_i, mm y^{-1}	P_H, mm y^{-1}	P_w, mm y^{-1}
As-received	0.12	0.95	1.79
USSP-10min	7.44	50.13	none
USSP-10min-20μm	3.62	3.34	8.27
USSP-10min-40μm	0.048	0.44	0.54
USSP-10min-80μm	0.097	0.83	1.815
USSP-10min-100μm	0.095	0.72	1.02

6.3.5 Corrosion Morphology

The typical corrosion morphologies of the as-received, USSP treated and polished AZ31 Mg alloy sheets after the immersion in 3.5 wt.% NaCl solution for 7 days are present in figure 6.9. The corrosion product on the surface after immersion was cleaned by the solution in an ultrasonic container. After immersion for 7 days, all the surfaces show corroded morphologies while the corrosion degrees are different.

For the as-received AZ31 Mg alloy sheet, the corrosion morphology is present in figure 6.9(a). In figure 6.9(a), the corrosion morphology presents a quite uniformly corroded surface meanwhile there are some corroded deep pits on the surface, which is the typical corrosion morphology in Mg alloys. Even though there are lots of pits, the depth of these pits is quite close to each other. Generally, the rolled AZ31 Mg alloys is regarded as an alloy sheet of good corrosion resistance among Mg alloys. There are not much formed second phase in AZ31 Mg alloys sheet because of the limited addition of alloy elements and the high solubilities of Al and Zn, which reduces the galvanic corrosion happened between Mg matrix and second phase (G.-L. Song & Xu, 2012). Meanwhile, the rolled AZ31 Mg sheet always presents a strong basal texture and the (0001) basal plane has a better corrosion resistance than other planes (He et al., 2015). Even though the corrosion resistance of rolled AZ31 Mg alloys is superior to other Mg alloys, after immersed in NaCl solution for a week, there are still several corroded pits. The rectangle area outlined by the dash line in figure 6.9(a) is magnified, seen in figure 6.9(b), to observe the detail corrosion morphology. In figure 6.9 (b), a lot of parallel corrosion features are founded. These features are deep into the matrix and its width are in nano scale and most of them are in one direction. As the as-receive AZ31 Mg alloy sheet has a strong basal plane texture, it can be inferred that these features are along the prismatic planes. This kind of parallel corrosion feature has been reported by McCall, Hill, and Lillard (2005) and M. Liu et al. (2008). The formation of this parallel and nano scale corrosion features are debated until the newest report by Pawar et al. (2017). They used the EBSD technology to confirm these corrosion features are along the prismatic plane. The corrosion rate of different planes in Mg alloys are increased in the order: (0001)

$<(11\bar{2}0)$ $<(10\bar{1}0)$ $<(11\bar{2}3)$ $<(10\bar{1}2)$ (Hagihara et al., 2016). This long parallel corrosion feature should be the result of corrosion along the $(10\bar{1}0)$ prismatic planes. What should be mentioned here is that this parallel corrosion features are cut by some short corrosion lines and these short corrosion lines are all perpendicular to these long parallel corrosion features, highlighted by the red dash line. The 90^o angel between the parallel corrosion features and the short corrosion lines indicates that this short corrosion line should be corrosion features along $(11\bar{2}0)$ prismatic planes. So the corrosion along the prismatic planes results the formation of cross-shaped corrosion features.

For the USSP treated sample, the general corrosion morphology is present in figure 6.9(c). Compared with as-received AZ31 Mg alloys, the USSP treated sample is severely corroded after 7 days immersion in 3.5% NaCl solution. There is a big corroded hole with a diameter of more than 500 μm at the center of figure 6.9(c) and the hole is deeply corroded. The area next to the corroded hole is present in figure 6.9(d). There are a lot of small pits at the surface. For USSP-20 μm polished sample, there is still a huge and deeply corroded hole. The diameter of the huge is close to that of the unpolished sample, indicating the corrosion mechanism of the 20 μm polished sample is similar with that of the USSP treated sample. This is because polishing 20 μm is not deep enough to remove all the Fe particles at the top surface and the reminding embedded Fe particle still have an enormous negative effect on the corrosion resistance. Meanwhile, the area next to the hole at USSP-20 μm polished is present in figure 6.9(f). Unlike the corrosion morphology of USSP treated sample who is full of small pits, the surface of USSP-20 μm polished sample is uniformly corroded, and few small pits are found.

For USSP-40 μm polished sample, the corrosion morphology is present in figure 6.9(g). An extremely uniformly corroded surface is obtained. Compared with as-received AZ31 Mg alloys, there are still some pits found but the size of the pits is decreased obviously. The corrosion morphology of the 40 μm polished sample is quite different from that of as-received. The high-magnified SEM of the corrosion morphology is present in figure 6.9 (h). The corroded surface is full of small round nano-dots with a diameter of several hundreds of nanometers. No parallel corrosion features are found. The corrosion mechanism of the 40 μm polished sample has been changed.

The corrosion morphology of the 80 μm polished sample is shown in figure 6.9 (i) and the high-magnified SEM in figure 6.9 (j). The number of formed pits is a little more than that of the 40 μm polished sample and the size of the pits is similar. In general, the corrosion morphology of the 80 μm polished sample is close to that of the 40 μm polished sample. Besides the nano-dots, there are also several parallel corrosion features found in the 80 μm polished sample, highlighted by the red dash circle. This is because the grain size is not as small as the grain size of the 40 μm polished sample, and the corrosion along some specific planes happens again. For the 100 μm polished sample in figure 6.9 (k), the corrosion morphology is not much different from that of the 80 μm polished sample, still very uniform. The formed pits are slightly more than that of the 80 μm polished sample, but still much less than the as-received as well as the size of pits. However, from the high-magnified SEM in figure 6.9 (l), it can be seen that the detailed corrosion features have changed. There are no nano-dots anymore. Instead, the corroded surface is covered by parallel corrosion features. What should be mentioned is these parallel corrosion features are much shallower than the deep parallel corrosion canyon in as-received sample. At the depth of 100 μm from the top surface, the effect of grain refinement on the corrosion rate is limited. The improved corrosion resistance of 100 μm polished area is mainly due to the formed residual stress(Denkena & Lucas, 2007). According to the result in chapter 4, it can be seen that the distribution of the compression residual stress is much deeper than the gradient nano structure. It is reported that the compression residual stress was benefit for the corrosion resistance (Pu et al., 2012). Meanwhile, the close corrosion rate between 100 μm polished sample and 80 μm polished sample implies that the contribution of grain refinement to the corrosion resistance at 80 μm polished sample is limited.

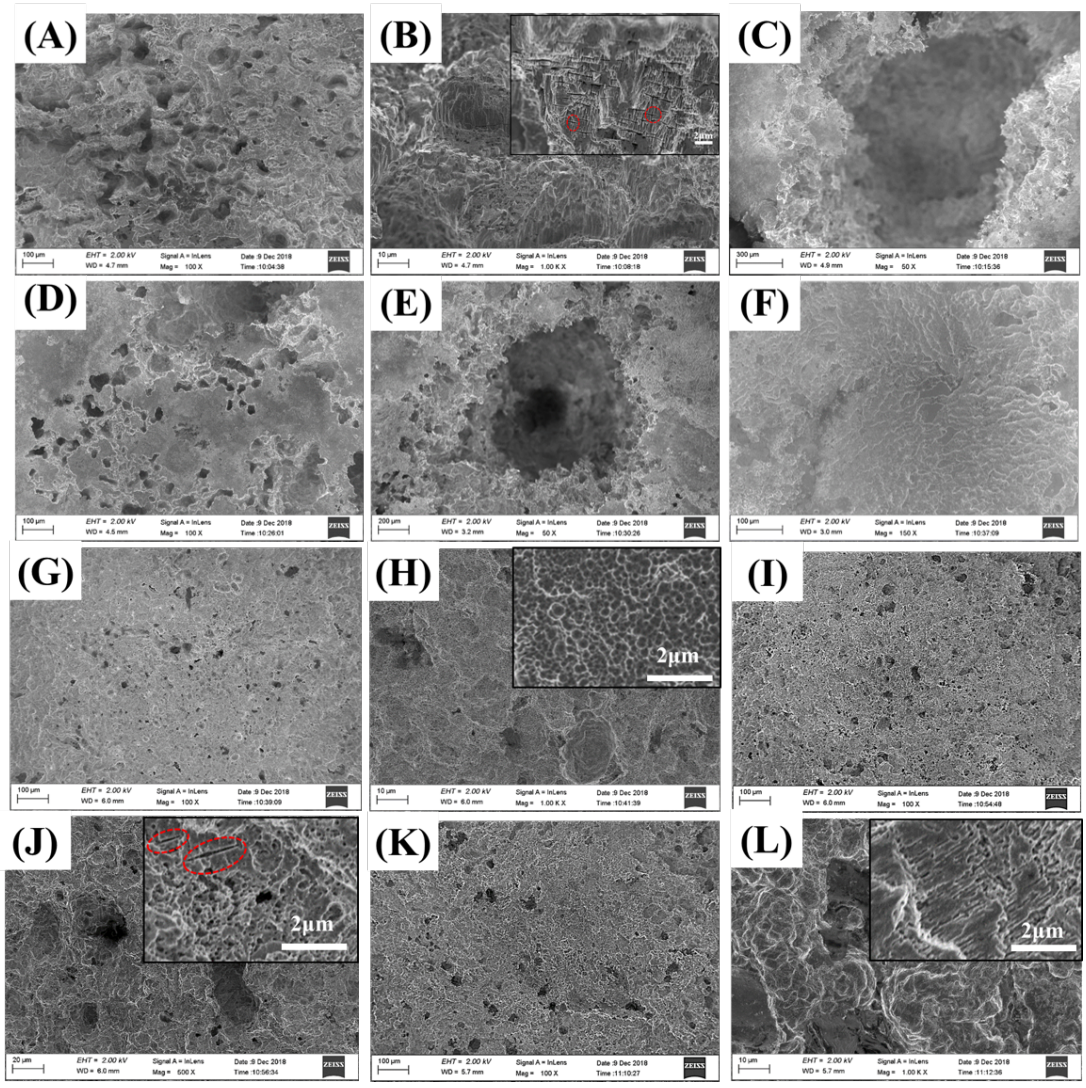

Figure 6.9. The SEM micrographs showing the corroded surface of as-received, USSP treated and polished samples in 3.5% NaCl solution for 7 days: (A) as-received, (B) closed-up of (A), (C) and (D) USSP treated, (E) and (F) 20 μm polished, (G) 40 μm polished, (H) closed-up of (G), (I) 80 μm polished, (J) closed-up of (I), (K) 100 μm polished and (L) closed-up of (K)

6.4 The corrosion mechanism

By manipulating the USSP treatment and the following polishing, different layers along the depth witt different microstructure are obtained. After immersion in 3.5 wt.% NaCl solution for 7 days, the corrosion behavior of the as-received, USSP treated and polished samples are schematically summarized in figure 6.10. For as-received AZ31 Mg

alloy sheet with a strong basal texture, the corrosion happens along the prismatic planes. These hundreds of nanometers in width but deeply penetrated corrosion lines happen both at the $(11\bar{2}0)$ and $(10\bar{1}0)$ planes. This internal corrosion inside of the grain would be stopped by the grain boundary and the new explored grain will be corroded in the further. For the USSP treated sample, the top layer is nanocrystallized. As mentioned before, during the USSP process, there would be Fe particle exfoliated from the stainless-steel shots. These Fe particles will attach at the top surface of the USSP treated area. During the immersion process, the serious galvanic corrosion happens between the matrix and the Fe particle, left the corroded pits at the surface. Because of the formed hydrogen gas and magnesium hydroxide, the Fe particle may be out of the touch with the matrix after the nearby Mg matrix has been corroded, and further has no influence on the corrosion behavior. This kind of Fe particles just affect the corrosion rate at the beginning process. For some Fe particles which are embedded in the Mg matrix, the Fe particles will go deeply into the corroded pits and further corrode the Mg matrix. Finally, a huge corroded hole would form. For the 40 μm polished sample, the explored surface is nanocrystalline, and the attached Fe particles are totally removed. The corrosion happens at the refined grains in the explored surface. As the grain has been refined to nanocrystalline, there are much more grain boundaries, and these grain boundaries act as the barriers of corrosion extension. As a result, a uniformed corrosion morphology is obtained, as shown in figure 5.10 (f).

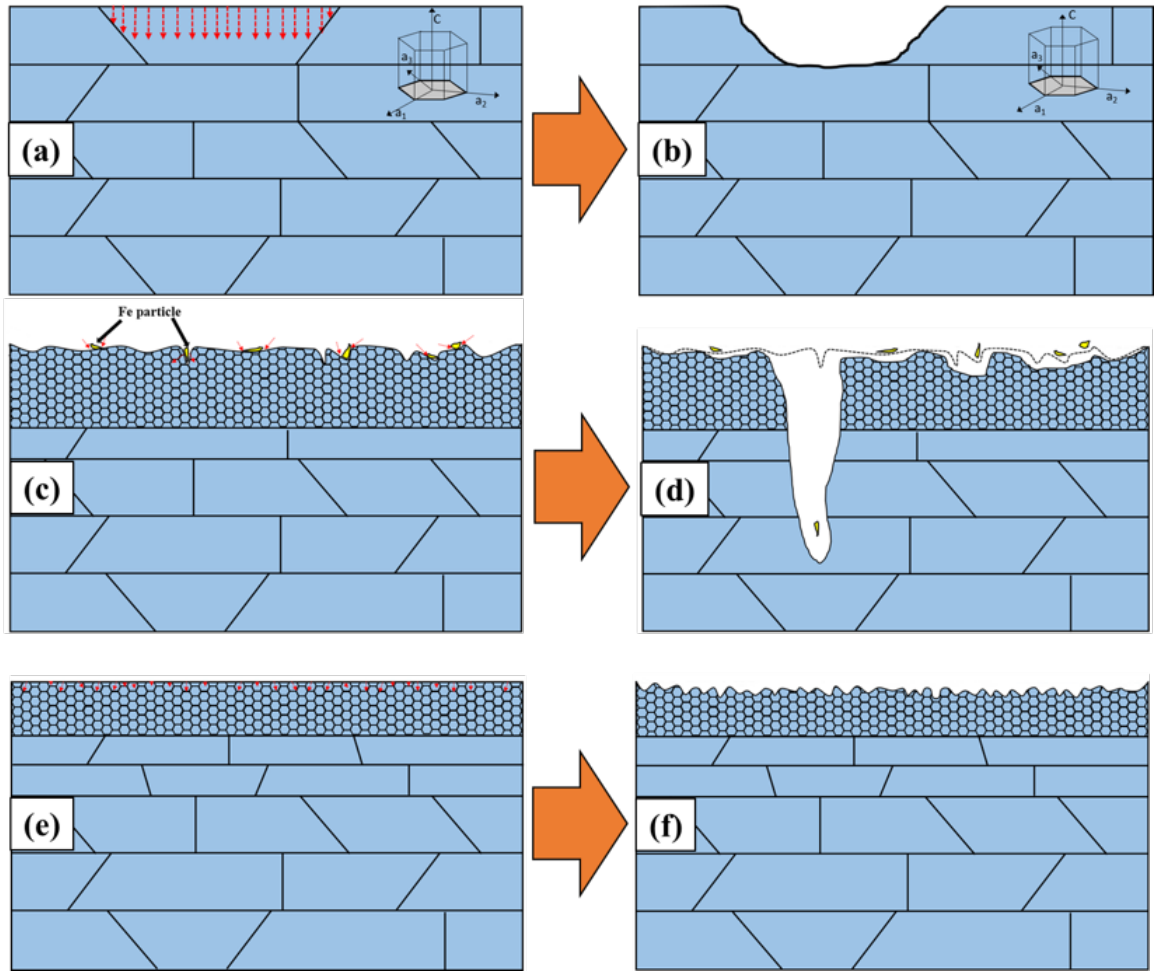

Figure 6.10. Schematic diagrams of the morphology for as-received AZ31 Mg alloy sheet before (a) and after (b) immersion, the USSP treated before (c) and after (d) immersion, and the 40 polished before (e) and after (f) immersion

6.5 Summary

In this chapter, an experimental investigation has been performed to study the corrosion behavior of the as-received AZ31 Mg alloy after USSP treatment and the following polishing. The corrosion behavior was investigated by the electrochemical test, hydrogen evolution test and mass loss test. The corrosion morphology after immersion for a week was also observed. The major conclusions from the experimental corrosion behavior study were summarized as following:

The corrosion resistance of AZ31 Mg alloy was significantly reduced after USSP treatment in 3.5 wt.% NaCl solution because of the Fe particles at the top surface of the USSP treated sample, and these Fe particles were exfoliated from the shot during the USSP treating process.

A 20 μm polishing of USSP sample could reduce the corrosion rate but still much higher than that of the as-received.

The reduced corrosion resistance of the USSP treated and 20 μm polished samples was due to the increased current density of the cathodic reaction during the immersion, which was because of the increased reaction sites during the corrosion process.

A 40 μm polishing of USSP sample improved the corrosion resistance greatly. The corrosion rate was half of the as-received. The corrosion rate of 80 μm and 100 μm polished samples was increased but still lower than that of as-received.

The improved corrosion resistance of the 40-100 μm polished sample was due to the reduced current density of the anodic reaction during the immersion. The reduced current density of the anodic reaction was because of the compression residual stress and the higher speed of protective layer formation during the corrosion process.

From the corrosion morphology, the grain boundary could protect the matrix and acted as the corrosion barrier. The massive amount of grain boundary in the nanocrystalline improved the corrosion resistance of Mg alloys and resulted in a uniform corrosion morphology.

CHAPTER 7. EXPERIMENTAL STUDY ON BENDING BEHAVIOR OF ULTRASONIC SHOT PEENING TREATED AZ31B MAGNESIUM ALLOY

7.1 Introduction

In chapter 4, it is found that the USSP treatment can improve the mechanical strength and hardness while its ductility is reduced greatly. From chapter 5, the result shows the improved strength can enhance the wear resistance of AZ31 Mg alloy. In chapter 6, the corrosion resistance of AZ31 Mg alloy also increases due to the nanocrystalline structure. In addition to these advantages provided by the nanocrystalline structure, the possible disadvantages caused by the reduced ductility should be considered.

The formability of a material is a property that is related closely to its ductility (Hull & Clyne, 1996). For AZ31 Mg alloy sheet, the formability is relatively poor compared with Al alloy sheet, or steel. The limited formability of AZ31 Mg alloy sheet is due to the formed strong basal texture and its limited slip systems (Agnew & Duygulu, 2005). It is necessary to investigate the effect of the reduced ductility of USSP treated samples on the formability of AZ31 Mg alloy sheet. The bending performance of a material is a useful index to estimate its formability. So it is necessary to investigate the effect of USSP treatment on the bending behavior of AZ31 Mg alloy sheet.

In this chapter, the effect of surface nanocrystalline by USSP treatment is investigated by a V-bending test. The experimental study of bending behavior with different thickness of surface nanocrystalline is conducted. Meanwhile, the bending behavior of the single side treated AZ31 sheet is also applied to study the effect of surface nanocrystalline position on the bending behavior. The microstructure evolution, including the twinning behavior, the strain distribution, the grain orientation is measured by EBSD

analyze technology. Besides, the bending process is simulated by ABAQUS software to study the distribution of stress and strain after bending. A quasi in-situ EBSD is also conducted to study the microstructure evolution and strain distribution during the bending process as well as the effect of surface nanocrystalline on them.

The results show that the both sides USSP treated sample has a similar bending performance with the as-received, regardless of the USSP treated time. The result implies the reduced ductility after USSP treatment does not lead to a worse bending performance. Moreover, the bending performance of the USSP inner treatment can reduce the shift of neutral layer during the bending process, and improve the bendability. Moreover, the outer side treatment can improve the bendability greatly. The EBSD results and FEM simulation results show that the improved bending performance is due to the re-distribution of stress and strain. With a nanocrystalline at the outer surface layer, its higher yield stress leads to the more strain at the inner layer during bending. The relationship between the thickness and the position of surface nanocrystalline and the bending performance is also discussed.

7.2 Experimental setup and sample preparation

To study the bending behavior of the ultrasonic shot peening treated AZ31 Mg alloy sheet, a V-bending test at room temperature was designed, using a die with an included bend angle of 120 and a tip-radius of 4 mm. The test specimen was cut by CNC cutting machine from the center of the treated area, with a size of 50 mm$\times$12 mm$\times$3 mm (RD$\times$TD$\times$ND). All tests were conducted at a loading speed of 3mm/min.

In order to investigate the effect of gradient nano structural thickness on the bending behavior, three USSP treatment times (5 min, 10 min and 15 min) were employed. The samples were treated at both sides of the TD$\times$RD plane to obtain different thickness of gradient nano structure, shown in figure 7.2 (b). This sample is named as: USSP-both.

Meanwhile, a single side treatment at the TD×RD plane was conducted to investigate the effect of asymmetrical structure on the bending behavior. The AZ31 Mg alloy sheets had a single side treatment to obtain a gradient nano structure while the opposite side was left untreated with the original grain structure. The treated side was placed at the internal or external side during the bending process, shown in figure 7.2 (c) and figure (d). The gradient nano structure at internal is named as: USSP-inner and gradient nano structure at external is named as: USSP-outer.

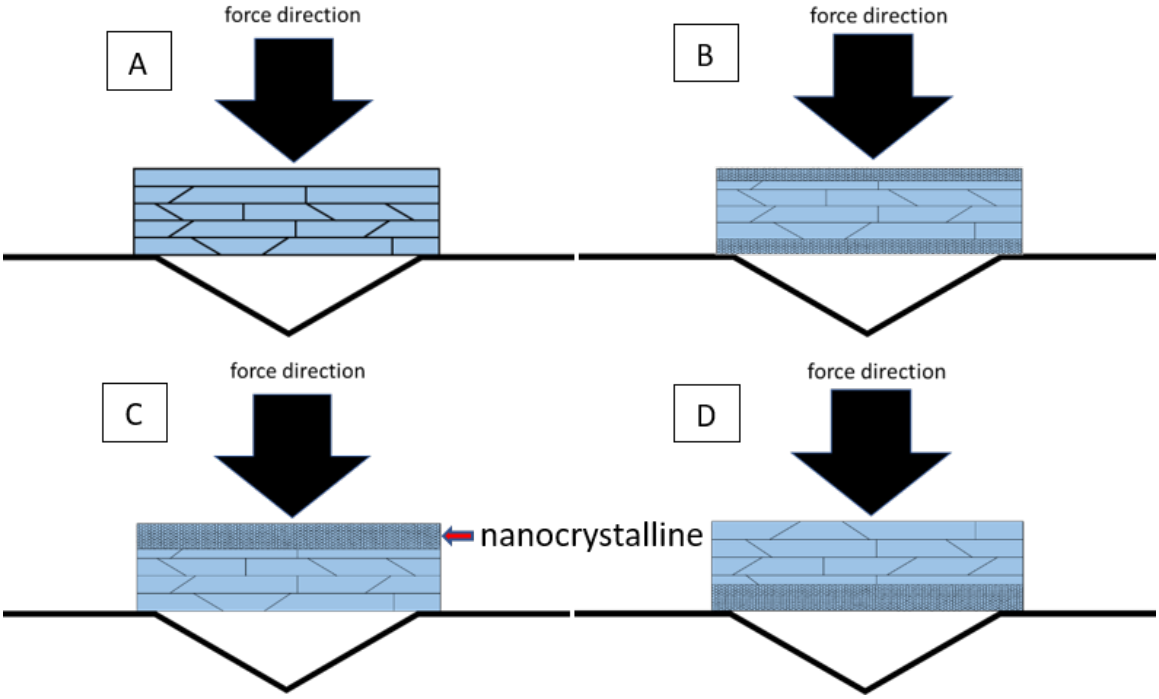

Figure 7.1. The Schematic diagrams of the position of nano structure during bending process: (a) the as-received, (b) nano structure at both sides, (c) nano structure at the internal side, (d) nano structure at the external side

The morphology of the bending sample and the microstructure evolution after bending was characterized and analyzed by OM and EBSD. For the morphology of the crack, a macro picture after bending was present. The crack morphology observed from the TD direction was present by the OM. For EBSD, the sample was taken from the area close to the fracture. The sample was electrochemically polished before EBSD characterization.

7.3 The effect of USSP treated time on the bending behavior

The load-stroke curves of magnesium alloy sheets with different USSP treated time are present in Figure 7.2. From the load-stroke curves, it is seen that the bending ability of the USSP treated sample is closed to the as-received. All four curves present a similar punch distance of about 4.5 mm, before crack and fracture occurrence. The required bending load is increased after USSP treatment and the increase of USSP time results in a higher bending load value. In chapter 4, it is found that the USSP treatment will increase the mechanical stress while sacrifices its ductility. The ductility is always regarded to be a key factor that will affect the bendability of the material. Here, the reduced ductility in USSP treated Mg alloy does not have obvious detrimental effect.

The morphology of the sample after bending and the optical microscopy picture of the fracture from the TD direction is present at figure 7.3. For the as-received AZ31 Mg alloy in figure 7.3(a), there is an obvious macro crack at the outer side. For the USSP-both samples, they present a similar bending behavior so the USSP treatment of 10 min is selected and present in figure 7.3(b). The black area is the USSP treated area and a macro crack is also present. From the optical microscopy of the fracture in figure 7.3 (c), the crack is penetrated to the matrix for more than 500 μm. The crack is close to 45^o from the force load direction, indicating it is caused by the shear stress. For the USSP-both, the crack is also similar, with a 45^o. What should be mentioned is that there are some small cracks with multi-directions happening at the inner sider of the USSP-both, which is not found in as-received.

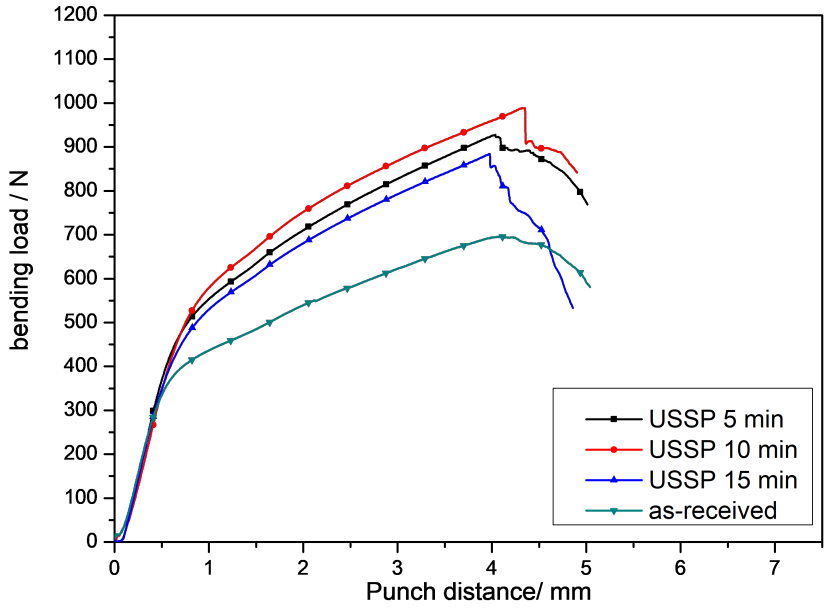

Figure 7.2. The load-stroke curves of USSP-both magnesium alloy sheets with different USSP treated time

The schematic illustration of bending process is shown in figure 7.4. During the bending process, the outer region of the sheet, which is the c region in figure 7.4, is under tension. For the inner region of the sheet, it is under compression. The rolled Mg alloys always presents a tension-compression yield asymmetry, which leads to the shift of neutral axis (Huang & Han, 2013). In this study, from the tensile and compression result in chapter 4, the CYS/TYS value for the as-received is 0.61. After the USSP treatment, the CYS/TYS values are 0.62, 0.53 and 0.65, respectively. So, the USSP cannot improve the tension-compression yield asymmetry. That may be one of the reasons why the bendability of the sheet after USSP treatment is similar to that of the untreated.

To clearly observe the microstructural evolution during the bending, an EBSD analysis was employed from the TD direction. In figure 7.5, the whole section of the USSP-both with 10 min treatment from the TD direction was conducted to evaluate the microstructure evolution. The sample is taken from the area close to the fracture. The

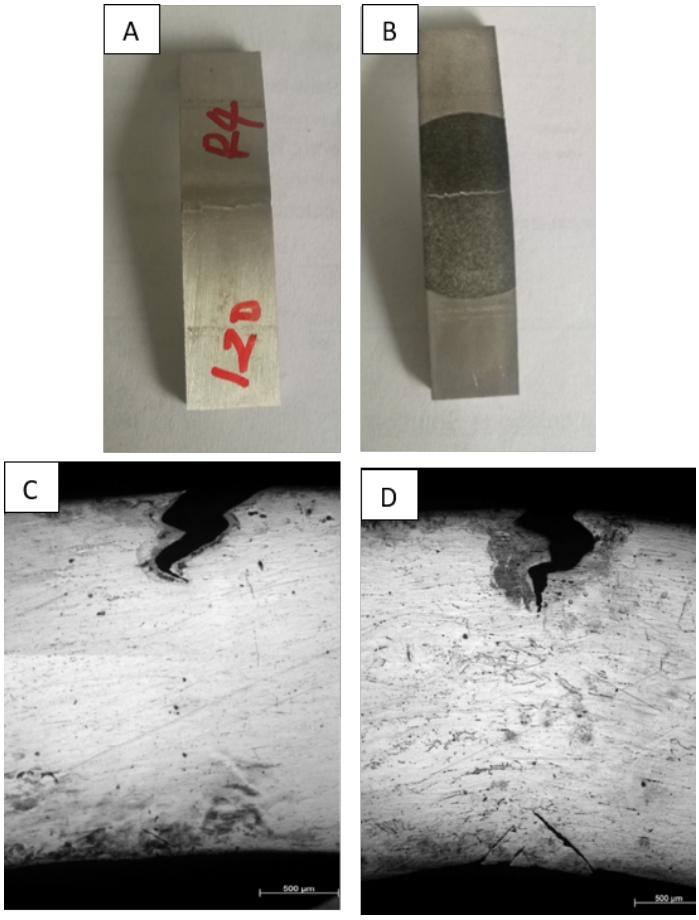

Figure 7.3. The morphology of the sample after bending: (a) as-received and (b) USSP-both, and the optical microscopy picture of the fracture from the TD direction: (c) as-received and (d) USSP-both

detection area is about 3mm×1.5mm. The top surface at the outer layer is the white area and this area is unable to detect the full amount of local stress. This area is the combination result of the USSP process and bending process. The bottom area is close to the top area. From the inverse pole figure (IPF) maps from TD directions, it shows a prismatic orientation, which is the same as the orientation before bending. The twin structure is observed, and it is found the twin is mainly distributed at the bottom half area. An IPF map from the RD direction is also present. From the IPF from RD direction, an obvious microstructure change during the bending process is present. For the outer zone, a prismatic orientation is kept after bending. For the middle zone, it contains both prismatic

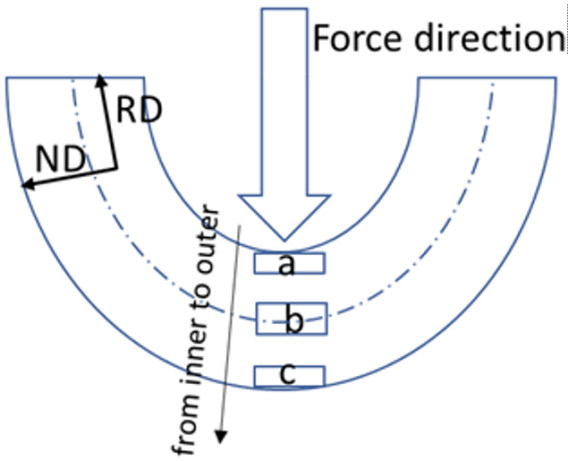

Figure 7.4. The schematic illustration of the bending process

and basal orientations. For the inner zone, just a basal orientation is observed. So, the sheet after bending presents different textures along the thickness. During the V-bending process, the outer surface zone is under tension and the inner surface zone is under compression. In the outer zone, the strong basal plan texture results in the dominated deformation mechanism was the prismatic slip (Robson, Stanford, & Barnett, 2011). For the inner zone, the compression was loaded perpendicular to the c-axis of the grains. This leads to the happening of $(10\bar{1}2)$ tension twin. As the rotation of tension twins is 86^o, the c-axis of the grains at the inner zone is rotated from the ND direction to the RD direction, which results in the shift of red in the IPF map from RD direction. Meanwhile, a part of the middle zone area is also shifted to red, which means the middle zone is under compression and the natural layer is shifted towards the outer region after bending. The critical shear stress for $(10\bar{1}2)$ tension twin is much smaller than that of the prismatic slip (Barnett, 2007). So, the deformation in the inner zone is much easier than that in the outer zone. This asymmetry between tension and compression results in the shift of the natural layer to the outer region.

For the as-received sample, the outer surface zone is present in figure 7.6(a). The outer surface layer is under tension during the bending process, and few twin structures are observed. For the middle layer in figure 7.6(b), the upper part is similar to that in the outer surface layer, which is under tension during the bending. The lower part is quite

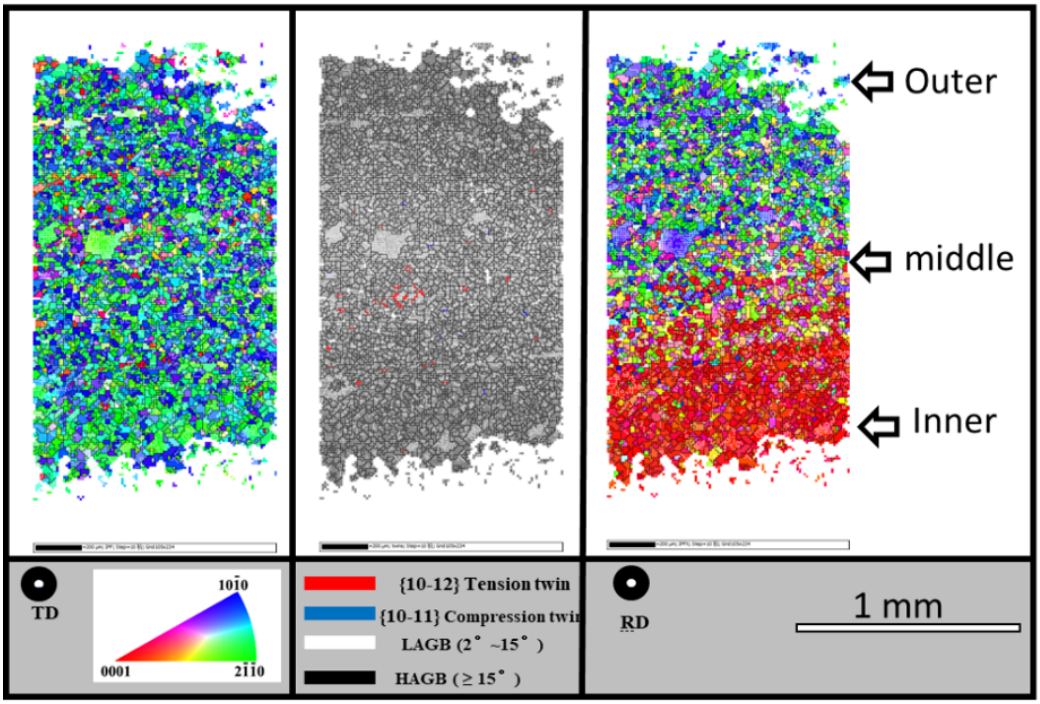

Figure 7.5. The EBSD characterization of the microstructure from the TD direction after bending for USSP-both 10 min sample

different, which is full of twin structures. From the IPF of RD direction, it clearly presents a lot of grain rotation, which is the shift of c-axis from the ND to the RD direction. For the inner surface layer, the shift of c-axis happens at the almost all grains. Meanwhile, there are lots of white areas, meaning these areas are under heavy deformation.

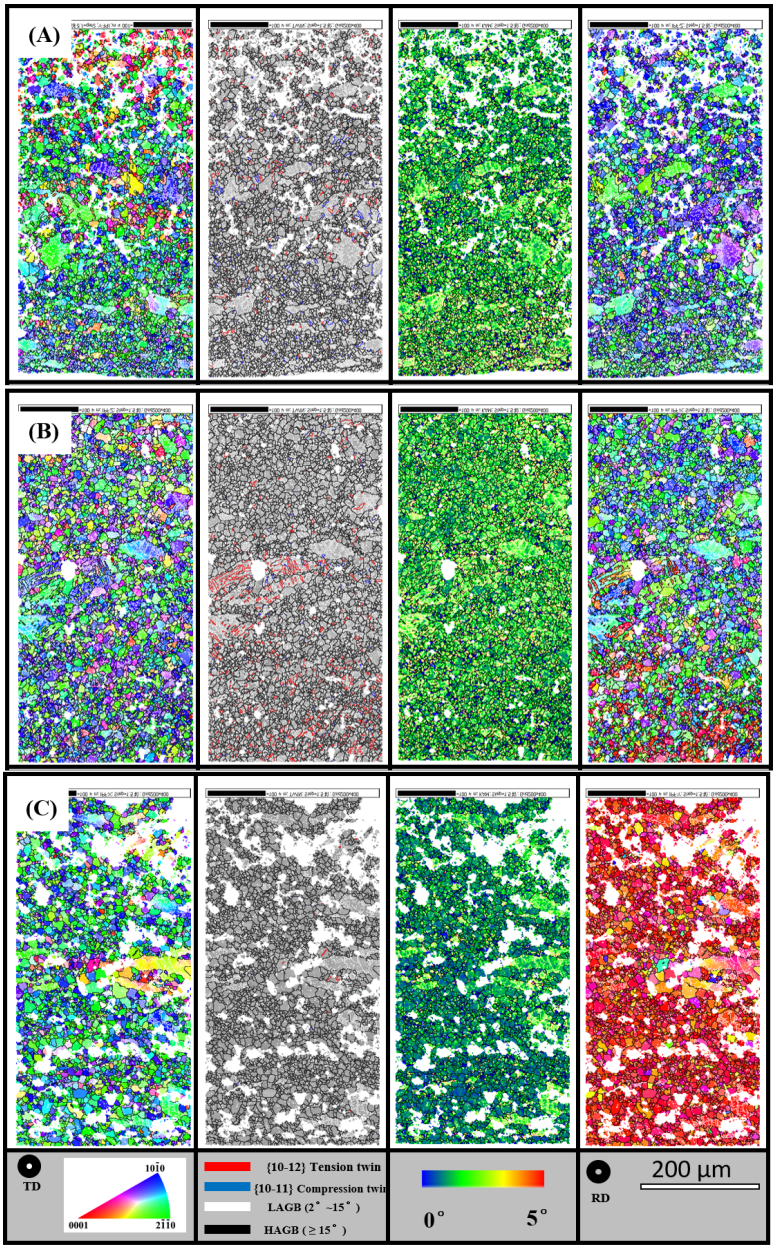

Figure 7.6. EBSD maps of the various positions: (a) outer surface zone, (b) middle zone and (c) inner surface zone of as-received

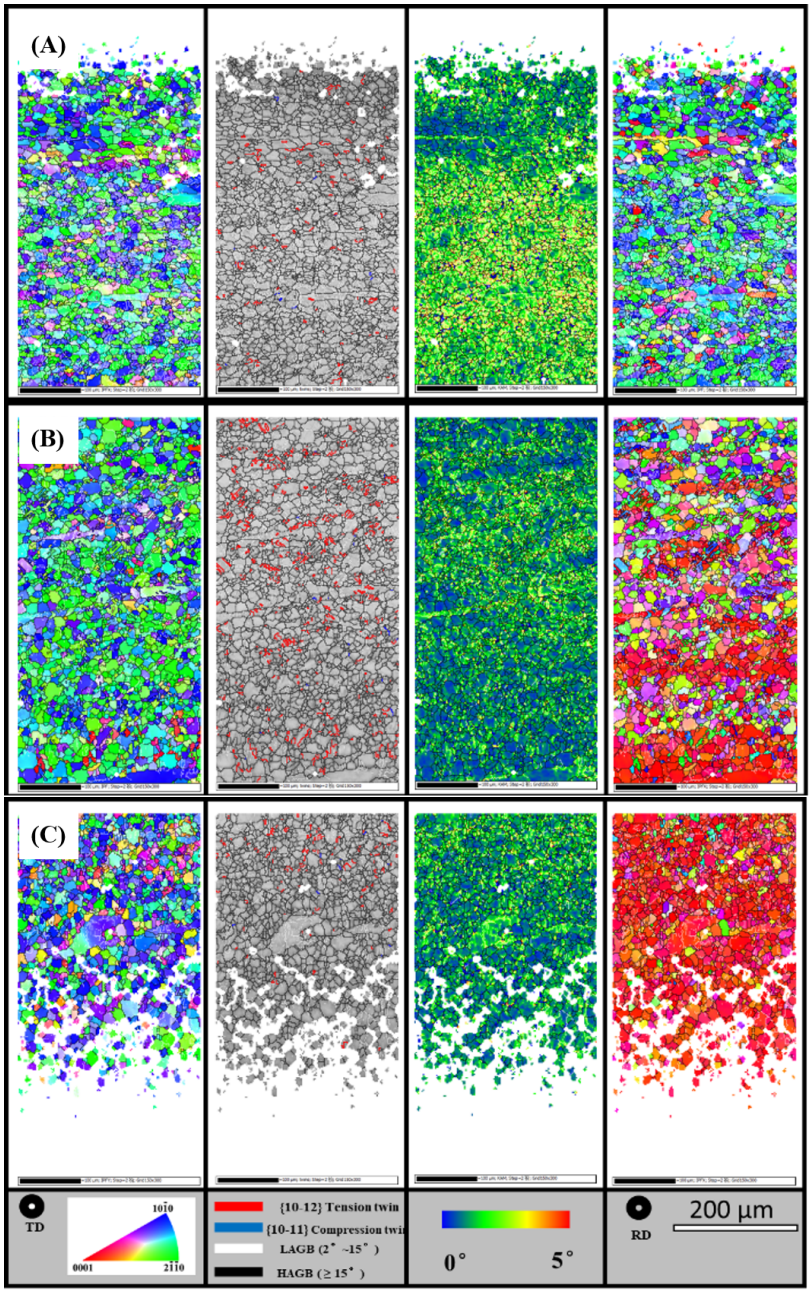

Figure 7.7. EBSD maps of the various positions: (a) outer surface zone, (b) middle zone and (c) inner surface zone of the USSP-both 10 min

The detailed EBSD maps of the USSP-both 10 min sample are present in figure 7.7. For the outer surface zone of USSP-both in figure 7.7(a), the outer zone is under tension and there are few twins found, which is the same as as-received. The surface area is the nano structure zone which is not detectable. The grains at the interface area of the

nano structure and the matrix hardly deformed, indicating the interface is not the weak point during the bending. From the KAM map, a stress band of 45^o is distributed. For the middle zone in figure 7.7(b), a lot of $(10\bar{1}2)$ tension twins are found. In the IPF map from the RD direction, it clearly presents an area full of different orientations, indicating part translation of the grain orientation. For the inner zone in figure 7.7(c), the surface area is the gradient nano structure. The area close to the gradient nano structure is also full of the white area, implying the area is also heavily deformed. The rest of the area is totally red, which means the grains in the inner zone are completely shifted from the basal plane texture to a prismatic texture with c axis along the RD direction. What is interesting is the $(10\bar{1}2)$ tension twin fraction in the inner zone is 3.09%, which is smaller than that of the middle zone, 5.6%. The inner zone undergoes a more serious compression during the bending process. After the grains have been shifted from the basal plane texture to prismatic texture, the c axis is along the RD direction. The further compression of the shifted grain is along the c-axis. The compression along the c-axis will result in the formation of $(10\bar{1}1)$ a compression twin. However, the CRSS value of $(10\bar{1}1)$ the compression twin is as high as $\sim$ 114 Mpa. After the original grains with the basal plan texture consumed, the formation of twin becomes harder. The formed $(10\bar{1}2)$ tension twin disappears after the grain has been total shifted and the fraction of $(10\bar{1}2)$ tension twin is reduced. The decreased $(10\bar{1}2)$ tension twin and hardly formed $(10\bar{1}1)$ compression twin result in its twin fraction is lower than the middle zone.

7.4 The effect of USSP treated layer position on the bending behavior

7.4.1 USSP-inner treated

The load-stroke curves of USSP-inner magnesium alloy sheets with different USSP treated time are shown in Figure 7.8. From the loadstroke curves, it is seen that the bending ability of the USSP-inner sample is quite different from the as-received and USSP-both. It is clearly found that the bending loads of the USSP-inner are higher than

the as-received. Even though the USSP-inner is treated at one side, there is an obvious enhancement of the mechanical strength. Meanwhile, all these USSP-inner samples show a better bending performance than the as-received. The USSP-inner 5min sample presents the best bendability, reaching 6.5mm before fracture. After 10min USSP treatment, the bendability is reduced to $\sim$ 6mm. The bending performance of 15 min treated sample is slight better than the as-received. This asymmetric structure improves the bending performance and the USSP treated time influences the bendability.

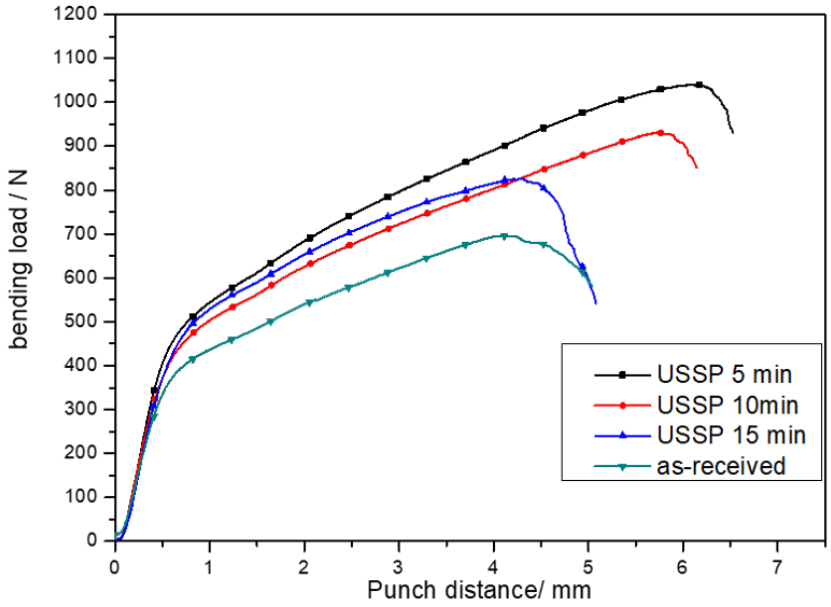

Figure 7.8. The load-stroke curves of USSP-inner magnesium alloy sheets with different treated time

The morphology of the USSP-inner sample after bending and the optical microscopy picture of the fracture from the TD direction are present in figure 7.9. An obvious macro crack is present at the convex of the outer side for each sample. From the optical microscopy of the fracture, the crack is penetrated to the matrix for more than 800 μm and the crack is close to 45^o from the force load direction, indicating it is caused by the shear stress. In the inner zone, there are some small cracks happening of the USSP-inner, which is also found in the USSP-both samples. So the gradient nano structure is easier to generate the cracks during compression.

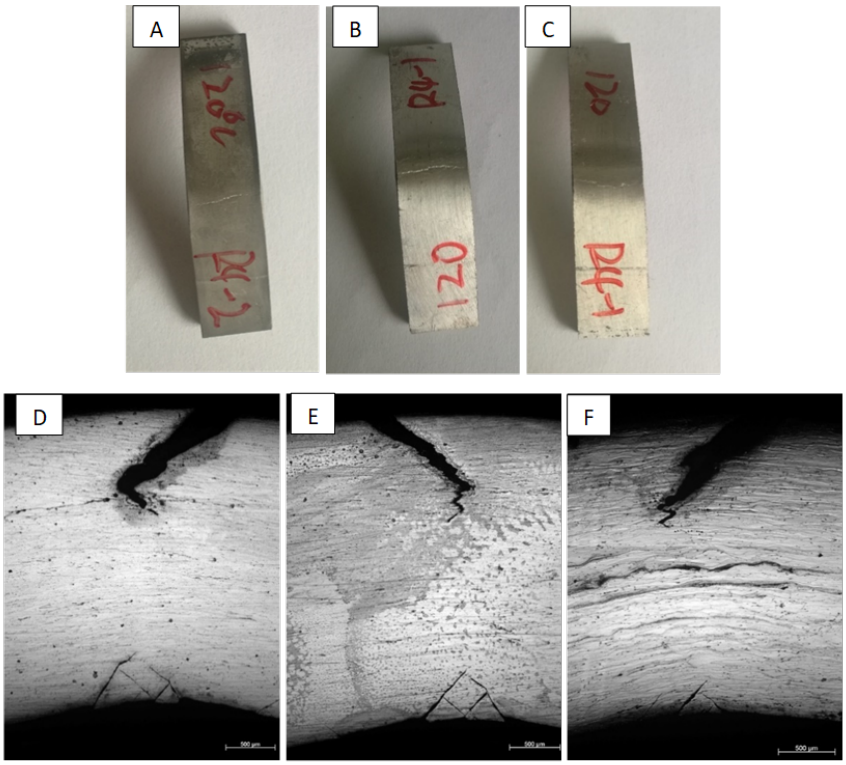

Figure 7.9. The morphology of the USSP-inner sample after bending: (a) 5 min, (b) 10 min and (c) 15min, the optical microscopy picture of the fracture from the TD direction: (d) 5 min, (e) 10 min and (f) 15min

The EBSD maps of the outer surface zone, middle zone and inner surface zone for USSP-inner 5 min and 15 min samples are shown and compared in figure 7.10 and figure 7.11. For the outer surface zone of USSP-inner 5min sample, the edge of the outer surface is clearly detected while more white area in the 15min sample. The twins in the outer zone of the USSP-inner are barely found, just like the as-received. For the middle zone, both the USSP-inner 5 min and 15 min samples presents the shift of c-axis, which is turned to red in the IPF map from the TD direction. What should be mentioned is that, the percent of red area in the USSP-inner 5min sample is more than that of the USSP-inner 15min sample. For the as-received and USSP-both samples, the neutral layer of Mg alloys will shift to the outer region during the bending process. For the USSP-inner sample, the

induced gradient nano structure can pull the neutral layer back and a thicker gradient nano layer can have a more obvious effect. For the inner zone, the USSP-inner 5min sample is totally red and the twin percent is also smaller than the middle zone. The result is similar in USSP-inner 15 min samples.

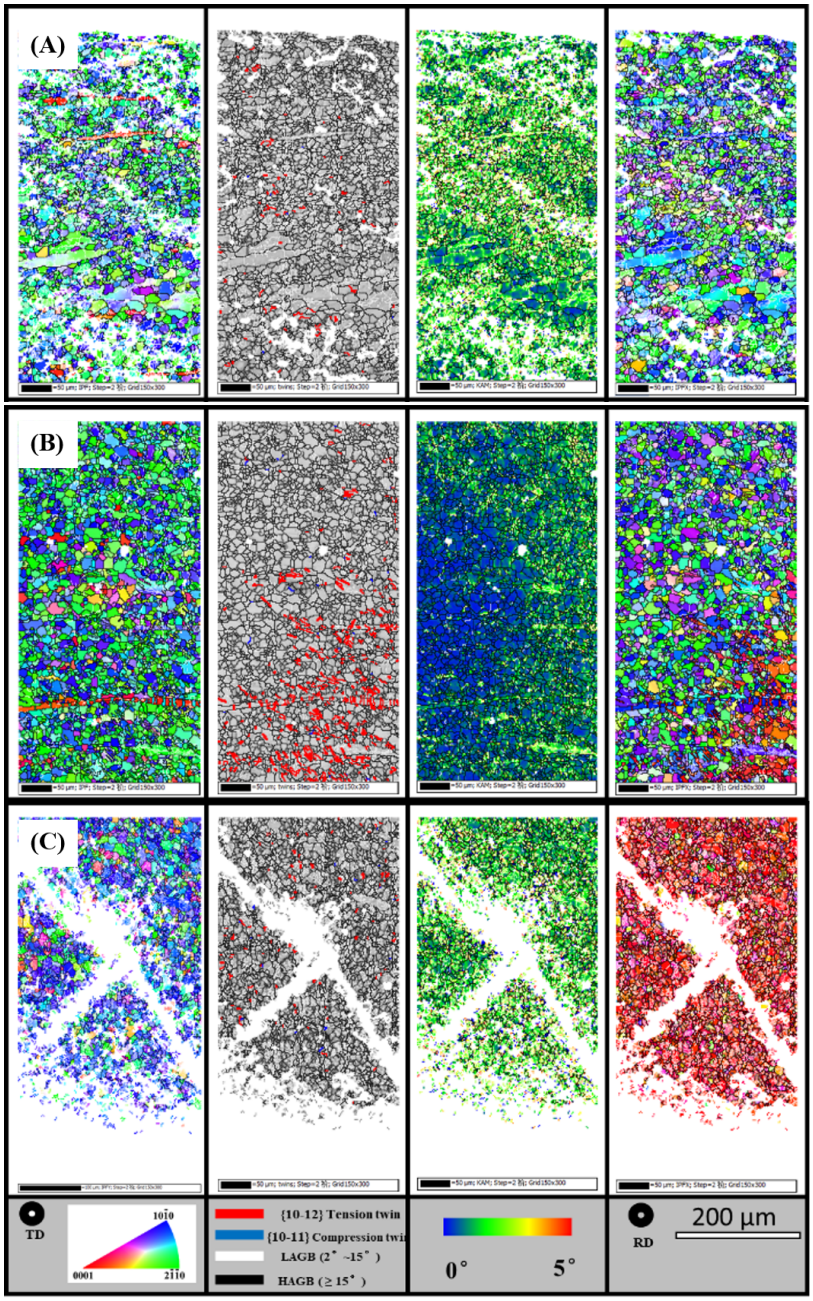

Figure 7.10. EBSD maps of the various positions: (a) outer surface zone, (b) middle zone and (c) inner surface zone of USSP-inner 5 min.

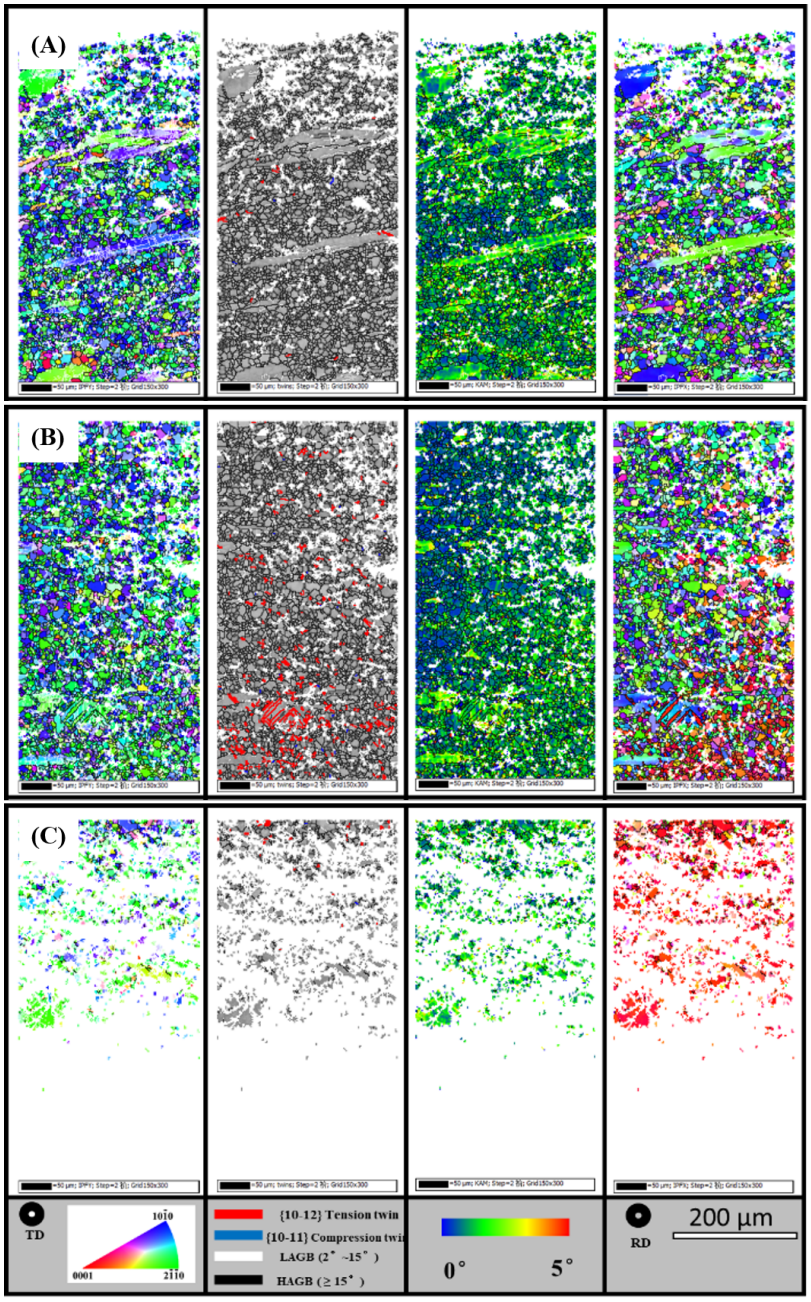

Figure 7.11. EBSD maps of the various positions: (a) outer surface zone, (b) middle zone and (c) inner surface zone of the USSP-inner 15 min.

7.4.2 USSP-outer treated

The load-stroke curves of USSP-outer magnesium alloy sheets with different USSP treated time are present in Figure 7.12. From the load-stroke curves, it is seen that the USSP-outer sample shows a totally different tendency from the as-received and USSP-inner. For the USSP-inner 5min sample, the curve is similar to as-received and the sample fractures at a load distance of 4.5 mm. For the USSP-inner 10min sample, the bending load becomes smaller than that of as-received. The loading distance before fracture is also just $\sim$ 4.5 mm. For the USSP-inner 15min sample, the increased value of the load at the tail of the curve indicates the sample has touched the die mold and is successfully shaped, and the needed bending load of the USSP-outer 15 min is the smallest among them. It is well known that the gradient nano structure can improve the mechanical strength due to the obvious grain refinement. Here, the placed gradient nano structure at the outer surface zone reduces the needed load value during the bending process.

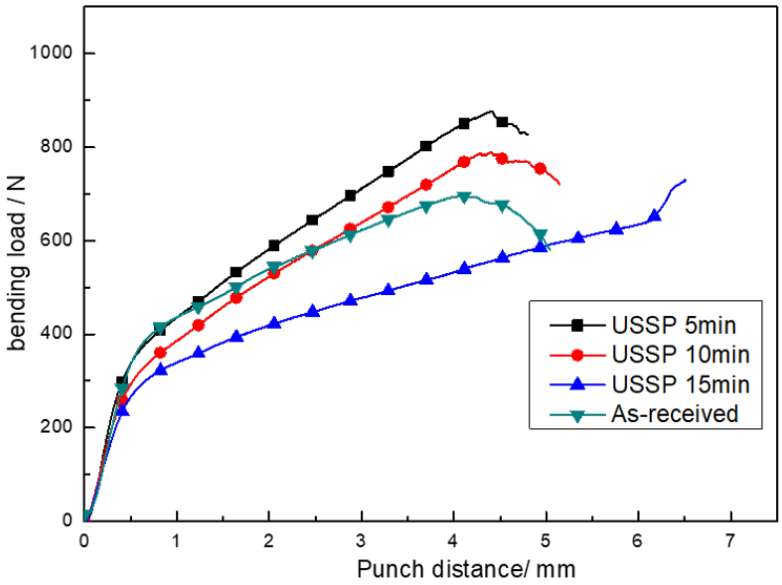

Figure 7.12. The load-stroke curves of USSP-outer magnesium alloy sheets with different treated time

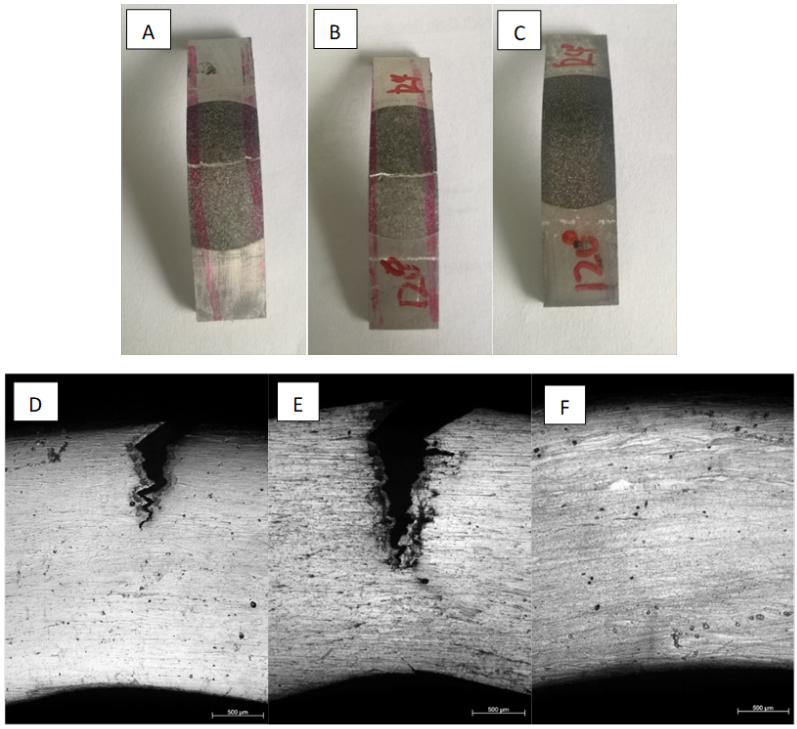

Figure 7.13. The morphology of the USSP-outer sample after bending: (a) 5 min, (b) 10 min and (c) 15min, the optical microscopy picture of the fracture from the TD direction: (d) 5 min, (e) 10 min and (f) 15min

The morphology of the USSP-outer sample after bending and the optical microscopy picture of the fracture from the TD direction are shown in figure 7.13. Cracks are found in USSP-outer 5 min and 10 min samples, just as the as-received and USSP-inner samples. No macro cracks is present at the convex of the outer side at the USSP-outer 15 min sample. From the optical microscopy of the fracture, the USSP-outer 15min sample is crack free, at both the inner side and outer side. The USSP-outer 15 min sample can be molded at this bending condition. The EBSD of the outer surface zone, middle zone and inner surface zone for USSP-outer 5 min and 15 min samples are also shown and compared in figure 7.14 and 7.15. For the outer surface zones of USSP-inner 5min and 15 min samples are white areas, which are the gradient nano structures induced by USSP process. In the outer zone, the slip still dominates the main contribution of the plastic deformation and few twins are found. In the outer zone of the USSP-outer 5 min

and 15 min samples, both present the shift of c-axis, observed from the IPF map of RD direction. The proportion of the red area in the 5 min sample is less than that in the 15 min sample, which is different from the USSP-inner samples. For the USSP-inner sample, the red area in the 5 min sample is more than that of the 15 min sample. In the inner zone, unlike the USSP-inner sample, there is no multi-directional cracks. There is less white area, compared with the USSP-inner sample. This result shows that there are fewer occurrences of local stress concentration in the USSP-outer sample. The less white area in USSP-outer 15 min samples implies that the increased treatment time can reduce the local stress concentration.

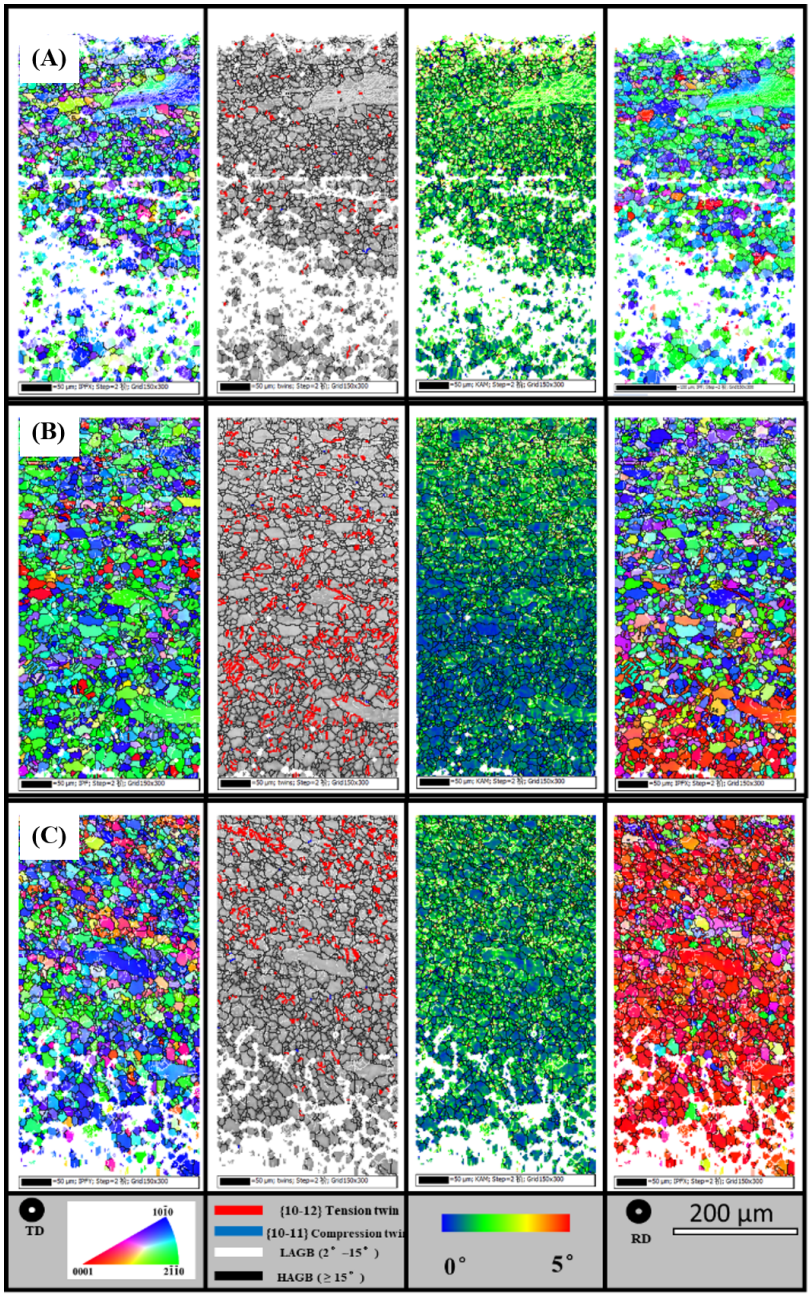

Figure 7.14. EBSD maps of the various positions: (a) outer surface zone, (b) middle zone and (c) inner surface zone of USSP-outer 5 min.

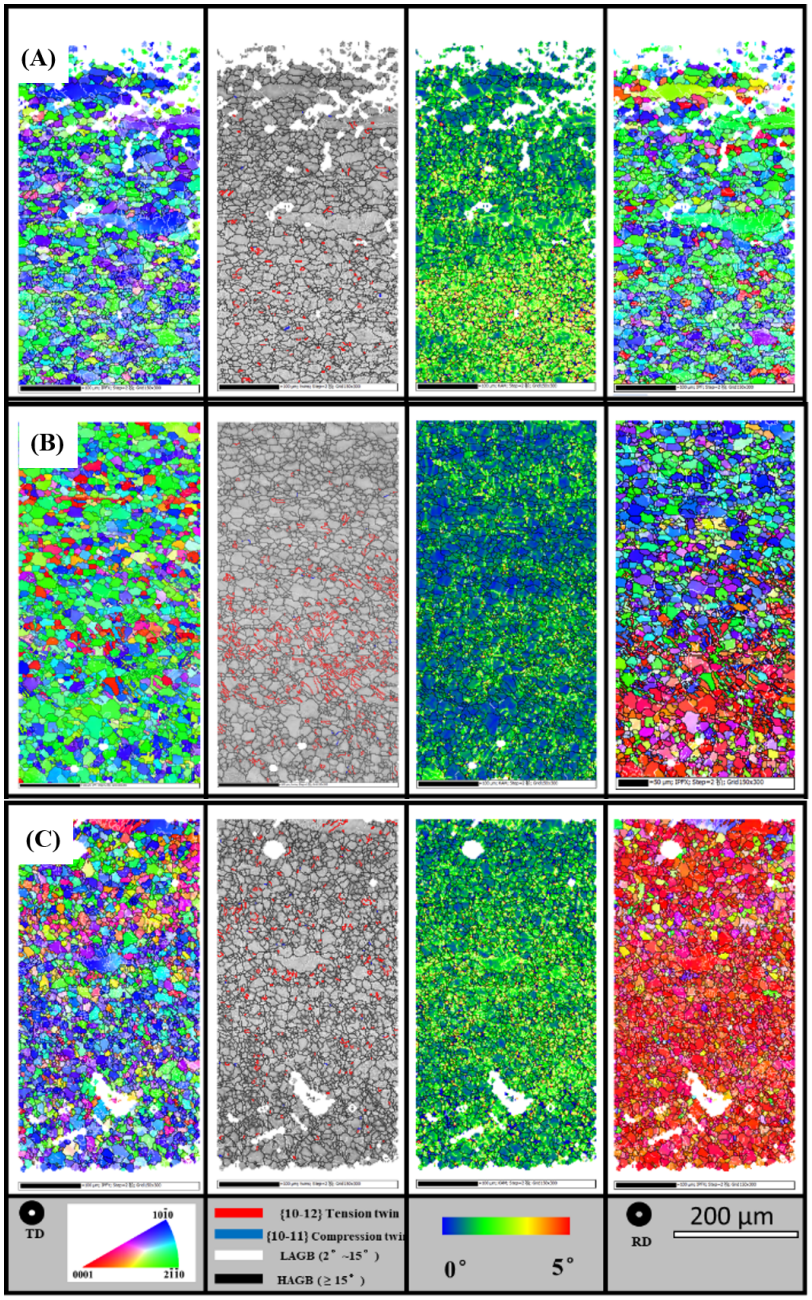

Figure 7.15. EBSD maps of the various positions: (a) outer surface zone, (b) middle zone and (c) inner surface zone of USSP-outer 15 min.

The above results show that the asymmetric structure induced by the single side treatment can change the bending behavior of AZ31 Mg alloy sheet. The single side treated samples show better bending performances, compared with the as-received. The different placed positions of the gradient nano structure not only influence the bending

load values, but also affect the load distance. Moreover, the USSP treated time also has an effect on the bending performance. For the USSP-inner, the 5 min sample shows the best bending performance while the further increase of treated time will reduce its bendability. For the USSP-outer, the longer treatment time, the better bending performance. The 15 min treated sample shows the best bendability. The improved bendability of the single side treated sample is due to its asymmetric structure. During the bending process, the outer zone undergoes a tension stress and the inner zone under compression. For the as-received AZ31 Mg alloy sheet with a strong basal texture, the $(10\bar{1}2)$ tension twin contributes the plastic deformation at the inner zone, and the low CRSS value for $(10\bar{1}2)$ tension twin results in its easy activity. In the outer zone, the dislocation slips mainly contribute to the plastic deformation, and the strong basal plane texture results in the low Schmid factor for the basal plane slip. The deformation in the inner zone is much easier than the deformation in the outer zone. So the fracture of the AZ31 Mg alloy sheet always happens at the convex of the outer layer, which undergoes the highest tension strain and stress. For the USSP-outer samples, the outer surface zone is replaced by the gradient nano structure with a higher mechanical stress. Even though the nano structure is of limited ductility, the higher yield stress can prevent the occurence of cracks.

For the USSP-inner sample, the gradient nano structure forms multi-directional cracks during compression. The improved bendability of the USSP-inner samples may be due to its effect on the neutral layer. As mentioned, the inner zone and the outer zone undergoes different deformation models. The asymmetry of the deformation between the outer and inner zones results in the shift of the neutral layer. The coefficient of the neutral layer, K-value, is a standard to measure the offset of the neutral layer, and the K-value can be expressed as the followings:

$$k = 0.5\beta^2 + \frac{\beta - 1}{t}R \tag{7.1}$$

where β, R and t are the coefficient of incrassation, the inside bending radius and the original thickness, respectively. $\beta=(t_1-t)/t$ and t_1 is the thickness after bending. When the k-value is less than 0.5, it means the neutral layer has been shifted to the inner zone, and a k-value more than 0.5 means the shift to the outer zone. From the equation, it is clearly found that the k-value is strongly connected with the change of thickness before and after bending. In this study, the R values cannot be measured correctly because the majority of the samples are fractured during the bending and a additional load occurs. So the β value is calculated to represent the shift of neutral layer. A positive value of β means the shift towards the outer zone and a negative value means to the inner zone. The values of all the test samples are summarized in table 7.1. The β values of the as-received has a value of 0.023, which means the neutral layer of the as-received AZ31 sheet shifts to the outer zone during bending. For the USSP-both samples, the β values for 5 min, 10 min and 15 min are 0.015, 0.02 and 0.011, respectively. So the USSP at both sides cannot alter the shift of neutral layer. For the USSP-inner 5 min sample, the β value is just 0.0004, which means the shift of the neutral layer is very limited. For the USSP-inner 10 min and 15 min samples, the β values become negative, which means the neutral layer shifts towards the inner zone. For the USSP-outer samples, the β values for 5 min, 10 min and 15 min are 0.041, 0.034 and 0.04, respectively, which is bigger than that of the as-received. The bigger positive β value means the neutral layer of the USSP-outer samples has shifted more outward. During the bending process, the deformation of the neutral layer is pure bending while the outer or inner region undergoes a nonuniform bending deformation to corporate the thinning or thickening of the sheet. A smaller β value means the thinning or thickening is smaller during the bending, which reduces the shear stress at the outer zone and result in a improved bending performance in USSP-inner 5 min sample.

Table 7.1. The modification of the thickness before and after bending

sample condition	before bending/mm	after bending/mm	β
as-received	2.65	2.71	0.023
both-5min	2.74	2.78	0.015
both-10min	2.56	2.61	0.020
both-15min	2.76	2.79	0.011
inner-5min	2.73	2.74	0.004
inner-10min	2.9	2.73	-0.059
inner-15min	2.76	2.43	-0.120
outer-5min	2.66	2.77	0.041
outer-10min	2.67	2.76	0.034
outer-15min	2.48	2.58	0.040

7.5 FEM simulation of the bending process

A two-dimensional model was developed to simulate the bending process of as-received and USSP treated AZ31 Mg alloy by ABAQUS software. The plasticity properties of the as-received and the USSP treated materials were obtained from the tension test result from chapter 4. For the USSP treated AZ31 Mg alloy, a gradient nano structure was set by the virtual temperature technique. A continuously variable temperature field was assigned and the one to one relationship between temperature and mechanical properties was created. The other thermal parameters, such as conductivity factor, were set as zero to ensure the temperature does not change during the bending process. By this method, the gradient mechanical properties at the top surface were achieved. According to the result in chapter 4, the thickness of the gradient nano structure

was set as 100 μm. The yield stress of the top surface nano layer was set as 500 MPa, according to the report by H. Chen et al. (2017). So the yield stress is set to linearly decrease from 500 MPa at the surface to 128 MPa at a depth of 100 μm. The load distance was set as 4mm, which was before the occurrence of a fracture during bending process, according to the load-stroke curves.

In figure 7.16, the simulation results of the equivalent plastic strain (PEEQ) and the mises stress are shown. For the as-received, the maximum mises stress is 2.32 e+2 MPa and the maximum PEEQ is 7.96 e-2. The maximum compression stress is located at the concave of the bending center, and the maximum tension stress is located at the convex. For PEEQ, the convex area shows the maximum value. For USSP-both, the maximum mises stress increases to 5.027 e+2 MPa. The maximum compression stress is still at the concave and the maximum tension at the convex. However, the distribution of the stress is more concentrated at the surface zone. For PEEQ, the maximum value is 8.947e-2, just a little bigger than the as-received. Meanwhile, the distribution of PEEQ is similar to that of as-received. The result implies that the USSP-both treatment enhances the required stress for bending while a high stress does not affect the strain distribution. The convex of the USSP-both undergoes a similar strain with that of as-received, and forms cracks as in as-received sample. The distributions of the asymmetric structure in Mg-inner and Mg-outer are quite different. For the USSP-inner, the maximum mises stress is 4.71 e+2 MPa and is located at the inner surface zone. The gradient nano structure at the inner zone would endure a high stress during the bending process, and results in multi-directional cracks. For PEEQ, it has the highest value of maximum PEEQ, 9.06e-2, among these four different states, and it is located at the convex. A higher value of maximum PEEQ at the outer surface zone leads to a higher risk of fracture during bending. The undergoing strain at the outer surface zone does not change. For USSP-outer, the maximum mises stress is 4.71 e+2 MPa, close to that of USSP-inner, but it is located at the outer surface zone. For PEEQ, the maximum value is 8.878e-2 and located at the inner surface zone. For the outer zone, the PEEQ value is just 5.00e-2. This means the gradient nano structure at the outer zone leads to a different deformation behavior during bending. The tension at the outer zone is restrained by this gradient nano structure and the inner zone was heavily

deformed. This deformation behavior is a benefit for the bending of Mg alloy because the compression in the inner zone is more easily deformed than the tension in the outer zone. In the inner zone, the $(10\bar{1}2)$ tension twin can be easily activated under a compression perpendicular to the c-axis. In the outer zone, the low Schmid facts of basal plane slip and $(10\bar{1}2)$ tension twin is low and the plastic deformation can be only coordinated by the non-basal plane slip. The deformation compatibility of the inner zone is much better. So this USSP-outer structure leads to a favorable deformation mechanism during bending.

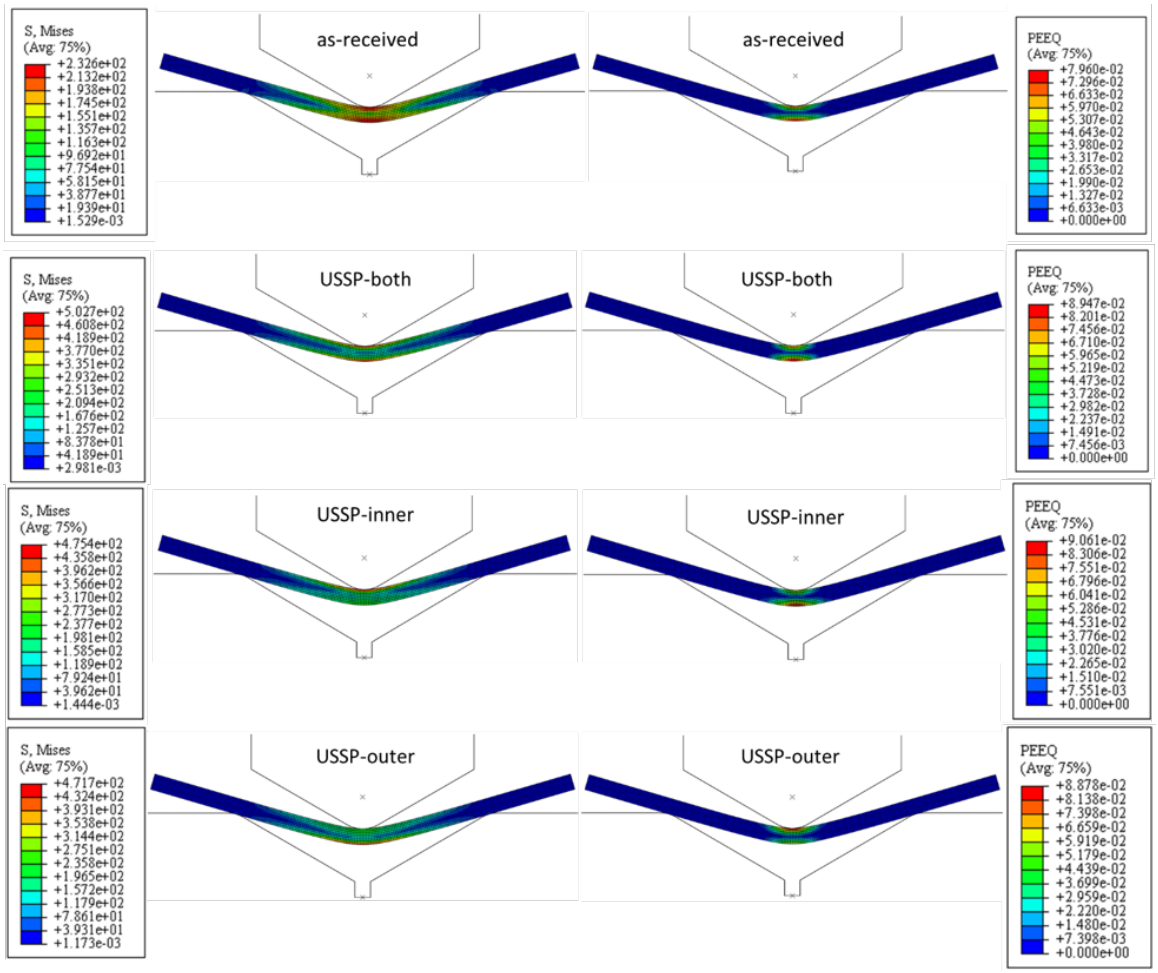

Figure 7.16. Finite element analysis of stress and strain of as-received, USSP-both, USSP-inner and USSP outer AZ31 Mg alloys after a load of 4 mm during the bending process

7.6 A quasi in-situ EBSD study: effect of USSP treated layer position on bending process

In order to better understand the effect of this asymmetric structure on the bending behavior, a quasi in-situ EBSD experiment was set up. A self-made in-situ EBSD holder for the V-bending process was prepared. The sample preparation was introduced in chapter 3. Three different states: as-received, USSP-inner and USSP-outer, were used to investigate the effect of placed position of gradient nano structure on the bending behavior. In this study, the samples of as-polished, bent at two load distances: 0.8mm and 1.6mm, were analyzed. The deformation modes and microstructure of the samples with three different states were observed from extrados to intrados, including the change of grain orientation, twins, and local stress distribution during the test and the shift of neutral layer.

Figure 7.17 shows the microstructure of the as-received AZ31 Mg alloy including the as-polished, bent at load distances of 0.8 mm and 1.6 mm. The as-polished sample shows a uniform and fine grains in figure 7.17(a). From the IPF maps, the initial grain orientation has a strong basal plane texture. Few twins are observed, and the twin fraction of tension twin is just 0.75% and compression twin of 0.1%.

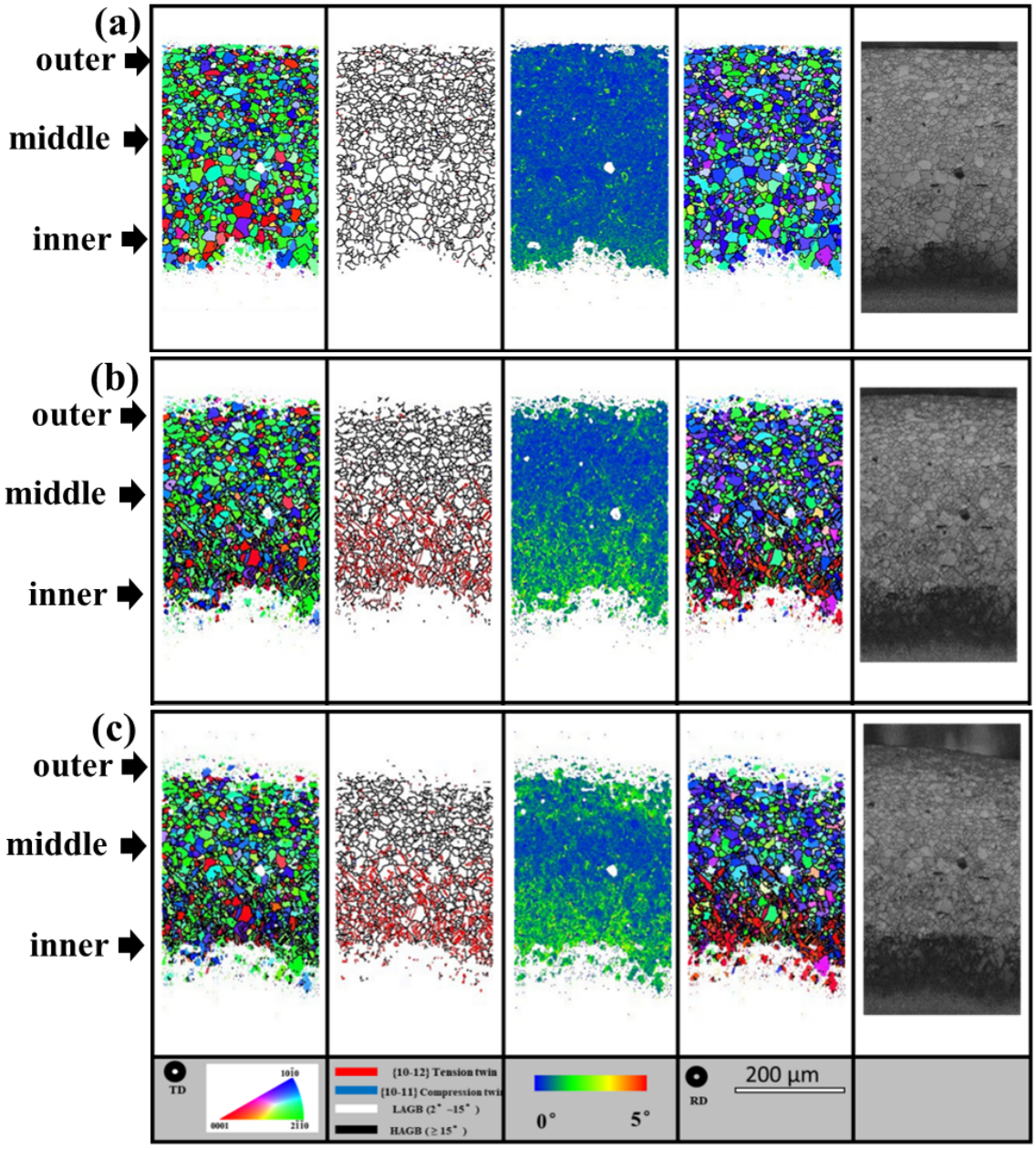

Figure 7.17. EBSD maps of the various positions: (a) as-polished, (b) after a load distance of 0.8mm and (c) after a load distance of 1.6mm of the as-received AZ31 Mg alloy sheet.

At the load distance of 0.8 mm in figure 7.17(b), at the outer zone, few twins are captured and some white areas, where the confident index value is lower than 0.3, appears. At larger strains, the quality of the Kikuchi patterns in in-situ EBSD experiment becomes lower and the part of the crystallographic information is lost. At the inner zone, a lot of

$(10\bar{1}2)$ tension twins are nucleated and growing in most grains, forming the twin bands. More white areas are captured in the intrados than in the extrados. Moreover, a grain rotation of c-axis from the ND to RD direction happens, leading to a drastic texture change. The twin bands extend to the center area, so the center area is also full of twins. The low-strain layer of the neutral zone is at the middle-upper part of the sample, which means the neutral layer has shifted towards the outer zone. From the KAM map, the strain gradient is present. The area under tension at the outer zone is smaller than the area under compression at the inner zone. The twin fraction of the tension twin increases to 14.9% and the compression is still 0.1%. The growing twins at the inner zone leads to the missed grain information in intrados. For the extrados, the possible deformation modes might be complex. The basal plane and the $(10\bar{1}2)$ tension twin are not active because of their low Schmid factors. The non-basal dislocation ships and the contraction twinning are the two possible deformation mechanism during bending. Here, the contraction twinning is not active at the extrados, so the non-basal dislocation is the only possible deformation mechanism.

For the sample at a further load distance to 1.6mm, shown in figure 7.17(c), the microstructure evolution after bending is similar. The outer zone under tension is dominant by dislocation slip while the inner zone under compression is dominant by twinning. No further extension of the twin bands is observed. The area fraction of $(10\bar{1}2)$ tension twin is 14.4% and the compression twin is still 0.1%. Also, the twin area in compression zone does not increase. The further increase of the load distance does not lead to a further shift of the neutral layer or the shift is quite limited. The slight decrease of tension twin fraction may be due to the increased fraction of white area. Some twinning area is placed by the white area that the crystallographic information is lost. In the outer zone, the $(10\bar{1}1)$ compression twin still cannot be active with the further increase of the loading distance. The compression twins can lead to a local softening and a favorable orientation for basal slip because its rotation of c-axis is 56^o. Here, still non-basal plane slip is the dominant mechanism, leading to a local stress concentration and surface hardening, seen in the KAM map.

The microstructural evolution of the USSP-inner sample during the bending process is present in figure 7.18. The as-polished shows a gradient nano structure at the inner surface zone while the rest of the sample is of uniform grains. The thickness of the gradient nanostructure is about 50 μm. A lot of $(10\bar{1}2)$ tension twins are found and the inner zone keeps the stain from the USSP process. Some areas at the inner zone are white because of the nano structure.

At a load distance of 0.8mm in figure 7.18(b), more tension twins at the inner zone are observed and the outer zone still has few twins, just like what is happened in the as-received. The white area appears at the extrados and the area at intrados grows. Compared with the as-received with a load distance of 0.8 mm, the twin band becomes more obvious than that in as-received while the tension twin fraction decreases a bit. The tension twin fraction is 12.0% and the compression twin is 0.1 %. Moreover, the white area at the outer zone is more than that of as-received. From the FEM simulation result, the gradient nano structure at the inner side leads a higher stress at the inner zone during bending process. The higher stress may lead to a quicker growing and extension of the twin band, forming a longer and wider twin band. Meanwhile, the stress of USSP-inner is more concentrated, so the twinning area is less. That may be why the twin fraction is 12.0 %. The thickness of the white area at both inner and outer sides are increased, compared with that of as-received with the same load distance, especially the outer side. The contraction twinning is still not active at the extrados, and the non-basal dislocation is the only possible deformation mechanism.

At a load distance of 1.6mm in figure 7.18(c), the microstructure evolution is still presenting a gradient change. The outer zone is under tension and the inner zone is under compression. The fraction of the $(10\bar{1}2)$ tension twin is 11.1% and the compression twin is 0.1%. The white area is thickening during the further load. The changing tendency in the USSP-inner is the same as the as-received. During the further loading, the twin fraction decreases, and the white area increases. The difference is there is more white area in the USSP-inner than in the as-received. The gradient nano structure at the inner side results in an increase strain at the extrados during the bending. The result is consistent with the FEM simulation result.

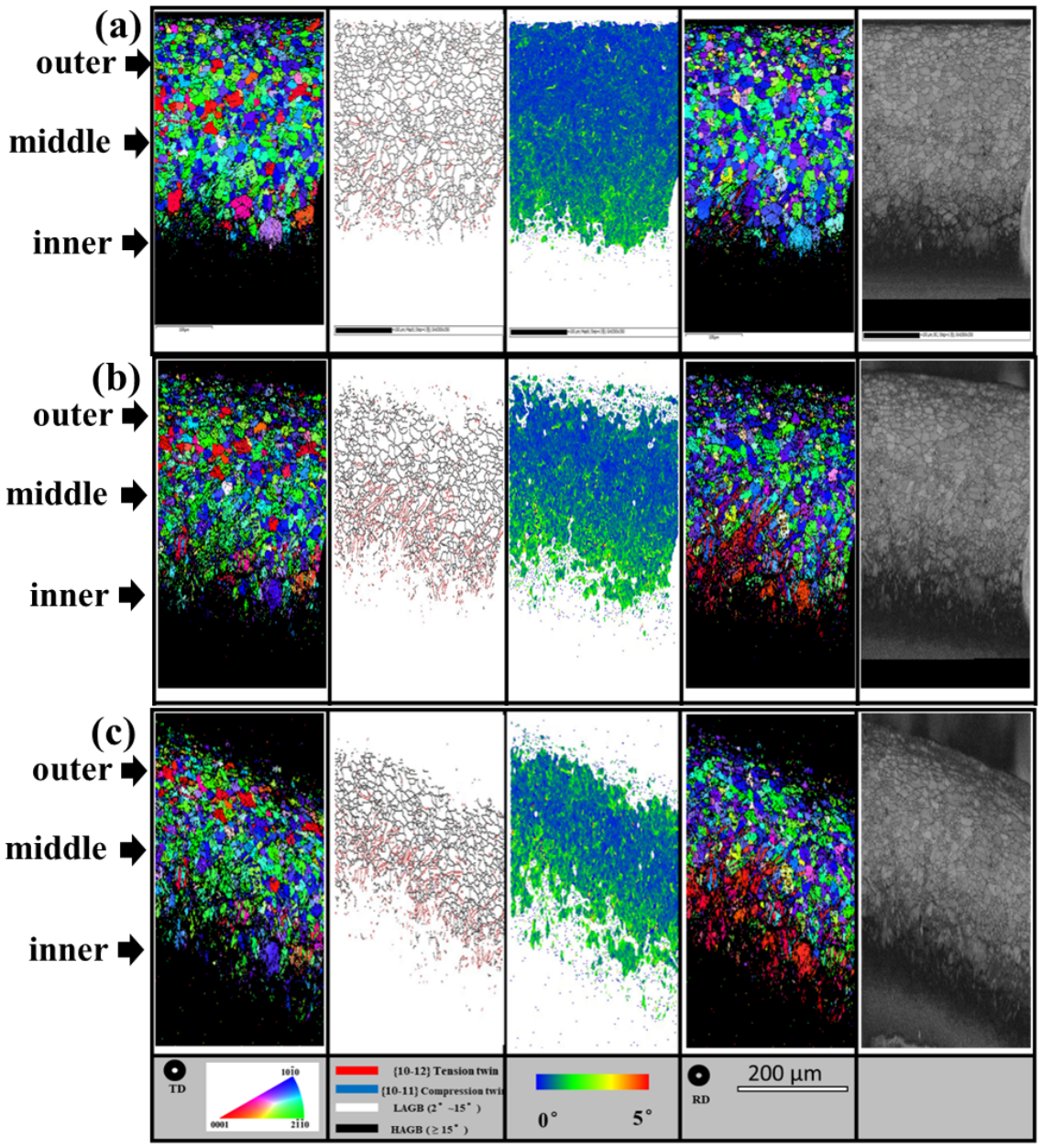

Figure 7.18. EBSD maps of the various positions: (a) as-polished, (b) after a load distance of 0.8mm and (c) after a load distance of 1.6mm of the USSP-inner AZ31 Mg alloy sheet

Similar to the gradient microstructure evolution in as-received and USSP-inner samples, the effect of gradient nano structure at the outer side on the microstructure evolution during the bending are also recorded and compared, shown in figure 7.19. The as-polished USSP-outer shows a gradient nano structure at the outer surface zone and the grains in the untreated area is uniform with a basal plane texture.

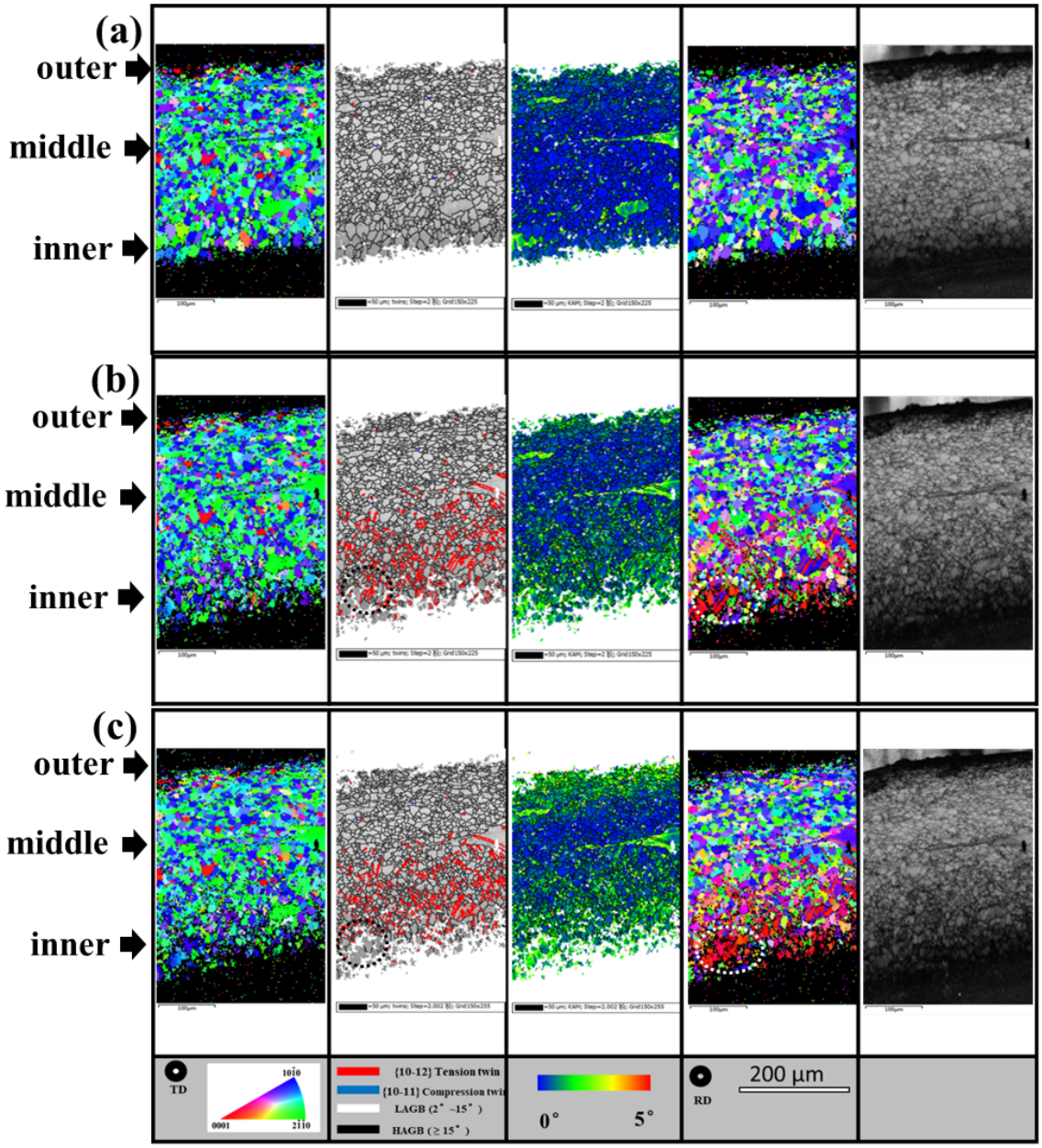

Figure 7.19. EBSD maps of the various positions: (a) as-polished, (b) after a load distance of 0.8mm and (c) after a load distance of 1.6mm of the USSP-outer AZ31 Mg alloy sheet

Figure 7.19(b) shows the microstructure of USSP-outer after bending deformation at a load distance of 0.8 mm. The microstructure evolution in figure 7.19(b) illustrates that the similar deformation at the USSP-outer sample, where the inner zone is dominated by the twinning while the outer zone is dominated by the dislocation slips. The tension twin fraction is 12.5% and the compression twin is still just 0.1%. Twinning bands occurs and grows across the center line. The neutral layer has shifted towards the outer side.

Figure 7.19(c) shows the microstructural evolution of USSP-outer at a load distance of 1.6mm. The tension twin fraction is 11.8% and the compression twin is 0.1%. The disappearing of the tension twins is observed, which is highlighted by the white dash line circle in the IPF map from the RD direction and the black circle in the grain boundary map. The further bending leads to a further shift of the grains c-axis in the grains at the circle. After the whole grain has shifted from the ND to RD, the twins disappear, and the grain becomes totally red in the IPF map from the RD direction. It should be mentioned that the twin disappearing phenomena happens next to the white area. So it can be implied that the twin fraction during the bending process will increase firstly, reach a peak value, then decrease with further loading. The white area at the inner zone increases after this further bending. From the KAM map, both the inner surface area and the outer surface area suffer a lot of strain. What is different from the USSP-inner and as-received is the white area at the outer zone does not increase, compared with that at the load distance of 0.8mm. The result is the evidence that the outer surface zone will undergo a less serious plastic deformation after placing the gradient nano structure at the outer zone.

7.7 Summary

In this chapter, a three-point V-bending experimental investigation has been conducted to study the bending behavior of the as-received, USSP-both, USSP-inner and USSP-outer four samples. The microstructure evolution during the bending process was investigated by the EBSD analysis. A simple FEM simulation was employed to show the stress and strain distribution during the bending process. A quasi in-situ EBSD experiment was also used to study the microstructure and deformation mechanism during bending. The major conclusions from the experimental and simulation results are summarized as follows:

The bendability of the as-rolled AZ31 Mg alloy with a thickness of 3 mm was poor, and the fracture happened at a load distance of $\sim$ 4.5 mm.

During the bending, the inner zone was under compression while the outer zone was under tension. The plastic deformation at the inner zone was dominated by the twinning while the outer zone was dominated by the dislocation slips. The different deformation mechanisms at the inner and outer zone leaded to the shift of neutral layer towards outer zone during bending.

The twinning at the inner zone resulted in the shift of c-axis from ND to RD.

The USSP treatment at both zones led to a higher value of load stress and had almost a similar bendability of as-received even though the ductility of the USSP-both sample was reduced.

The USSP treatment at the inner side for 5 min improved the bendability and longer treatments of 10 min and 15min degenerated the bendability to as-received. The improved bendability of the 5 min treated sample was due to the drawing back of the neutral layer to the middle position.

The USSP treatment at the outer side for 5 min could improve the bendability a bit and longer treatment of 15 min enhanced the bendability, obviously. The obviously improved bendability of the 15 min sample was due to its asymmetric structure, resulting in a smaller strain at the convex.

The tension twin fraction during the bending process increased firstly, reach a peak value, then decrease with further loading.

CHAPTER 8. CONCLUSIONS

In the current research, the studies on the microstructural evolution (grain size, twinning structure, surface roughness, etc.) during the ultrasonic shot peening process of AZ31 Mg alloy, as well as the effect of formed surface nanocrystalline on the mechanical properties (microhardness, mechanical stress, wear resistance and bending performance) and corrosion resistance have been conducted. The results indicates that a gradient nano structure formed at the top surface after treatment. One of the research focuses in this study is how the formed nanocrystalline affect the mechanical properties of AZ31 Mg alloys. Another focus of this study is how the modified mechanical properties change the wear resistance and bending performance, to see if the ultrasonic shot peening treatment can improve the service performance and widen the application of Mg alloys. In addition, the influence of surface nanocrystalline on the corrosion resistance of AZ31 Mg alloy was also carried out to investigate the corrosion mechanism of refined grain structure. Major conclusions of this research are listed as follows:

• A gradient nanostructure was achieved at the top surface after the ultrasonic shot peening process. The grain at the top surface was refined to 45nm after 5 min USSP treatment, and further refined to 42 nm and 37nm for 10 min and 15 min treatments, respectively. A lamellar nanocrystalline was below the top surface along the depth. $(10\bar{1}2)$ tensile twins were found at the heavily deformed grains below the nanocrystalline layer. The untwined matrix still underwent a deformed strain.

• The microhardness of the USSP treated samples was increased greatly compared to the as-received sample. The microhardness was increased from 65 HV of the as-received sample to 123 HV, 127HV and 143 HV of USSP 5min, 10 min and 15 min samples, respectively. The improved microhardness was attributed to the grain refinement, the work hardening and the residual stress.

• The tensile stress and compression stress were improved remarkably after USSP treatment while the elongation was sacrificed. The yield stress was improved from 127.7 MPa to 198 MPa after a 10 min USSP treatment. The improved mechanical stress was attributed to the grain refinement and the work hardening.

• The wear resistance of AZ31 Mg alloy was improved after USSP treatment. The coefficient of friction and the wear rate of AZ31 Mg alloy becomes lower after USSP treatment. The widths of the wear track of the USSP treated sample is much narrower than that of as-received. The worn surface of USSP treated surface has a lower surface roughness. The formed surface nanocrystalline led to the transition boundary between the mild wear and severe wear to a higher sliding speed and higher applied load.

• The corrosion resistance of AZ31 Mg alloy was significantly reduced after USSP treatment in 3.5 wt.% NaCl solution because of the Fe particles at the top surface of the USSP treated sample, which were exfoliated from the shot during the USSP treating process.

• A 40 μm polishing of USSP sample improved the corrosion resistance greatly. The corrosion rate was half of the as-received. 80 μm and 100 μm polished samples also showed a lower corrosion rate than that of as-received but a slightly increase compared to the 40 μm polished . The improved corrosion resistance of the 40-100 μm polished samples was due to the reduced current density of the anodic reaction during the immersion. From the corrosion morphology after 7 days' immersion, the grain boundary could protect the matrix and acted as a corrosion barrier. The massive amount of grain boundary in the nanocrystalline improved the corrosion resistance of Mg alloys and resulted in a uniform corrosion morphology.

• The bendability of the as-rolled AZ31 Mg alloy with a thickness of 3 mm was limited, and a fracture happened at a load distance of 4.5 mm. The USSP treatment at both sides led to a higher value of load stress and had a similar bendability of as-received even though the ductility of USSP treated sample was reduced greatly.

• The USSP treatment at the inner side for 5 min could improve the bendability and longer treatments of 10 min and 15 min degenerated the bendability to as-received. The improved bendability of 5 min treated samples was due to the drawing back of the neutral layer to the middle and reduced the shear stress. The USSP treatment at the outer side for 5 min could improve the bendability a bit and a longer treatment of 15 min enhanced the bendability, obviously. The obvious improved bendability of 15 min samples was due to its asymmetric structure, resulting in a smaller strain at the convex.

REFERENCES

Agnew, S. R., & Duygulu, Ö. (2005). Plastic anisotropy and the role of non-basal slip in magnesium alloy az31b. *International Journal of plasticity*, *21*(6), 1161–1193.

Ahmadkhaniha, D., Huang, Y., Jaskari, M., Järvenpää, A., Sohi, M. H., Zanella, C., … Langdon, T. G. (2018). Effect of high-pressure torsion on microstructure, mechanical properties and corrosion resistance of cast pure mg. *Journal of materials science*, *53*(24), 16585–16597.

Amanov, A., Penkov, O. V., Pyun, Y.-S., & Kim, D.-E. (2012). Effects of ultrasonic nanocrystalline surface modification on the tribological properties of az91d magnesium alloy. *Tribology International*, *54*, 106–113.

An, J., Li, R., Lu, Y., Chen, C., Xu, Y., Chen, X., & Wang, L. (2008). Dry sliding wear behavior of magnesium alloys. *Wear*, *265*(1-2), 97–104.

Archard, J., & Hirst, W. (1956). The wear of metals under unlubricated conditions. *Proceedings of the Royal Society of London. Series A. Mathematical and Physical Sciences*, *236*(1206), 397–410.

Atrens, A., Liu, M., & Abidin, N. I. Z. (2011). Corrosion mechanism applicable to biodegradable magnesium implants. *Materials Science and Engineering: B*, *176*(20), 1609–1636.

Atrens, A., Song, G.-L., Cao, F., Shi, Z., & Bowen, P. K. (2013). Advances in mg corrosion and research suggestions. *Journal of Magnesium and Alloys*, *1*(3), 177–200.

Aung, N. N., & Zhou, W. (2010). Effect of grain size and twins on corrosion behaviour of az31b magnesium alloy. *Corrosion Science*, *52*(2), 589–594.

Aung, N. N., Zhou, W., & Lim, L. E. (2008). Wear behaviour of az91d alloy at low sliding speeds. *Wear*, *265*(5-6), 780–786.

Azadmanjiri, J., Berndt, C. C., Kapoor, A., & Wen, C. (2015). Development of surface nano-crystallization in alloys by surface mechanical attrition treatment (smat). *Critical Reviews in Solid State and Materials Sciences*, *40*(3), 164–181.

Barnett, M. (2007). Twinning and the ductility of magnesium alloys: Part i:tension twins. *Materials Science and Engineering: A*, *464*(1-2), 1–7.

Bian, M. Z., & Shin, K. S. (2013). twinning behavior in magnesium single crystal. *Metals and Materials International*, *19*(5), 999–1004.

Birbilis, N., Ralston, K., Virtanen, S., Fraser, H., & Davies, C. (2010). Grain character influences on corrosion of ecaped pure magnesium. *Corrosion Engineering, Science and Technology*, *45*(3), 224–230.

Cao, F., Shi, Z., Hofstetter, J., Uggowitzer, P. J., Song, G., Liu, M., & Atrens, A. (2013). Corrosion of ultra-high-purity mg in 3.5% nacl solution saturated with mg (oh) 2. *Corrosion science*, *75*, 78–99.

Chan, H., Ruan, H., Chen, A., & Lu, J. (2010). Optimization of the strain rate to achieve exceptional mechanical properties of 304 stainless steel using high speed ultrasonic surface mechanical attrition treatment. *Acta Materialia*, *58*(15), 5086–5096.

Chang, Y.-Y., Wang, D.-Y., Chang, C.-H., & Wu, W. (2004). Tribological analysis of nano-composite diamond-like carbon films deposited by unbalanced magnetron sputtering. *Surface and Coatings Technology*, *184*(2-3), 349–355.

Chegini, M., Fallahi, A., & Shaeri, M. (2015). Effect of equal channel angular pressing (ecap) on wear behavior of al-7075 alloy. *Procedia Materials Science*, *11*, 95–100.

Chen, H., & Alpas, A. (2000). Sliding wear map for the magnesium alloy mg-9al-0.9 zn (az91). *Wear*, *246*(1-2), 106–116.

Chen, H., Yang, J., Zhou, H., Moering, J., Yin, Z., Gong, Y., & Zhao, K. (2017). Mechanical properties of gradient structure mg alloy. *Metallurgical and Materials Transactions A*, *48*(9), 3961–3970.

Chen, X., Han, Z., & Lu, K. (2018). Friction and wear reduction in copper with a gradient nano-grained surface layer. *ACS applied materials & interfaces*, *10*(16), 13829–13838.

Chen, Y., Wang, Q., Peng, J., Zhai, C., & Ding, W. (2007). Effects of extrusion ratio on the microstructure and mechanical properties of az31 mg alloy. *Journal of materials processing technology*, *182*(1-3), 281–285.

Denkena, B., & Lucas, A. (2007). Biocompatible magnesium alloys as absorbable implant materials–adjusted surface and subsurface properties by machining processes. *CIRP annals*, *56*(1), 113–116.

Dey, A., & Pandey, K. M. (2018). Wear behaviour of mg alloys and their composites–a review. *International Journal of Materials Research*, *109*(11), 1050–1070.

Easton, M., Beer, A., Barnett, M., Davies, C., Dunlop, G., Durandet, Y., … Beggs, P. (2008). Magnesium alloy applications in automotive structures. *Jom*, *60*(11), 57.

Edalati, K., Ashida, M., Horita, Z., Matsui, T., & Kato, H. (2014). Wear resistance and tribological features of pure aluminum and al–al2o3 composites consolidated by high-pressure torsion. *Wear*, *310*(1-2), 83–89.

El Aal, M. I. A., El Mahallawy, N., Shehata, F. A., El Hameed, M. A., Yoon, E. Y., & Kim, H. S. (2010). Wear properties of ecap-processed ultrafine grained al–cu alloys. *Materials Science and Engineering: A*, *527*(16-17), 3726–3732.

Esmaily, M., Svensson, J., Fajardo, S., Birbilis, N., Frankel, G., Virtanen, S., … Johansson, L. (2017). Fundamentals and advances in magnesium alloy corrosion. *Progress in Materials Science*, *89*, 92–193.

Farhat, Z., Ding, Y., Northwood, D., & Alpas, A. (1996). Effect of grain size on friction and wear of nanocrystalline aluminum. *Materials Science and Engineering: A*, *206*(2), 302–313.

Gao, J., Guan, S., Ren, Z., Sun, Y., Zhu, S., & Wang, B. (2011). Homogeneous corrosion of high pressure torsion treated mg–zn–ca alloy in simulated body fluid. *Materials Letters*, *65*(4), 691–693.

Ge, M.-Z., Xiang, J.-Y., Tang, Y., Ye, X., Fan, Z., Lu, Y., & Zhang, X. (2018). Wear behavior of mg-3al-1zn alloy subjected to laser shock peening. *Surface and Coatings Technology*, *337*, 501–509.

Gopi, K. R., & Nayaka, H. S. (2017). Tribological and corrosion properties of am70 magnesium alloy processed by equal channel angular pressing. *Journal of Materials Research*, *32*(11), 2153–2160.

Gusieva, K., Davies, C., Scully, J., & Birbilis, N. (2015). Corrosion of magnesium alloys: the role of alloying. *International Materials Reviews*, *60*(3), 169–194.

Hagihara, K., Okubo, M., Yamasaki, M., & Nakano, T. (2016). Crystal-orientation-dependent corrosion behaviour of single crystals of a pure mg and mg-al and mg-cu solid solutions. *Corrosion Science*, *109*, 68–85.

Hakamada, M., Furuta, T., Chino, Y., Chen, Y., Kusuda, H., & Mabuchi, M. (2007). Life cycle inventory study on magnesium alloy substitution in vehicles. *Energy*, *32*(8), 1352–1360.

Han, Y., Zhang, L., Lu, J., & Zhang, W. (2009). Thermal stability and corrosion resistance of nanocrystallized zirconium formed by surface mechanical attrition treatment. *Journal of materials research*, *24*(10), 3136–3145.

He, J., Jiang, B., Zhang, J., Xiang, Q., Xia, X., & Pan, F. (2015). Enhancement of mechanical properties and corrosion resistance of magnesium alloy sheet by pre-straining and annealing. *Materials Science and Engineering: A*, *647*, 216–221.

Hirsch, J. (2011). Aluminium in innovative light-weight car design. *Materials Transactions*, *52*(5), 818–824.

Holmberg, K., Andersson, P., & Erdemir, A. (2012). Global energy consumption due to friction in passenger cars. *Tribology International*, *47*, 221–234.

Horner, D., Connolly, B., Zhou, S., Crocker, L., & Turnbull, A. (2011). Novel images of the evolution of stress corrosion cracks from corrosion pits. *Corrosion Science*, *53*(11), 3466–3485.

Hort, N., Huang, Y., Fechner, D., Störmer, M., Blawert, C., Witte, F., ... others (2010). Magnesium alloys as implant materials–principles of property design for mg–re alloys. *Acta biomaterialia*, *6*(5), 1714–1725.

Hu, T., Xin, Y., Wu, S., Chu, C., Lu, J., Guan, L., ... Chu, P. K. (2011). Corrosion behavior on orthopedic niti alloy with nanocrystalline/amorphous surface. *Materials Chemistry and Physics*, *126*(1-2), 102–107.

Huang, R., & Han, Y. (2013). The effect of smat-induced grain refinement and dislocations on the corrosion behavior of ti–25nb–3mo–3zr–2sn alloy. *Materials Science and Engineering: C*, *33*(4), 2353–2359.

Hull, D., & Clyne, T. W. (1996). *An introduction to composite materials*. Cambridge university press.

Ivasishin, O. M., Anokhin, V., Demidik, A., & Savvakin, D. G. (2000). Cost-effective blended elemental powder metallurgy of titanium alloys for transportation application. In *Key engineering materials* (Vol. 188, pp. 55–62).

Jelliti, S., Richard, C., Retraint, D., Roland, T., Chemkhi, M., & Demangel, C. (2013). Effect of surface nanocrystallization on the corrosion behavior of ti–6al–4v titanium alloy. *Surface and Coatings technology*, *224*, 82–87.

Kramer, D. A. (2000). Magnesium and magnesium alloys. *Kirk-Othmer Encyclopedia of Chemical Technology*, 1–55.

Kumar, S., Rao, G. S., Chattopadhyay, K., Mahobia, G., Srinivas, N. S., & Singh, V. (2014). Effect of surface nanostructure on tensile behavior of superalloy in718. *Materials & Design (1980-2015)*, *62*, 76–82.

Laleh, M., & Kargar, F. (2011). Effect of surface nanocrystallization on the microstructural and corrosion characteristics of az91d magnesium alloy. *Journal of Alloys and Compounds*, *509*(37), 9150–9156.

Lee, H.-s., Kim, D.-s., Jung, J.-s., Pyoun, Y.-s., & Shin, K. (2009). Influence of peening on the corrosion properties of aisi 304 stainless steel. *Corrosion science*, *51*(12), 2826–2830.

Lei, J., Cui, W.-f., Xiu, S., Gang, L., & Lian, Z. (2014). Effects of surface nanocrystallization on corrosion resistance of β-type titanium alloy. *Transactions of Nonferrous Metals Society of China*, *24*(8), 2529–2535.

Lesuer, D. R., & Kipouros, G. J. (1995). Lightweight materials for transportation applications. *JOM Journal of the Minerals, Metals and Materials Society*, *47*(7), 17–17.

Li, J., Chen, S., Wu, X., Soh, A., & Lu, J. (2010). The main factor influencing the tensile properties of surface nano-crystallized graded materials. *Materials Science and Engineering: A*, *527*(26), 7040–7044.

Li, N., Li, Y., Li, Y., Wu, Y., Zheng, Y., & Han, Y. (2014). Effect of surface mechanical attrition treatment on biodegradable mg–1ca alloy. *Materials Science and Engineering: C*, *35*, 314–321.

Li, Y., Wang, F., & Liu, G. (2004). Grain size effect on the electrochemical corrosion behavior of surface nanocrystallized low-carbon steel. *Corrosion*, *60*(10), 891–896.

Liu, G., Lu, J., & Lu, K. (2000). Surface nanocrystallization of 316l stainless steel induced by ultrasonic shot peening. *Materials Science and Engineering: A*, *286*(1), 91–95.

Liu, H., Chen, Y., Tang, Y., Wei, S., & Niu, G. (2007). The microstructure, tensile properties, and creep behavior of as-cast mg–(1–10)% sn alloys. *Journal of Alloys and Compounds*, *440*(1-2), 122–126.

Liu, M., Qiu, D., Zhao, M.-C., Song, G., & Atrens, A. (2008). The effect of crystallographic orientation on the active corrosion of pure magnesium. *Scripta Materialia*, *58*(5), 421–424.

Liu, Y., Jin, B., Li, D.-J., Zeng, X.-Q., & Lu, J. (2015). Wear behavior of nanocrystalline structured magnesium alloy induced by surface mechanical attrition treatment. *Surface and Coatings Technology*, *261*, 219–226.

Liu, Y., Jin, B., & Lu, J. (2015). Mechanical properties and thermal stability of nanocrystallized pure aluminum produced by surface mechanical attrition treatment. *Materials Science and Engineering: A*, *636*, 446–451.

Lu, K., & Lu, J. (2004). Nanostructured surface layer on metallic materials induced by surface mechanical attrition treatment. *Materials Science and Engineering: A*, *375*, 38–45.

Luo, A., & Pekguleryuz, M. (1994). Cast magnesium alloys for elevated temperature applications. *Journal of materials science*, *29*(20), 5259–5271.

Luo, A. A. (2013). Magnesium casting technology for structural applications. *journal of Magnesium and Alloys*, *1*(1), 2–22.

Makar, G., & Kruger, J. (1993). Corrosion of magnesium. *International materials reviews*, *38*(3), 138–153.

Matsubara, K., Miyahara, Y., Horita, Z., & Langdon, T. (2003). Developing superplasticity in a magnesium alloy through a combination of extrusion and ecap. *Acta materialia*, *51*(11), 3073–3084.

McCall, C., Hill, M., & Lillard, R. (2005). Crystallographic pitting in magnesium single crystals. *Corrosion engineering, science and technology*, *40*(4), 337–343.

Meng, X., Duan, M., Luo, L., Zhan, D., Jin, B., Jin, Y., … Lu, J. (2017). The deformation behavior of az31 mg alloy with surface mechanical attrition treatment. *Materials Science and Engineering: A*, *707*, 636–646.

Moon, J. H., Baek, S. M., Lee, S. G., Seong, Y., Amanov, A., Lee, S., & Kim, H. S. (2019). Effects of residual stress on the mechanical properties of copper processed using ultrasonic-nanocrystalline surface modification. *Materials Research Letters*, *7*(3), 97–102.

Mordike, B., & Ebert, T. (2001). Magnesium: propertiesapplicationspotential. *Materials Science and Engineering: A*, *302*(1), 37–45.

Mordyuk, B., Prokopenko, G., Vasylyev, M., & Iefimov, M. (2007). Effect of structure evolution induced by ultrasonic peening on the corrosion behavior of aisi-321 stainless steel. *Materials Science and Engineering: A*, *458*(1-2), 253–261.

Müller, W. D., Nascimento, M. L., Zeddies, M., Córsico, M., Gassa, L. M., & Mele, M. A. F. L. d. (2007). Magnesium and its alloys as degradable biomaterials: corrosion studies using potentiodynamic and eis electrochemical techniques. *Materials Research*, *10*(1), 5–10.

Pawar, S., Slater, T., Burnett, T., Zhou, X., Scamans, G., Fan, Z., ... Withers, P. (2017). Crystallographic effects on the corrosion of twin roll cast az31 mg alloy sheet. *Acta Materialia*, *133*, 90–99.

Pérez-Prado, M. T., Del Valle, J., Contreras, J., & Ruano, O. A. (2004). Microstructural evolution during large strain hot rolling of an am60 mg alloy. *Scripta Materialia*, *50*(5), 661–665.

Pollock, T. M. (2010). Weight loss with magnesium alloys. *Science*, *328*(5981), 986–987.

Pu, Z., Song, G.-L., Yang, S., Outeiro, J., Dillon Jr, O., Puleo, D., & Jawahir, I. (2012). Grain refined and basal textured surface produced by burnishing for improved corrosion performance of az31b mg alloy. *Corrosion Science*, *57*, 192–201.

Pu, Z., Yang, S., Song, G.-L., Dillon Jr, O., Puleo, D., & Jawahir, I. (2011). Ultrafine-grained surface layer on mg–al–zn alloy produced by cryogenic burnishing for enhanced corrosion resistance. *Scripta Materialia*, *65*(6), 520–523.

Qi, Q.-j., Liu, Y.-B., & Yang, X.-H. (2003). Effects of rare earths on friction and wear characteristics of magnesium alloy az91d. *TRANSACTIONS-NONFERROUS METALS SOCIETY OF CHINA-ENGLISH EDITION-*, *13*(1), 111–115.

Rakita, M., Wang, M., Han, Q., Liu, Y., & Yin, F. (2013). Ultrasonic shot peening. *International Journal of Computational Materials Science and Surface Engineering*, *5*(3), 189–209.

Ralston, K., Fabijanic, D., & Birbilis, N. (2011). Effect of grain size on corrosion of high purity aluminium. *Electrochimica Acta*, *56*(4), 1729–1736.

Revie, R. W. (2008). *Corrosion and corrosion control: an introduction to corrosion science and engineering*. John Wiley & Sons.

Robson, J., Stanford, N., & Barnett, M. (2011). Effect of precipitate shape on slip and twinning in magnesium alloys. *Acta materialia*, *59*(5), 1945–1956.

Rupert, T. J., & Schuh, C. A. (2010). Sliding wear of nanocrystalline ni–w: Structural evolution and the apparent breakdown of archard scaling. *Acta Materialia*, *58*(12), 4137–4148.

Seenuvasaperumal, P., Doi, K., Basha, D. A., Singh, A., Elayaperumal, A., & Tsuchiya, K. (2018). Wear behavior of hpt processed ufg az31b magnesium alloy. *Materials Letters*, *227*, 194–198.

Shanthi, M., Lim, C., & Lu, L. (2007). Effects of grain size on the wear of recycled az91 mg. *Tribology international*, *40*(2), 335–338.

Shi, X., Liu, Y., Li, D., Chen, B., Zeng, X., Lu, J., & Ding, W. (2015). Microstructure evolution and mechanical properties of an mg–gd alloy subjected to surface mechanical attrition treatment. *Materials Science and Engineering: A*, *630*, 146–154.

Singh, I., Singh, M., & Das, S. (2015). A comparative corrosion behavior of mg, az31 and az91 alloys in 3.5% nacl solution. *Journal of Magnesium and Alloys*, *3*(2), 142–148.

So, H. (1995). The mechanism of oxidational wear. *Wear*, *184*(2), 161–167.

Song, G., & Atrens, A. (2003). Understanding magnesium corrosiona framework for improved alloy performance. *Advanced engineering materials*, *5*(12), 837–858.

Song, G., Atrens, A., St John, D., Wu, X., & Nairn, J. (1997). The anodic dissolution of magnesium in chloride and sulphate solutions. *Corrosion Science*, *39*(10-11), 1981–2004.

Song, G.-L., Mishra, R., & Xu, Z. (2010). Crystallographic orientation and electrochemical activity of az31 mg alloy. *Electrochemistry Communications*, *12*(8), 1009–1012.

Song, G.-L., & Xu, Z. (2012). Effect of microstructure evolution on corrosion of different crystal surfaces of az31 mg alloy in a chloride containing solution. *Corrosion Science*, *54*, 97–105.

Stanford, N., & Barnett, M. R. (2008). The origin of rare earth texture development in extruded mg-based alloys and its effect on tensile ductility. *Materials Science and Engineering: A*, *496*(1-2), 399–408.

Styczynski, A., Hartig, C., Bohlen, J., & Letzig, D. (2004). Cold rolling textures in az31 wrought magnesium alloy. *Scripta Materialia*, *50*(7), 943–947.

Sun, H., Shi, Y.-N., & Zhang, M.-X. (2008). Wear behaviour of az91d magnesium alloy with a nanocrystalline surface layer. *Surface and Coatings Technology*, *202*(13), 2859–2864.

Sun, H., Shi, Y.-N., Zhang, M.-X., & Lu, K. (2007). Plastic strain-induced grain refinement in the nanometer scale in a mg alloy. *Acta Materialia*, *55*(3), 975–982.

Sun, Q., Han, Q., Liu, X., Xu, W., & Li, J. (2017). The effect of surface contamination on corrosion performance of ultrasonic shot peened 7150 al alloy. *Surface and Coatings Technology*, *328*, 469–479.

Taltavull, C., Torres, B., Lopez, A., & Rams, J. (2013). Dry sliding wear behavior of am60b magnesium alloy. *Wear*, *301*(1-2), 615–625.

Tao, N., Sui, M., Lu, J., & Lua, K. (1999). Surface nanocrystallization of iron induced by ultrasonic shot peening. *Nanostructured Materials*, *11*(4), 433–440.

Thomas, S., Medhekar, N., Frankel, G., & Birbilis, N. (2015). Corrosion mechanism and hydrogen evolution on mg. *Current Opinion in Solid State and Materials Science*, *19*(2), 85–94.

Tian, J., Dai, K., Villegas, J., Shaw, L., Liaw, P., Klarstrom, D., & Ortiz, A. (2008). Tensile properties of a nickel-base alloy subjected to surface severe plastic deformation. *Materials Science and Engineering: A*, *493*(1-2), 176–183.

Valiev, R. Z., Estrin, Y., Horita, Z., Langdon, T. G., Zechetbauer, M. J., & Zhu, Y. T. (2006). Producing bulk ultrafine-grained materials by severe plastic deformation. *Jom*, *58*(4), 33–39.

Valiev, R. Z., Estrin, Y., Horita, Z., Langdon, T. G., Zehetbauer, M. J., & Zhu, Y. (2016). Producing bulk ultrafine-grained materials by severe plastic deformation: ten years later. *Jom*, *68*(4), 1216–1226.

Villegas, J. C., Dai, K., Shaw, L. L., & Liaw, P. K. (2005). Nanocrystallization of a nickel alloy subjected to surface severe plastic deformation. *Materials Science and Engineering: A*, *410*, 257–260.

Vinarcik, E. J. (2002). *High integrity die casting processes*. John Wiley & Sons.

Wang, A., Venkataraman, S., Alspaugh, S., Katz, R., & Stoica, I. (2012). Cake: enabling high-level slos on shared storage systems. In *Proceedings of the third acm symposium on cloud computing* (p. 14).

Wang, B., Guan, S., Wang, J., Wang, L., & Zhu, S. (2011). Effects of nd on microstructures and properties of extruded mg–2zn–0.46 y–xnd alloys for stent application. *Materials Science and Engineering: B*, *176*(20), 1673–1678.

Wang, K., Tao, N., Liu, G., Lu, J., & Lu, K. (2006). Plastic strain-induced grain refinement at the nanometer scale in copper. *Acta Materialia*, *54*(19), 5281–5291.

Wang, Q., Jiang, B., Chai, Y., Liu, B., Ma, S., Xu, J., & Pan, F. (2016). Tailoring the textures and mechanical properties of az31 alloy sheets using asymmetric composite extrusion. *Materials Science and Engineering: A*, *673*, 606–615.

Wang, S., Yang, Z., Zhao, Y., & Wei, M. (2010). Sliding wear characteristics of az91d alloy at ambient temperatures of 25–200 c. *Tribology letters*, *38*(1), 39–45.

Wang, X., & Li, D. (2002). Mechanical and electrochemical behavior of nanocrystalline surface of 304 stainless steel. *Electrochimica Acta*, *47*(24), 3939–3947.

Wang, X., Liu, Z., Dai, W., & Han, Q. (2015). On the understanding of aluminum grain refinement by al-ti-b type master alloys. *Metallurgical and Materials Transactions B*, *46*(4), 1620–1625.

Wen, M., Liu, G., Gu, J.-f., Guan, W.-m., & Lu, J. (2008). The tensile properties of titanium processed by surface mechanical attrition treatment. *Surface and Coatings Technology*, *202*(19), 4728–4733.

Wu, X., Jiang, P., Chen, L., Yuan, F., & Zhu, Y. T. (2014). Extraordinary strain hardening by gradient structure. *Proceedings of the National Academy of Sciences*, *111*(20), 7197–7201.

Wu, X., Tao, N., Hong, Y., Xu, B., Lu, J., & Lu, K. (2002). Microstructure and evolution of mechanically-induced ultrafine grain in surface layer of al-alloy subjected to ussp. *Acta materialia*, *50*(8), 2075–2084.

Xia, S., Liu, Y., Fu, D., Jin, B., & Lu, J. (2016). Effect of surface mechanical attrition treatment on tribological behavior of the az31 alloy. *Journal of Materials Science & Technology*, *32*(12), 1245–1252.

Xin, R., Li, B., Li, L., & Liu, Q. (2011). Influence of texture on corrosion rate of az31 mg alloy in 3.5 wt.% nacl. *Materials & design*, *32*(8-9), 4548–4552.

Xu, J., Wang, X., Zhu, X., Shirooyeh, M., Wongsa-Ngam, J., Shan, D., ... Langdon, T. G. (2013). Dry sliding wear of an az31 magnesium alloy processed by equal-channel angular pressing. *Journal of Materials Science*, *48*(11), 4117–4127.

Yamashita, A., Horita, Z., & Langdon, T. G. (2001). Improving the mechanical properties of magnesium and a magnesium alloy through severe plastic deformation. *Materials Science and Engineering: A*, *300*(1-2), 142–147.

Yang, Q., Jiang, B., Tian, Y., Liu, W., & Pan, F. (2013). A tilted weak texture processed by an asymmetric extrusion for magnesium alloy sheets. *Materials Letters*, *100*, 29–31.

Yang, X., Ma, X., Moering, J., Zhou, H., Wang, W., Gong, Y., … Zhu, X. (2015). Influence of gradient structure volume fraction on the mechanical properties of pure copper. *Materials Science and Engineering: A*, *645*, 280–285.

Yang, Z., Li, J., Zhang, J., Lorimer, G., & Robson, J. (2009). Review on research and development of magnesium alloys. *Acta Metallurgica Sinica (English Letters)*, *21*(5), 313–328.

Yin, F., Han, Q., Rakita, M., Wang, M., Hua, L., & Wang, C. (2015). Numerical modelling and experimental approach for shot velocity evaluation during ultrasonic shot peening. *International Journal of Computational Materials Science and Surface Engineering*, *6*(2), 97–110.

Yin, F., Rakita, M., Hu, S., Sertse, H. M., & Han, Q. (2017). In-situ method to produce nanograined metallic powders/flakes via ultrasonic shot peening. *Journal of Manufacturing Processes*, *26*, 393–398.

Zhang, C., Zhu, S., Wang, L., Guo, R., Yue, G., & Guan, S. (2016). Microstructures and degradation mechanism in simulated body fluid of biomedical mg–zn–ca alloy processed by high pressure torsion. *Materials & Design*, *96*, 54–62.

Zhang, H., Hei, Z., Liu, G., Lu, J., & Lu, K. (2003). Formation of nanostructured surface layer on aisi 304 stainless steel by means of surface mechanical attrition treatment. *Acta materialia*, *51*(7), 1871–1881.

Zhang, H., Huang, G., Roven, H. J., Wang, L., & Pan, F. (2013). Influence of different rolling routes on the microstructure evolution and properties of az31 magnesium alloy sheets. *Materials & Design*, *50*, 667–673.

Zhang, J., Xu, J., Cheng, W., Chen, C., & Kang, J. (2012). Corrosion behavior of mg–zn–y alloy with long-period stacking ordered structures. *Journal of Materials Science & Technology*, *28*(12), 1157–1162.

Zhang, Y., Han, Z., Wang, K., & Lu, K. (2006). Friction and wear behaviors of nanocrystalline surface layer of pure copper. *Wear*, *260*(9-10), 942–948.

Zhao, M.-C., Liu, M., Song, G., & Atrens, A. (2008). Influence of the β-phase morphology on the corrosion of the mg alloy az91. *Corrosion Science*, *50*(7), 1939–1953.

Zhilyaev, A. P., Shakhova, I., Belyakov, A., Kaibyshev, R., & Langdon, T. G. (2013). Wear resistance and electroconductivity in copper processed by severe plastic deformation. *Wear*, *305*(1-2), 89–99.